ABSTRACT

Title of Document: THE ROLE OF PLASMONIC RESONANCE IN ENHANCEMENT OF INTERACTION OF LIGHT AND SILVER NANOSTRUCTURES IN FLUORESCENCE

SHY-HAUH GUO, Doctor of Philosophy, 2008

Directed By: Associate Professor Raymond J. Phaneuf, Department of Material Science and Engineering

Plasmonic resonant coupling in noble metallic nanostructures to incident radiation and the related subject of localized behavior of electromagnetic waves are currently of great interest due to their potential application to biosensing, chemical sensing, optical transmission, and nanophotonic devices.

In this thesis we present the results of experimental investigations and numerical calculations on nanometer-sized metallic structure enhanced fluorescence (nMEF). These investigations are carried out with silver nanostructures fabricated by two different methods: e-beam lithography (top down) and spray pyrolysis (bottom up). By fabrication of arrays of nanoparticles with varying shape, size, and inter-particle spacing, we determine the dependence of fluorescence enhancement on these critical

dimensions and locate the optimum configuration for fluorescence enhancement for a given molecule and excitation wavelength. For practical applications, especially for rapid sensor fabrication, we then repeat the nMEF measurement with size-selected Ag nanoparticles produced with a spray pyrolysis instrument equipped with differential mobility analyzer (DMA), basing our choice of particle size and average spacing (~coverage$^{-1/2}$) on the findings from our results on electron-beam lithographically patterned structures.

To explore the role of particle plasmons in fluorescence enhancement quantitatively we compared the plasmon resonance frequencies for rod-shaped nanoparticles vs. width-to-length aspect ratios, with the shape which produces the optimum enhancement for a particular excitation/fluorescent-emission-peak frequency/polarization combination. In further experiments we measured fluorescence from two dimensional metallic stripes, with systematically-varying widths and spacings, both with and without an underlying noble metallic film. Finally, to probe the effect of the substrate, we compared fluorescence measurements in the absence of metal nanoparticles over oxide-coated silicon substrates and oxide-coated noble-metallic films.

In analyzing these results we applied both the discrete dipole approximation (DDA)[23,39] and finite difference time domain (FDTD) [24-26] methods, calculating the electromagnetic field response of our arrays to incident light. Comparison between these calculations and experiment provides physical insight as to the mechanisms of nano-metal particle-enhanced fluorescence: our results indicate local field enhancement from silver nanoparticles is crucial in nMEF.

THE ROLE OF PLASMONIC RESONANCE IN ENHANCEMENT OF INTERACTION OF LIGHT AND SILVER NANOSTRUCTURES IN FLUORESCENCE

By

SHY-HAUH GUO

Dissertation submitted to the Faculty of the Graduate School of the
University of Maryland, College Park, in partial fulfillment
of the requirements for the degree of
Doctor of Philosophy
2008

Advisory Committee:
Associate Professor Raymond J. Phaneuf, Chairman/Advisor
Professor Martin Peckerar
Associate Professor Reza Ghodssi
Assistant Professor Thomas E. Murphy
Professor Michael Zachariah

Acknowledgements

This work was supported by the DCI postdoctoral program and the Laboratory for Physical Sciences. We thank Ben Palmer for allowing us access to the e-beam lithography system used in fabricating most of the nanostructures studied in this thesis, D.-H. Tsai and M. R. Zachariah for spray pyrolysis-synthesis of silver nanoparticles, J. Simpson and H. D. Drew for carrying out optical transmission measurements from our arrays. We also thank S.-J. Tsai, T. D. Corrigan, and H.-C. Kan, both for carrying out DDA calculations, and for valuable discussions.

Table of Contents

Chapter 1: Introduction

1.1 Motivation

Nanostructures with appealing optical [1], electronic [2], and magnetic [3] properties are generating much enthusiasm in many fields, including material science, optics, and molecular biology. One of the most active areas is the investigation of the interaction of light with nanostructured systems, including surface enhanced Raman Scattering (SERS) [4] [5] [6], enhanced fluorescence [7], or light absorption efficiency [8] with applications in chemosensors [9], biosensors [10], and photovoltaic devices [11] respectively. The enhanced interactions are generally attributed to resonant coupling between radiation and particle plasmons in noble metallic nanostructures, and the possibility of tuning this resonance to coincide with that for resonant excitation of nearby molecules. We note in passing that SERS and fluorescence are different types of light-matter interaction and thus the nature of interactions between nanostructures and molecules in these two cases is not the same; in this thesis, we only focus on the latter phenomena.

During the last few decades, fluorescence has been the technique of choice for many assays in the biological sciences. Fluorescence spectroscopy is considered to be an essential research tool in biotechnology, especially in cellular and molecular imaging. Given this, spectroscopic enhancement of fluorescence would play an enabling role in the measurement at increased sensitivity, perhaps at the level of single-molecule detection. Recently, there has been a large interest in exploiting metal enhanced fluorescence and its applications to biotechnology [20, 28~30]; in these,

the contribution of the local surface Plasmon resonance is seldom emphasized. There have also been recent reports on fabrication of ordered Ag and Au nanostructures which focused on both extinction spectra and on surface-enhanced Raman scattering, but not on enhanced fluorescence [17][31,32].

1.2 Background

Fluorescence is a process in which the absorption of a photon by a molecule results in the emission of another photon with a longer wavelength due to Franck-Condon effect [27], which applies only to changes in the vibrational levels of a molecule in the course of a change in electronic levels. Unlike the excited state in phosphorescence, in the excited singlet states for fluorescence, the electron in the excited orbital is paired by opposite spin to the second electron in the ground-state orbital. Consequently, return to the ground state is spin allowed and occurs rapidly by emission of a photon.

There are several principal effects which contribute to fluorescence enhancement: first of all, arrays of nanostructures spaced at separations smaller than the wavelength of light may lead to a localization of strong electromagnetic fields, overcoming the diffraction limit of conventional optics. A periodic corrugation at the interface between the metallic and the dielectric media may serve in production of photonic crystals [12] or gratings [13] which open up gaps in the dispersion relation for the excitation of surface plasmons. Based upon the image effect for a charge in front of the metallic film [16], localized plasmons may couple to traveling plasmons in the presence of the metallic ground plane [14] which lies beneath the nanostructures. The

resonance frequencies and local field distribution are determined by the shape, size, spacing and composition of the nanostructures, as well as the dielectric constant of the surrounding medium [1] [15] [17].

There have been a number of other studies of metal nanoparticle enhanced fluorescence. Reports by Geddes *et al.* [7,19,20] and Gerber *et al.* [21] provided evidence that the coupling between fluorophores and the plasmon electrons is important to enhanced fluorescence. These two groups reached similar conclusions: that the interactions between the excited fluorophores and nanoparticles change the fluorophores' radiative decay rate which, in turn, enhances fluorescence. As we show below and elsewhere [22] however, this model is not complete: it neglects the nanoparticles' response to incident light and the spatial distribution of fluorophores. The plasmonic contribution to the electric field distribution is not uniform near the surface of nanoparticle. As a result, fluorophores at different locations will interact with the oscillating charge which constitutes the plasmon differently, which may result in different radiative decay rate. In spite of extensive previous study having been done in this area, it was not clear at the outset of the work reported in this thesis whether the incident light induced effect or coupling between fluorophores and nanoparticles dominated the total enhancement. How the radiative decay rate of fluorophores at different location is affected by the latter is also not yet clear. While the role of substrates in enhanced fluorescence has generally been neglected in previous work, there have been reports [14] [16] suggesting a potential coupling between

localized particle plasmons and traveling surface plasmons in the presence of an underlying metallic film.

1.3 Organization

The remainder of this thesis is organized as follows: in chapter 2 we describe the experimental techniques used in fabricating and characterizing our arrays of silver nanoparticles and the fluorescent molecules. In chapter 3 we describe a series of experiments in which we measure the dependence of the fluorescence enhancement from different silver nanostructures on the size, shape and spacing of the particles, as well as the nature of the substrate, and thickness of spacer layers. We begin that chapter with results on size-selected spherical nanoparticles, comparing the fluorescence with measurements of the optical extinction [18], and calculations of the local fields, carried out by two different methods. In the second part of chapter 3 we describe the results of a systematic study of enhanced fluorescence from arrays of Ag columns of square and triangular cross section fabricated by electron beam lithography [17]. We next describe results for anisotropic, rod-shaped columns consisting of both extinction and fluorescence measurements to determine the incident light-polarization dependence of fluorescence on the rods' width-to-length aspect ratio. We discuss the limitations of a simple model based only on resonant Plasmon coupling in light of these results. We end chapter 3 with results from two dimensional nano-groove structures with and without an underlying metal film, comparing the results with those of numerical calculations, and relating the local electric field resulting from the interaction between nanostructures and incident light

to the enhanced fluorescence we observed. Chapter 4 gives some overall conclusions from this work. Additional details on the calculations and measurements are given in a series of appendices.

Chapter 2: Experimental and Numerical Methods

2.1 Metallic nanostructure fabrication

2.1.1 Electron-beam lithography

We employed conventional electron beam lithography to create the well-defined characteristic nanoparticles and other nanofeatures. The procedures are indicated schematically in figure 2.1. In most of our studies we used Si (001) substrates (1~10 $\Omega - cm$). We first deposited approximately 25nm of an aluminum oxide (Al_2O_x) onto these substrates to improve the adhesion of the silver nanoparticles, as Ag does not wet SiO_2. We next spun polymethyl methacrylate (950,000 molecular weight, 4% resins in anisole solvent) onto the substrates, and then patterned this layer using a field emission scanning electron microscope (SEM, JEOL JSM-6500F), which has been modified for electron beam lithography control (Nabitty). A silver layer, typically 75nm thick, was deposited using an electron beam evaporator (CHA Mark 40). After this, the part of the silver layer coating the resist was removed by a lift-off procedure.

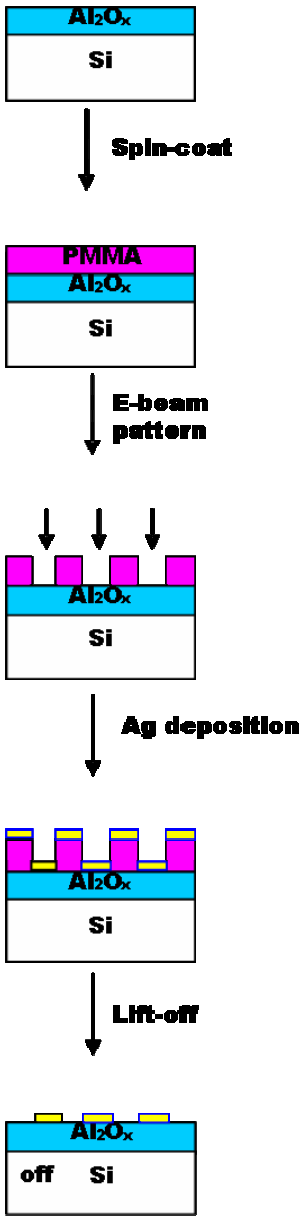

Figure 2.1: Schematic of electron beam lithography procedures for producing Ag nanostructures on aluminum oxide coated silicon substrate.

2.1.2 Spray Pyrolysis Synthesis

As a faster alternative to electron beam lithography, we synthesized spherical silver nanoparticles by spray pyrolysis as shown schematically in Fig. 2.2 [33] Aerosol particles were produced by passing a carrier gas through an oven in which Ag is heated to 1100-1200 ^{0}C resulting in evaporation and condensation. These are then charged and passed through a differential mobility analyzer (DMA) [34], [35] for size-selection. Next the aerosol passed through second furnace, in which the particles were sintered in hydrogen to make them spherical. These spherical, size-selected particles were directed onto a Si (001) substrate [33], [35] which as pre-patterned with a square grid of crossed lines using photo-lithography. The pattern allowed navigation to the same position with both scanning electron microscopy (SEM) for particle metrology and laser scanning microscopy (LSM) for fluorescent imaging.

We obtained statistics of the size and the number density of the particles by analyzing the SEM images scanned from the sample (appendix C). [36] All of the measurements reported below were done in regions away from the grid lines, i.e. on the oxide-coated Si substrate. We varied the average diameter of the nanoparticles over the range from 50 nm to 320 nm. A statistical analysis showed a maximum of 7% standard deviation from the average. The aerial coverage of the particles varied from 4% to 15% between samples; we corrected for this variation in the analysis, as described in section 2.9.

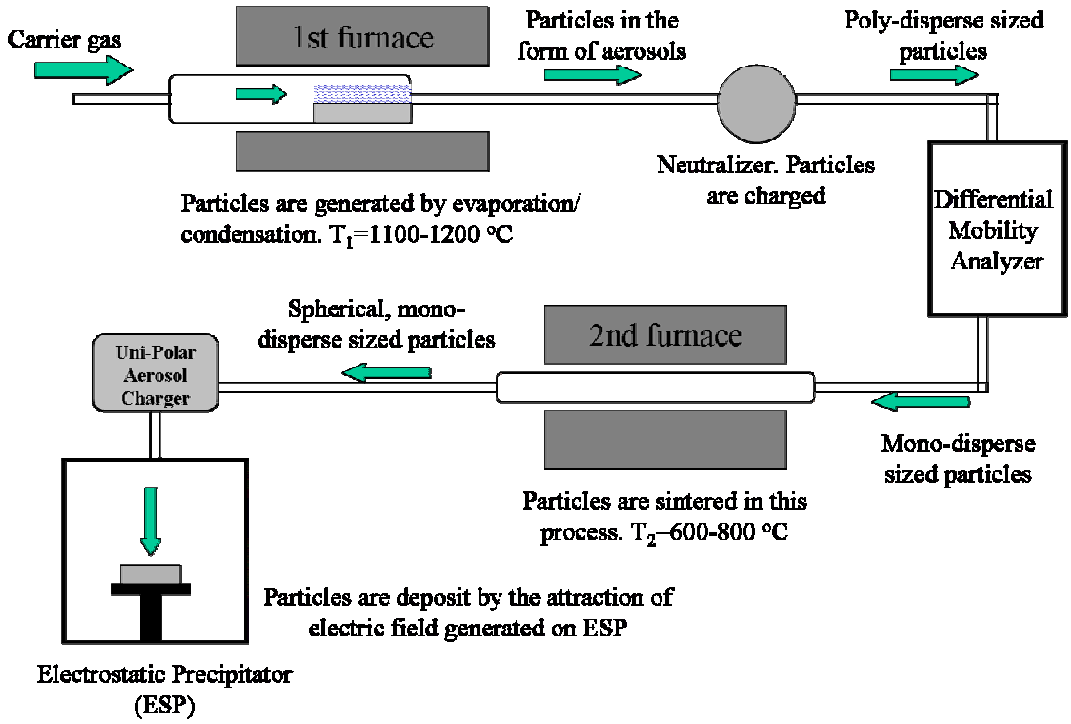

Figure 2.2: Schematic of synthesis of size selected spherical silver nanoparticles (From Ref. [33]).

2.2 *Atomic Force Microscopy (AFM) Measurement*

Imaging of surfaces under study was performed with a commercial AFM (Digital Instruments Dimension 3100), using tapping mode, in ambient atmosphere. We used AFM to characterize the sample topography after each fabrication step, determining surface roughness as well as the height of the nanostructures.

An important issue in our analysis of enhancement factor was whether the fluorescently tagged proteins covered both the Ag nanostructures and the oxide-coated substrate. We resolved this unambiguously by measuring AFM force curves from Ag nanostructures and the substrate before and after depositing the fluorescently-tagged protein. It is well known that hydroscopic forces, in particular the meniscus force dominate the van der Waals forces for measurements done in ambient atmosphere. As these depend strongly on relative humidity, force curve measurements done in ambient are difficult to reproduce. [37] We solved this problem by performing our measurements with both the sample and stylus immersed under the same buffer solution used in storing the proteins, eliminating the meniscus force, and resulting in repeatable surface tension forces. The measurement scheme is shown in Fig. 2.3. The adhesive force, measured on withdrawing the tip while under a buffer solution is large and different before protein deposition: 21nN from the Ag nanostructures vs. 10 nN from the surrounding substrate. The adhesive force between the tip and Ag nanoparticle surface and between the tip substrate surfaces is nearly identical and much smaller, ~1nN, after protein deposition; the force curves are shown in Fig. 2.4. Based on these measurements we concluded that both the Ag nanostructures and substrate were coated with protein.

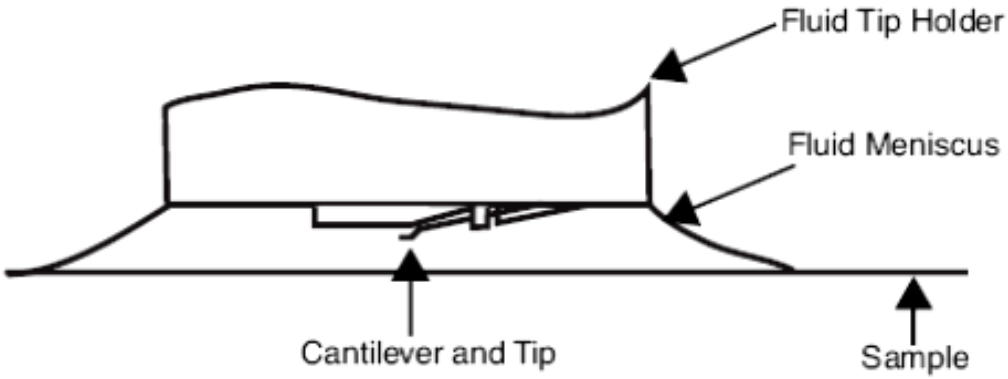

Figure 2.3: Schematic showing experimental set up for force curve measurement under fluid.

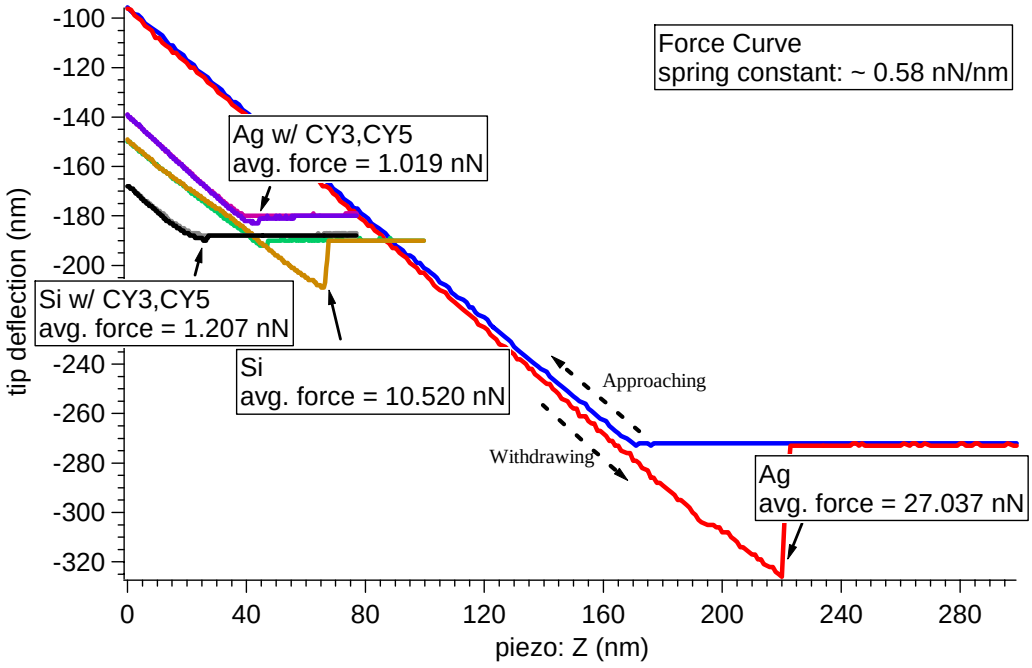

Figure 2.4: Force curves, as measured by AFM under a buffer solution, both before and after protein deposition on Ag nanostructures and Si substrate. We use a SiN cantilever with spring constant ~0.58 nN/nm, and both approaching and withdrawing curves (as labeled for example) are plotted for each situation. The adhesive force is calculated by multiplying the maximum tip-withdrawing deflection with the tip's spring constant.

2.3 *Coating sample with fluorescent molecules*

A spacer is generally required between the fluorescent molecule and metallic surfaces to prevent quenching of the fluorescence. In our experiments we used a self-assembled monolayer (SAM) spacer layer of Bovine Serum Albumin (BSA) - biotin (protein) to define a definite fluorophore to metal spacing. CY3, CY5 dyes were held in place using BSA-biotin as streptavidin conjugates. Both dyes were deposited on the same surface using an equimolar mixture in a 1 μM dilute buffer solution. The buffer consisted of a 5 mM solution of NaH_2PO_4 with the pH adjusted to 7.5. Finally we rinsed away fluorophore-tagged protein which was not bound to underlying BSA-biotin. Applying both dyes simultaneously eliminated variation in sample preparation and allowed the same areas to be evaluated using two spectral windows. The distance from the silver surface to the fluorescent tags is estimated to be approximately 8nm. Figure 2.5 is a schematic of the coated sample surface.

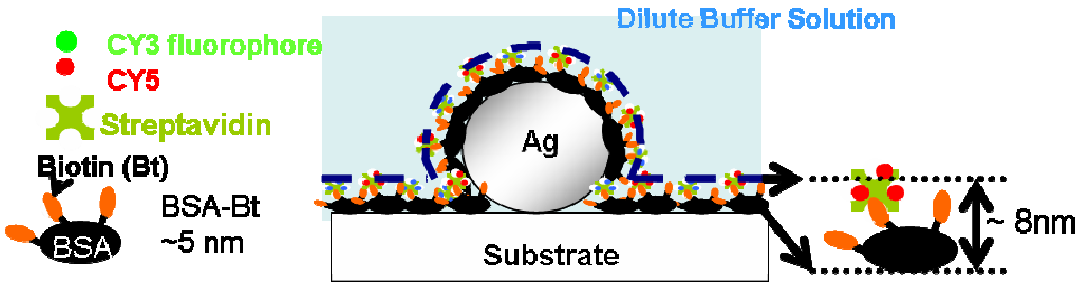

Figure 2.5: Schematic illustrating coating fluorophores onto Ag nanoparticles on substrate.

2.4 Fluorescence measurements

Fluorescence images of the sample were collected using a confocal laser scanning microscope (Zeiss model LSM 410) with objective lens producing a magnification of 100 and a numerical aperture of 0.8. The samples are maintained wet, i.e., under a thin layer of dilute buffer solution (as described in section 2.3). The absorption and emission spectra of the CY3 and CY5 fluorophores and excitation wavelengths are plotted in figure 2.6. CY3 was excited by linear polarized light using the 514 nm line of an Argon ion laser, and the fluorescence collected through a filter which passes light in the wavelength range from 535 to 575nm. For CY5 the 633 nm line of a He-Ne laser was used for excitation, and the fluorescence collected through a filter passing light of wavelength above 660nm. The measurement scheme is shown in figure 2.7. To extend the dynamic range, the LSM is equipped with a set of attenuation filters with index numbers of 1, 3, 10, 30, 100, 300, and 1000; the relative intensity passed by a filter is the reciprocal of the index number. For confirmation, we have done measurements, collecting a series of fluorescence images under different attenuation filters, and finding the average intensities from each. Since the dynamic range in an 8-bit gray level image is only 256 levels, any higher fluorescence intensity (I_f) would be truncated at the maximum value of 255. The detector dark current sets the lower limit of the range of measurable intensity; this is taken as the "background" intensity, I_B (Fig. 2.8). In the results presented in this thesis, we adopt the common convention of defining the ratio of background-corrected fluorescence intensities as $R = \frac{I_{f_2} - I_{B_2}}{I_{f_1} - I_{B_1}}$, where I_{f_2} is the average

fluorescent intensity with one level higher in attenuation index compared with I_{f_1}, and the same relationship between the average background intensities I_{B_1} and I_{B_2}. The near-linear region (around attenuation index 10 in Fig. 2.8) would manifest itself near the intensity ratio 3 in Fig. 2.9 (within the marked band). Having experimentally measured the attenuation produced by each filter, we are able to unify different dynamic ranges from various experimental results simply based on the optimum attenuation index value.

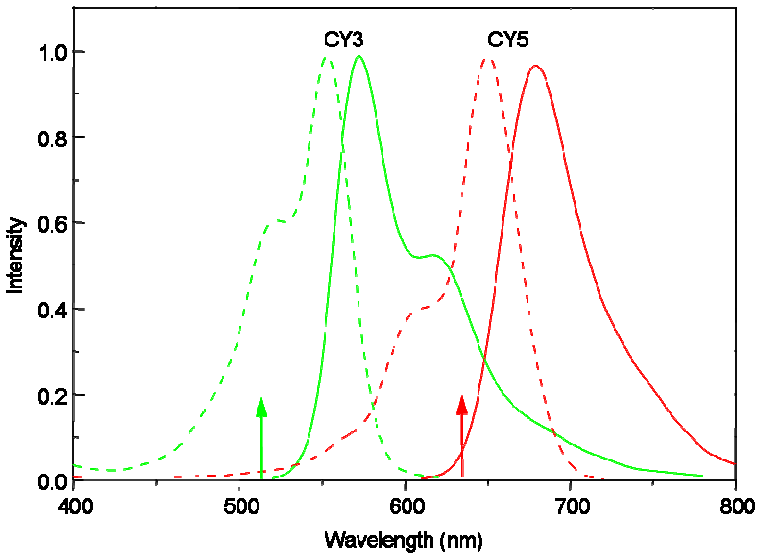

Figure 2.6: Absorption (dash) and emission (solid) spectra of CY3 (green) and CY5 (red); Laser lines used for excitation are shown with arrows: 514 nm (green) and 633 nm (red).

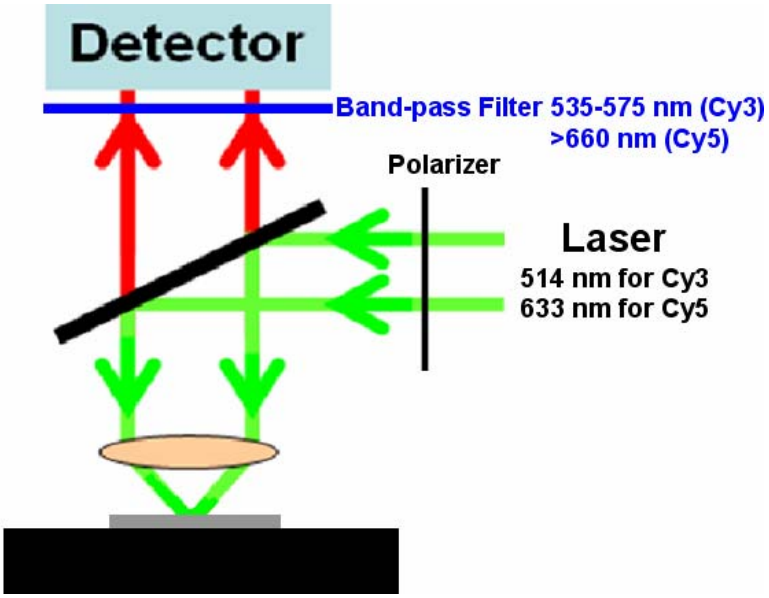

Figure 2.7: Schematic of laser scanning fluorescence microscopy measurement.

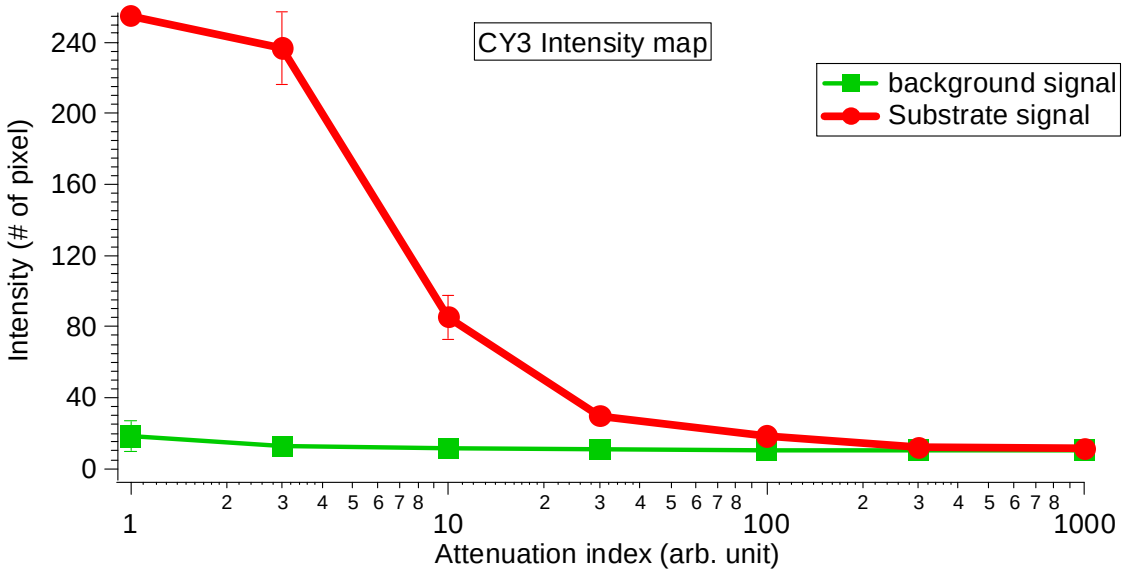

Figure 2.8: Intensity as a function of attenuation index of filter from CY3 fluorophore.

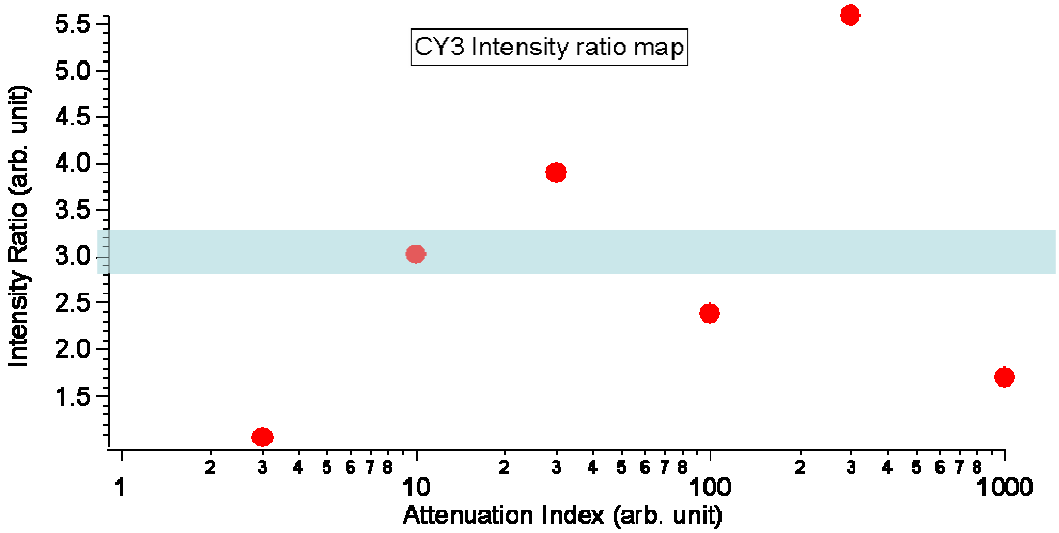

Figure 2.9: Intensity ratio as a function of attenuation index of filter from CY3 fluorophore.

2.5 *Scanning Electron Microscopy Characterization*

In addition to atomic force microscopy (AFM), described in section 2.2, we use scanning electron microscopy (SEM, LEO 1550 VP) to characterize the sample topography after each fabrication step. While AFM provides superior information as to feature height, SEM allows us to more precisely define the lateral dimensions of the structures, as the AFM tip is wedge shaped, and produces a convolution effect which depends on the height or depth of a feature.

The SEM also allows for energy-dispersive X-ray spectroscopy (EDX) providing direct information on compositional heterogeneity [38]. With this technique, we correlate the fluorescence enhancement with the coverage of silver nanostructures. Fig 2.10 (a), (d) shows scanning electron microscope images on silver pads and nanopillars on silicon substrates. The nanopillars prepared by electron beam lithography consist of particle arrays with controlled diameter 120nm and center-to-center spacing of 220nm. The EDX map acquired for silver pad (b) and nanopillars (e) is also given. Average x-ray signals were much lower in nanopillars due to lower effective surface areas. Surprisingly, the fluorescence (CY3) intensity was extremely high on nanopillars compared to continuous films under the same dynamic range defined by the attenuation in laser illumination as described in section 2.4. This prompted us to explore the origin of enhancement based on the vicinity of the fluorescent tags to silver nanostructures. One thing which should be noted is that the fluorescence map is taken under the linear regime for high intensity from silver nanopillars rather than from the ideal regime for silver pads. We could still

differentiate between silver pads and substrate at the lower dynamic range. We will address this in more detail in appendix J.

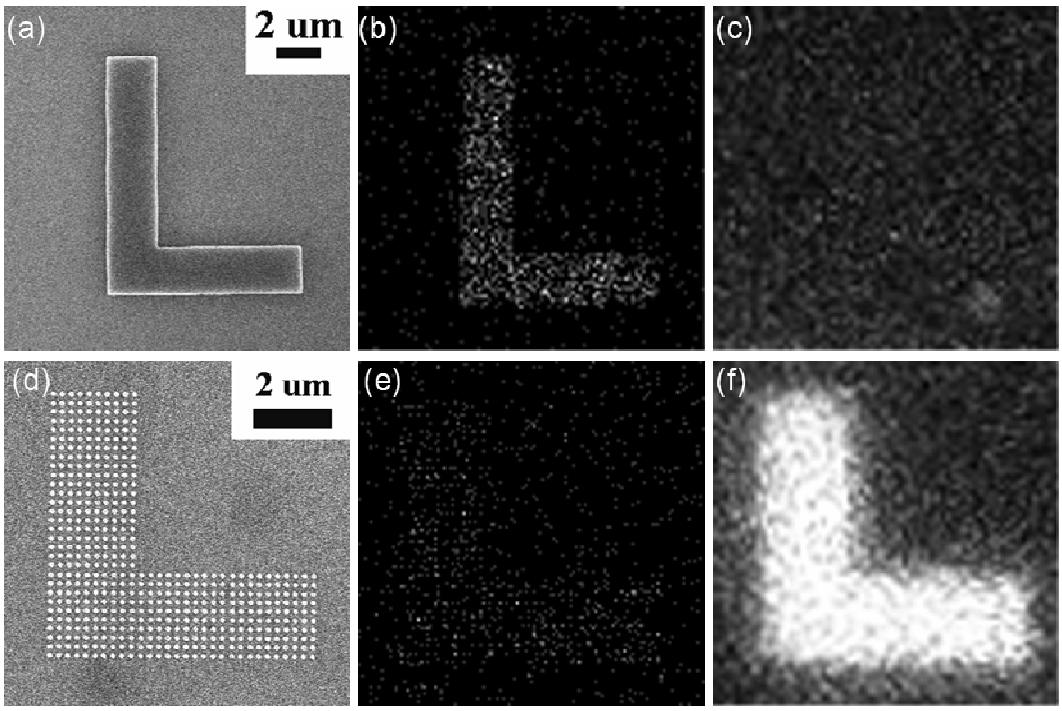

Figure 2.10: SEM images with beam energy 10keV of a silver pad (a) and nanoparticle array (d) on Si substrate consisting of diameter 120nm and center-center spacing 220nm nanopillars; EDX on silver pad (b), nanopillars (e) at energy 2.9844eV (L_{α_1} of Ag), and fluorescence (CY3) map on the same area of silver pad (c), and nanopillars (f).

2.6 Extinction measurements

To determine particle plasmon resonance frequencies for arrays of nanoparticle with varied size and shape we measured optical transmission spectra, in which the plasmon resonances appear as minima in the transmission spectrum, or as peaks in the extinction spectrum, as illustrated in Fig. 2.11.

These measurements require optically transparent substrates; we used commercial glass slides which are coated with a thin (15-30 nm), transparent indium tin oxide (ITO) layer. This conducting layer serves to prevent charge buildup during lithography, and improve adhesion of silver nanoparticles. For optical transmission measurements, metal (brass) masks provided an aperture over the silver nanoparticle array and over the bare substrate. Room-temperature transmission measurements of near-normal incident light at frequencies from 1 to 3 eV were performed using a Fourier-transform spectrometer. Comparing results with different polarizations of excitation light, we explore the role of the plasmon resonance coupling in fluorescence enhancement.

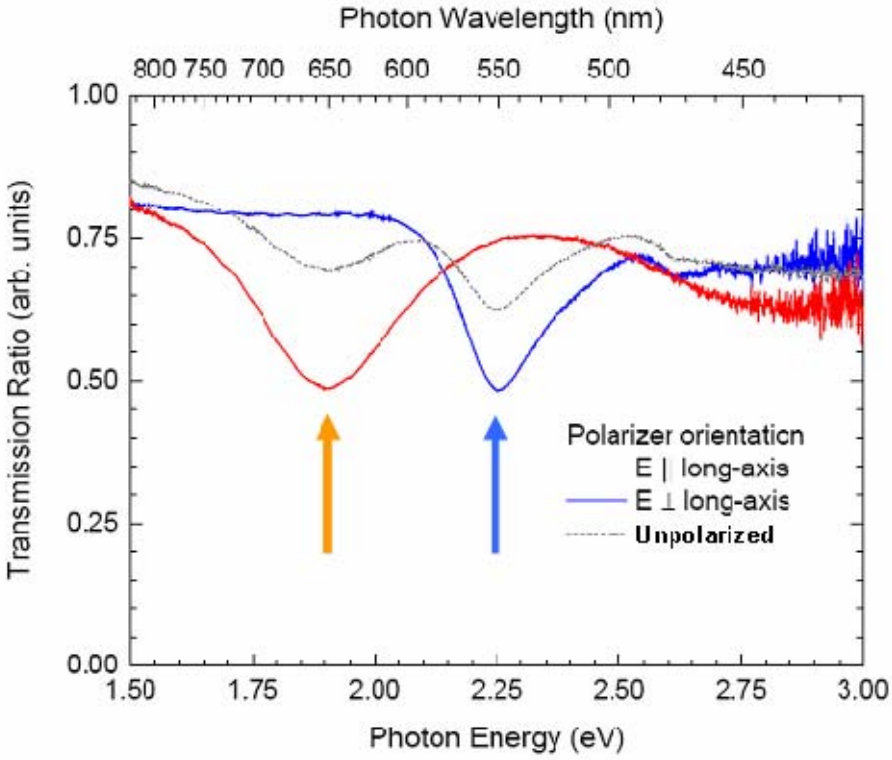

Figure 2.11: ***Transmission spectra measured for an array of rod-shaped Ag nanoparticles of lateral aspect ratio 2:1 deposited on ITO-coated glass. The red curve is for the electric field vector of the incident light parallel to the long axes of the rods; the blue curve is for the electric field vector perpendicular to the long axis of the nanoparticles.***

2.7 Numerical calculations

As part of the work presented in this thesis, we carried out numerical simulations to calculate the local electric field for arrays of noble metallic nanostructures with various shape, period, spacing, dielectric constant of surrounding media, as well as optical extinction spectra. The numerical calculations were based on two different modeling methods. The first is the finite-difference time-domain method (FDTD) [24-26], which is well suited to describing field distributions in regular arrays of nanostructures, due to the simplicity with which periodic boundary conditions can be set. As a second approach we used the discrete-dipole approximation method (DDA) [23, 39] to compute the extinction, scattering, and absorption cross sections for a single nanoparticle or particle arrays on a finite substrate. The calculations were performed for nanoparticle dimensions comparable to or smaller than the wavelength of the incident radiation. Furthermore, DDA provided us with the resultant spatial dipole distribution. In addition to the local field intensity distribution, it also allows evaluation the dipole moment of a nanostructure immersed in an electromagnetic field. Details for both methods are in Appendix A and B.

Chapter 3: Experimental results and discussions

PART I *Experiment with Self-assembly techniques:*

3.1 *Enhancement from Size-selected silver nanoparticles*

Figure 3.1 shows a comparison between scanning electron microscopy and fluorescence microscopy images from size-selected silver nanoparticles on the silicon substrate for the range of diameters we have studied [42]; in Fig. 3.1(a) – (e) the SEM images are shown in red, and fluorescence images for an excitation wavelength of 514 nm (exciting the Cy3 fluorophore), scanned from precisely the same regions are superposed in green. The SEM images show that particles are spherical, and randomly distributed. There are rare occasions where two or more particles are in contact; this occurs more frequently on samples with larger average particle diameter, as shown in Fig. 3.1(e). In general, however, individual particles are well separated from their neighbors. The images show a strong and systematic variation as the average diameter of the Ag nanoparticles is varied. Highest fluorescence intensities are obtained from samples with particle diameters slightly below the middle of range we have studied, i.e. for d ~ 90 nm. A similar trend, but with a slight increase in the optimum diameter is also observed from fluorescent images for an excitation wavelength of 633 nm, as discussed below.

The fluorescence images also show variation of the intensity from point to point within an image; this is apparently due to variation in the coverage of the tagged

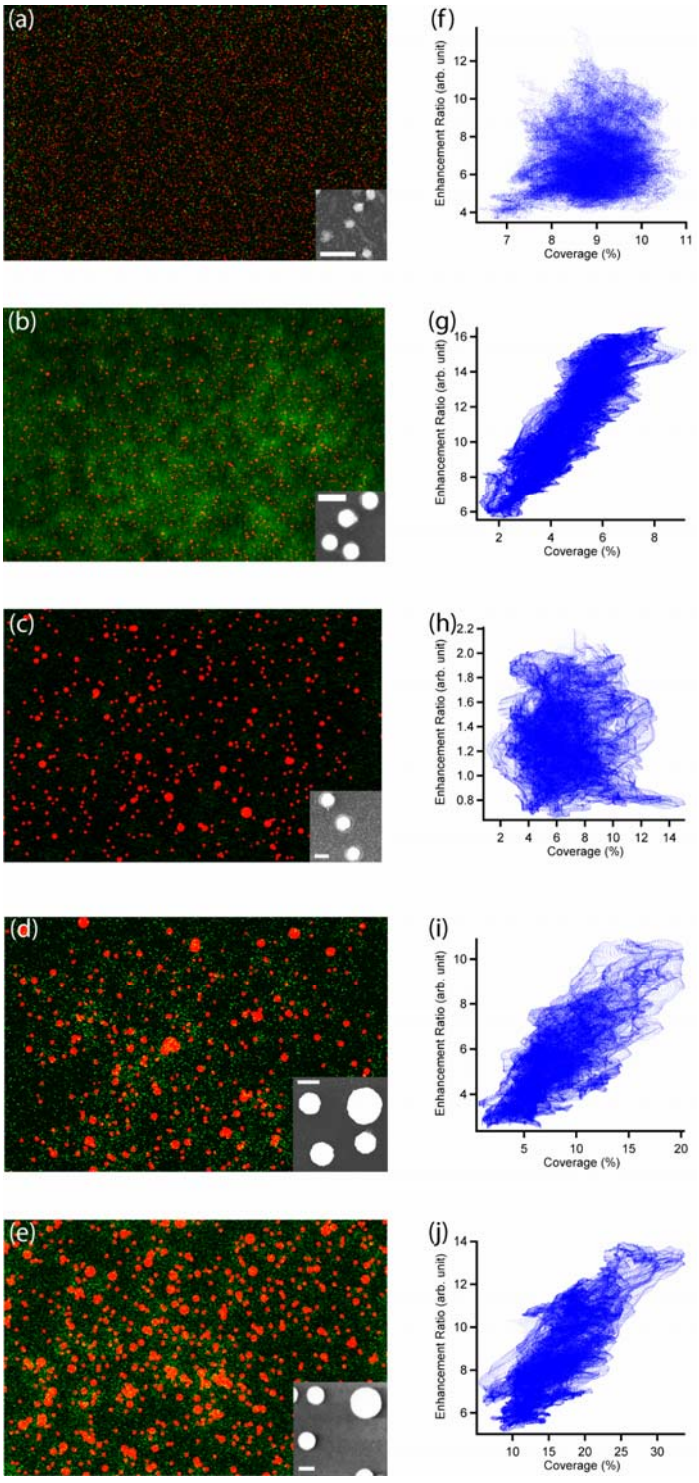

Figure 3.1: (a)-(e) SEM images (red) of the Ag nanoparticles deposited on silicon substrates, and the corresponding fluorescent images (green) for Cy3 fluorophore scanned with LSM from the same cell: The field of view is 20 μm. (f)-(j) Fluorescent intensity vs. local Ag nanoparticle coverage determined from 10 μm windows from panels (a)-(e). The average particle diameters in each panel are (a), (f) 67 ±1 nm, (b), (g) 96±2 nm, (c), (h) 173±24 nm, (d), (i) 271 ±14 nm, and (e), (j) 319 ±17 nm. The inset in panels (a)-(e) show higher magnification SEM images allowing the particle shapes to be seen; the size of the scale bar in the insets is 200 nm.

protein, as we find that this variation remains fixed when additional images of the same region are scanned and many of the bright regions occur between relatively well separated Ag nanoparticles. There are no extremely intense "hot spots" between particles in near – contact [44] or in agglomeration; however there is a correlation between local coverage for certain particle sizes, as seen in Fig. 3.1(g) and (i) where the local fluorescence intensity varies linearly with local Ag nanoparticle coverage within a sample. For other particle sizes the intensity and coverage are nearly independent. Interestingly, it is for those particle sizes corresponding to highest fluorescent intensities that a strong correlation exists.

In analyzing the effect of the nanoparticles on the fluorescence we define the normalized fluorescence enhancement ratio to be $N = \frac{I_a - I_B}{I_f - I_B}$, with $I_a = \frac{I_e - (1 - A_a) \cdot I_f}{A_a}$, where I_a is the average fluorescent intensity normalized with the percentage aerial coverage A_a of the silver nanoparticles (measured using SEM). I_e is the raw fluorescent intensity measured from areas containing fluorophore/spacer coated silver nanoparticles. I_f is the fluorescent intensity without silver nanoparticles, i.e. measured from areas where only fluorophore/spacer layer is present. I_B is the background intensity measured from an area of the substrate where both fluorophore and silver nanoparticles are absent. The ratio N describes the fluorescence enhancement due to the silver nanoparticles, factoring out the effect of variations in fluorophore coverage and Ag area fraction. The finite intensity and dwell time at each point in the image leads to some statistical variation from point to point, as

evidenced by the scintillations in the fluorescence images, we thus average each of the individual intensities over a region a few microns in lateral extent.

Fig. 3.2 shows the measured nanoparticle diameter dependence. As shown in panel 3.2(a), the enhancement initially increases with particle diameter, reaching a maximum of approximately 240 at d ~ 85 nm for the 514 nm wavelength excitation; we observe a window of particle diameters between ~85 nm and ~150 nm for which the enhancement exceeds 100 fold. For excitation at a wavelength of 633 nm, the maximum enhancement of approximately 350 is measured at a slightly larger diameter, ~150 nm, as seen in panel 3.2(b); the enhancement exceeds 100 for diameters from ~95 nm to ~160 nm. Much lower or no enhancement is obtained for particle sizes outside these “high-enhancement windows”.

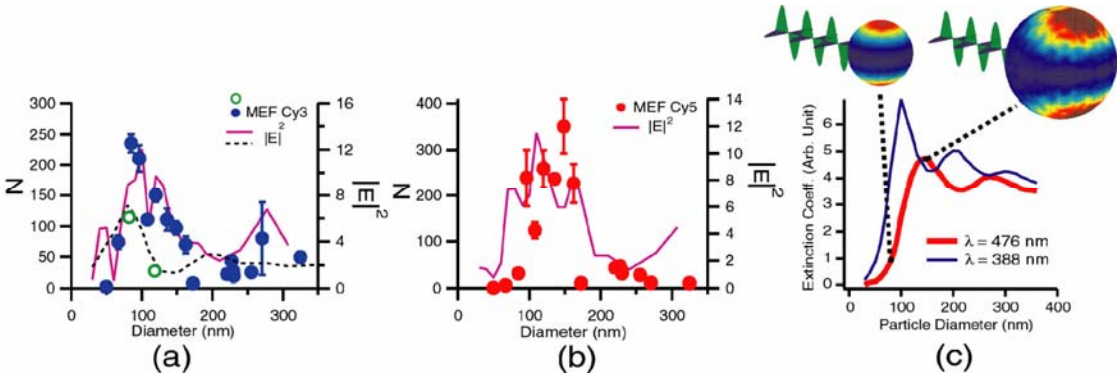

***Figure 3.2:** Measured normalized enhancement of the fluorescence, N, on silicon substrate (filled circles) or glass substrate (open circles), and the calculated (DDA) average E-field intensity (solid curve) near the Ag particles as a function of Ag particle diameter: (a) 514 nm excitation (Cy3 fluorophore), (b) 633 nm excitation (Cy5 fluorophore). The dashed curve in (a) shows the same averaged E-field intensity calculated by DDA for the case of glass substrate. (c) Calculated extinction coefficient and electrical field intensity, E^2, (with |E| normalized to incident amplitude) for silver nanoparticles by DDA. Extinction coefficients are plotted as a function of particle diameter for incident light wave length fixed at 476 nm (633 nm in air) in red curve and 388 nm (514nm in air) in blue curve. Insets show the E^2 distribution over a spherical surface 8nm from the surface of silver particles with diameter of 80nm and 150 nm, respectively. The incident light represented by the sinusoidal modulations is traveling toward the particle, and the E-field is polarized in the vertical direction (colored in green). The color scale bar indicates the field intensity normalized to that of the incident light.*

To understand the origins of the fluorescence enhancement dependence on particle size, we calculate the response of silver nanoparticles to incident light, using the discrete dipole approximation [45, 46]. In our experiment, the silver nanoparticles are always immersed in a thin layer of dilute buffer solution. Thus we assign the index of refraction of the space outside of the silver particle to that of water [47] for all calculations. For simplicity, in our calculations we model the incident light as a linearly polarized plane wave. Our SEM images show that the average particle separation well exceeds the individual diameters; therefore we limit our numerical calculations to the case of single silver nanoparticle. We begin with the simplest geometry, i.e. freely standing spherical silver nanoparticles. Fig. 3.2(c) shows the calculated extinction coefficients, normalized to the geometric cross section of the particle as a function of particle diameter. The thin blue curve is for an excitation wavelength of 388 nm in water, corresponding to 514 nm in air. The thick curve is for excitation at 476 nm in water, or 633 nm in air. These two curves display qualitatively similar trends: the extinction coefficient first increases with particle diameter reaching a maximum, (at ~100 nm for the former case and ~140nm for the latter case) then oscillates around a slow decaying tail. This behavior is qualitatively inconsistent with the abrupt drop in enhancement beyond the high-enhancement windows shown in Fig. 3.2(a), (b). Adding the substrate to the calculation might be expected to change the trend quantitatively, but not qualitatively [48]. This difference in behavior contradicts a simple correlation of fluorescence enhancement with resonant coupling between the incident light and plasmons in the silver nanoparticles. A hint as to the origin of this discrepancy comes from the calculated distribution of

electrical field intensity [39] near the particle shown in the insets. We note that the fluorescence intensity is expected to be proportional to the local intensity $\left|\vec{E}\right|^2$. The leftmost inset shows the spatial variation of the calculated E-field intensity, normalized to that of the incident light in the vicinity of an 80nm diameter silver particle, for a wavelength of 476 nm. While the optical extinction from silver nanoparticles in this size range is small, there is nonetheless a strong E-field enhancement in regions near the top and the bottom poles of the particle. The rightmost inset shows that as the particle diameter increases to 150 nm, close to where the maximum optical extinction occurs, the regions of high E-field shift away from poles of the particle. Significantly, the main effect of the particle size is in the spatial distribution, rather than the maximum value of the field strength.

We now consider how the silicon substrate affects this picture. Simple models of the enhancement based entirely upon the plasmon resonance suggest it should simply red-shift the resonance. We include it in our calculation, treating it as a finite square slab of silicon [49, 55] placed behind the particle in the direction of the wave vector $\vec{k}$ of the incident light. The lateral dimension of the silicon slab is chosen as 3 times the diameter of the silver particle; larger sizes are precluded by computer memory and practical computing time. We vary the thickness of the silicon slab from 75 nm to 450 nm, but find that this does not change the qualitative trend of the result. Figure 3 shows how the calculated E-field distribution in the azimuth of incident E-field polarization changes with the size of the silver nanoparticles; here a 150 nm thick silicon substrate and an incident light wavelength of 388 nm in water (514 nm in air) are used. Fig. 3.3(a) and (e) are 3D and cross-sectional renderings, respectively,

of the calculated intensity $\left|\vec{E}\right|^2$ for a relatively small diameter of 60 nm. As can be seen most clearly in the cross-sectional view, the silicon substrate, because of its large dielectric function, has a profound effect on the field; for this size the strongest field enhancement occurs beneath the particle. As shown in Fig. 3.3(b) and (f), increasing the particle size to 100 nm, close to the observed optimum in Fig. 3.2(a), causes regions of strong E-field enhancement to sweep upward, to the regions at and above the equator of the particle. A further slight increase in particle diameter to 120 nm results both in a slight downward sweep of the high field regions (Fig. 3.3(c), (g)), and a decrease in the measured enhancement (Fig. 3.2(a)). Increasing the particle size further, to 210 nm, both sweeps the regions of high E-field back into the region beneath the particle as shown in Fig. 3.3(d), (h), and causes a dramatic drop in the measured intensity (Fig. 3.2(a)).

This sweeping of regions of high field, and its correlation to the observed fluorescence enhancement demonstrate the profound effect of coupling to the silicon substrate. Both the particles and substrate are opaque at these wavelengths; only the fluorescent emission from molecules located in regions which are not shadowed by the particles can be observed. Remarkably, ***this active substrate has a strong effect on the size-dependence of fluorescence enhancement in the presence of a substrate.*** As a rough means of accounting for the shadowing effect in our calculation, we average the E-field intensity, i.e. $\left|\vec{E}\right|^2$, over only that region of the particle for which no shadowing occurs. Based upon the known thickness of the protein and spacer layer, the fluorescent tags are between 4-12 nm from the surface of the silver

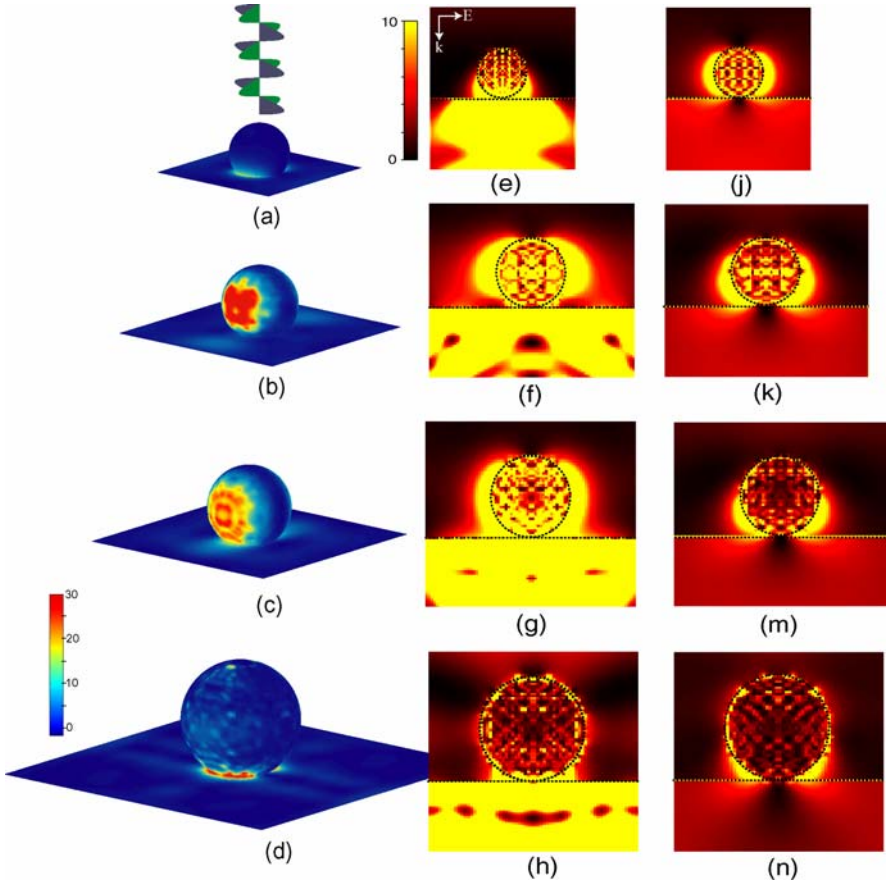

Figure 3.3: Calculated electric field intensity (E^2) distributions at the distance 8 nm from the surface of the silver nanoparticle and the silicon substrate. The particle diameters are 60nm, 100nm, 120nm, and 210nm for panels (a), (b), (c), and (d), respectively. As shown in panel (a), the incident light propagates downward and the polarization of the E-field is parallel to the substrate (colored in green). The wavelength of the incident light is 388 nm wavelength (514 nm in air). The color table indicates the field intensity normalized to the incident light intensity. Panels (e), (f), (g) and (h) are cross sectional renderings of electric field intensity (E^2) for particle diameters of 60nm, 100nm, 120nm, and 210nm, respectively; panels (j), (k), (m) and (n) are cross sectional renderings of the electric field intensity (E^2) for the same particle diameters, but on a SiO_2 substrate.

nanoparticles. We thus calculate the E-field intensity averaged over a hemi-spherical surface 8 nm from the particle surface opposite the substrate. We note that although regions of high field also exist within the substrate, no fluorescent molecules exist there. Summary plots of the size dependence of this averaged E-field intensity for the two excitations are shown as solid curves in Fig. 3.2(a), (b). Good agreement between the measured fluorescence enhancement and the calculation is evident in both cases. This result shows that the distribution of the enhanced E-field intensity is crucial to the measured fluorescence enhancement, and leads to an important insight: ***as the particle size varies, regions of electrical field enhancement shift position; maximum fluorescence enhancement occurs when a large fraction of those fluorophores which are not shadowed by either the particles or substrate are immersed in regions of high field; low or no enhancement otherwise.***

Our results thus demonstrate that coupling to an active substrate plays a striking, and unexpected role in the optimum enhancement of fluorescence by metal nanoparticles. Fluorescence from molecules located in close proximity to silver nanoparticles on a silicon substrate depends strongly on the particle diameter, with optimum normalized enhancement of at least 350 fold; the silicon substrate controls the regions of strong electric field, and in particular for which particle diameters are these regions not shadowed by the particles themselves. This effect is even more striking when compared to the field intensity which results from a more conventional, passive substrate, SiO_2. Fig. 3.3(j) - 3.3(n) show the calculated $\left|\vec{E}\right|^2$ distribution for the same particle sizes as for the Si substrate. The substrate perturbs the field much less strongly, resulting in a conventional dipole-like distribution for smaller particles,

and mixed dipolar/quadrupolar distribution at larger diameters. The resulting $\left|\vec{E}\right|^2$ vs. size dependence is shown as the dashed curve in Fig. 3.2(a). The maximum is shifted to a smaller diameter, and reduced by approximately a factor of 2; measurements, of the fluorescence enhancement for a SiO_2 substrate, shown by the open circles in Fig. 3.2(a) indeed show approximately half of the enhancement measured using a Si substrate. The effect we see is similar to the hot-spot effect between particles which is believed responsible for the observation of single molecule spectrum in SERS. [4] Here, however it is the "hot regions" around single particles, where high electrical field and thus large enhancement occurs. We thus find that it is essential to include the spatial distribution of the field near the nanoparticles into the consideration for optimizing design of biosensors employing plasmonic response from metallic nanoparticles.

3.2 Size-selected silver nanoparticles on a silver film

Since the active substrate has a strong effect on the size-dependence of fluorescence enhancement in the presence of a substrate, it would be interesting to explore how it will react with the substrate of even larger dielectric response; in this section we address this carrying out measurements of fluorescence on for fluorophores located above silver nanoparticles on an underlying silver film [16]. These measurements were in fact carried out on the same samples described in the last section; the size-selected silver nanoparticles prepared described above were also deposited on the 50 nm thick silver lines we pre-deposited to use as a navigational aid. Comparing fluorescence intensity from on and off these films, we find an additional factor of between 3-4 times in the raw enhancement ratio (i.e. with no correction for the Ag coverage), at a slightly smaller optimum average particle size for excitation of both the CY3 and CY5 fluors, as shown in Fig. 3.4. A possible explanation for this additional enhancement is an image effect for the localized plasmon in the nanoparticles in front of the ground plane. The dipole moment on the nanoparticles will induce surface charge distribution on the ground plane, and it will effectively see an image dipole within the silver film. This dipole-dipole interaction generates strong field nearby the surface, and may excite the fluorophores much more effectively than the same structure without the ground plane. An alternative explanation might be a coupling between localized particle plasmons and a surface plasmon in the film. In a later section we present a series of controlled experiments to further explore the role of the coupling between silver nanostructures and an underlying silver film in the fluorescence enhancement.

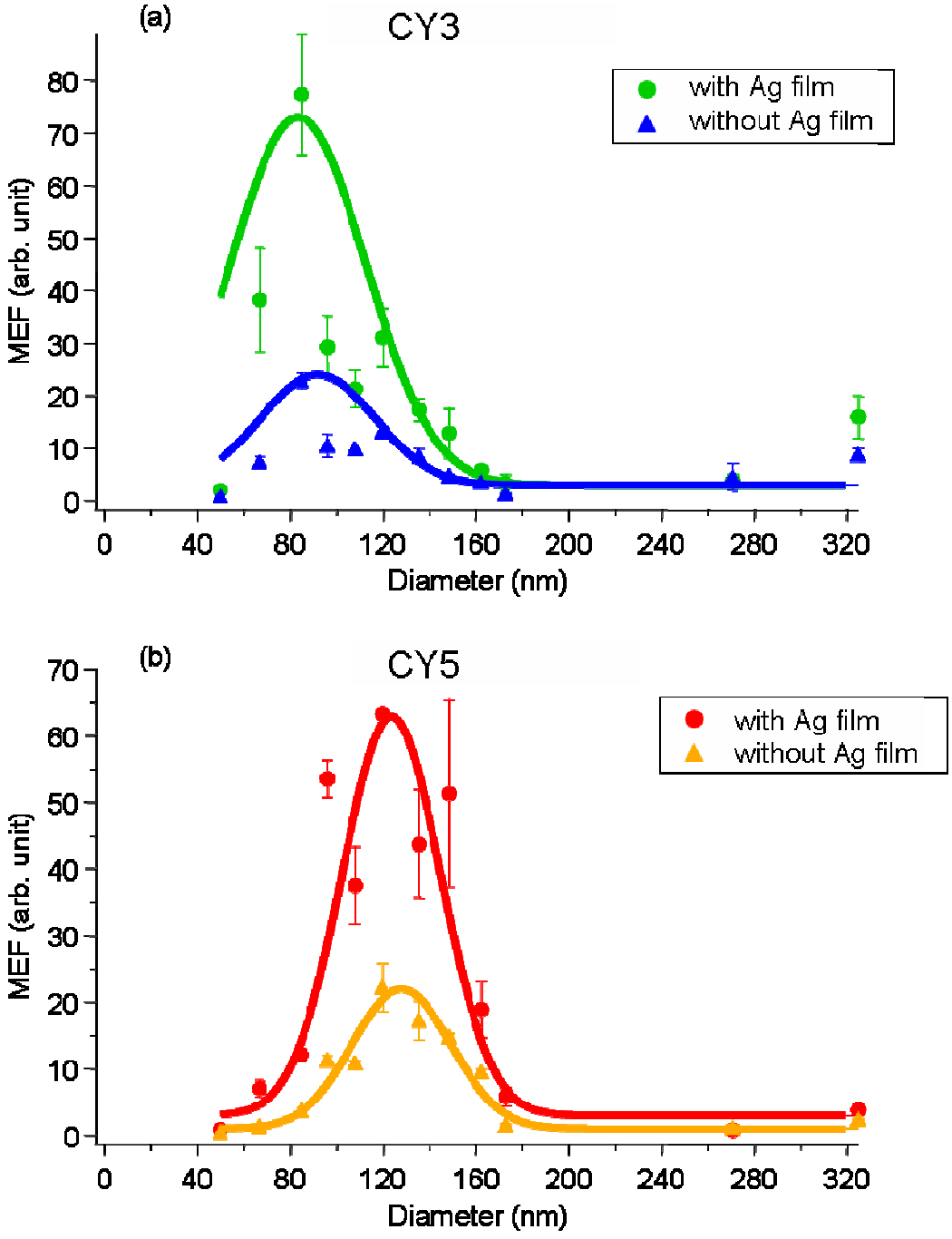

***Figure 3.4:** Summary plots for raw fluorescence enhancement for (a) CY3, (b) CY5 tagged proteins on size-selected silver nanoparticles on a silver film; also shown are the raw enhancements measured at regions with no underlying Ag film.*

PART II Fluorescence Enhancement From Nanostructures Defined by Electron-beam Lithography:

3.3 Silver Nanocolumns with Regular-Polygonal Cross Sections

We have fabricated arrays of square silver nanoparticles (as shown in figure 3.5, 3.6) with various sizes and center-to-center spacings on an aluminum oxide covered silicon substrate to investigate the optimum geometrical parameters for enhanced fluorescence [17] [50]. Examples of our scanned fluorescence images are shown in the top two panels in figure 3.7. These were measured by excitation with an Argon laser and a He-Ne laser which produce light whose wavelength is close to the maximum in the absorption spectrum for CY3 and CY5 respectively.

Our size/spacing combinatorial method has the advantage that one can visually pick out the optimum from the intensity map. Detailed plots of fluorescence enhancement versus the lateral size of the nanoparticles are shown in figure 3.7(c), (d). Fluorescence enhancement becomes highly dependent on particle size in the limit where the particle dimensions exceed roughly one-tenth the light wavelength. There is also some dependence of the optimum size on the spacing, at least for spacing/size ratios less or equal to 2. The optimum size for excitation at 514nm is approximately 90nm in the large spacing limit. This is smaller than that for excitation at 633nm where the optimum size is 110nm. These experimental observations are consistent with the red shift in the Plasmon resonance with increased lateral size of metallic nanoparticles [15, 32].

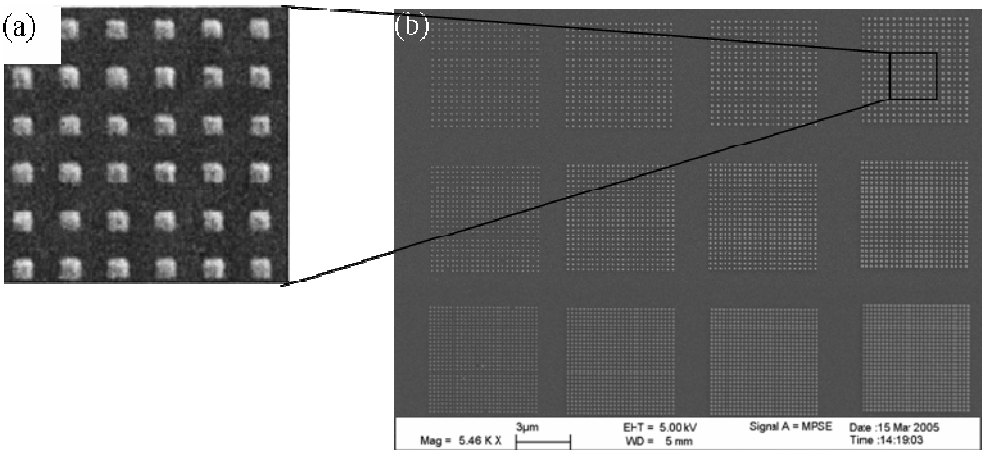

Figure 3.5: Scanning electron microscope images of Ag nanopillar arrays. (a) Detail of cell containing 130nm wide square cross-section silver nanopillars with 390 nm pitch; the field of view is 2.4µm. (b) Image showing multiple cells in which particle widths and center-center spacings are varied from cell to cell.

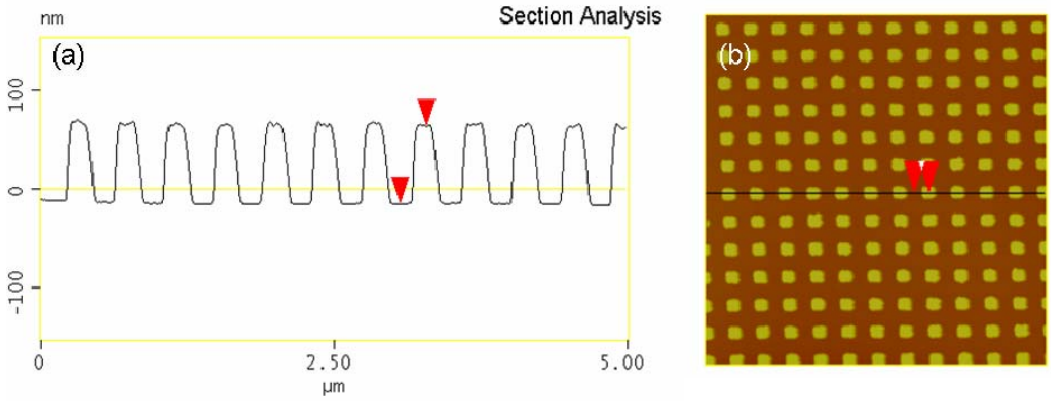

Figure 3.6: AFM image (right) and height profile (left) showing the actual height of the pillars to be ~75 nm. Field of view is 5 µm

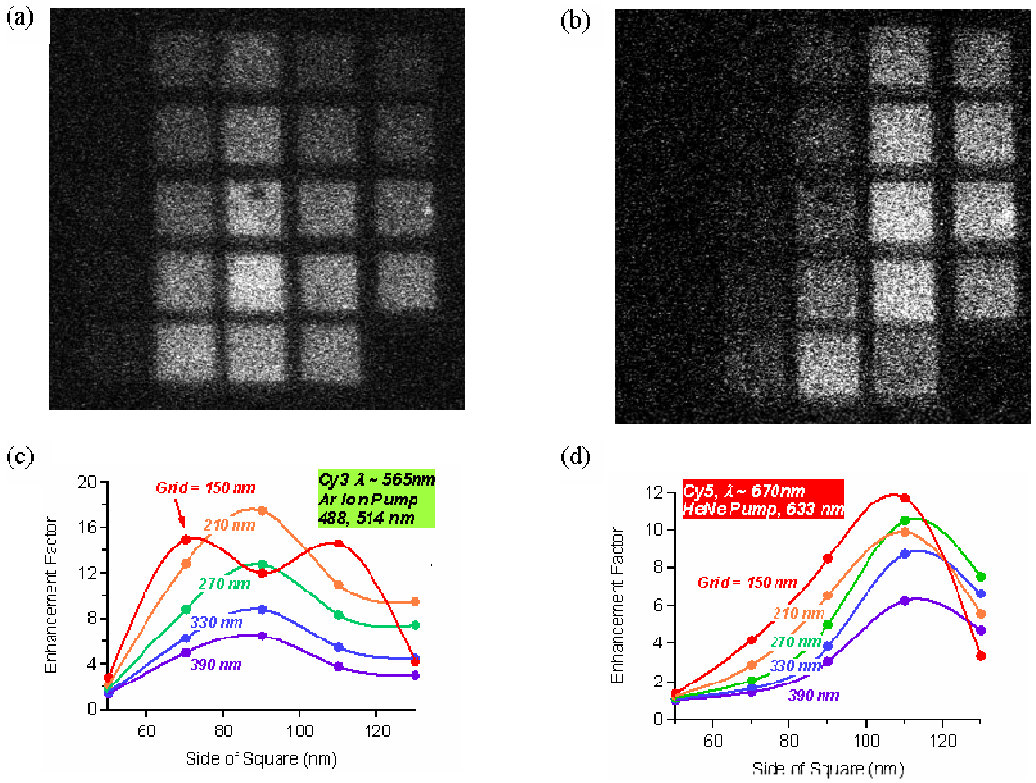

Figure 3.7: Scanned fluorescence images from a combinatorial array of square shaped nanoparticles, and excitation at (a) 514nm and (b) 633nm. (c), (d) Plots of fluorescence enhancement ratio vs. width of nanoparticles for varying spacing in nanometers and excitation at (c) 514nm and (d) 633nm.

From figure 3.7(c) and 3.7(d) it can also be seen that there is a nearly monotonic increase in the overall enhancement as the spacing decreases. Qualitatively, this is intuitive when one considers that a smaller spacing means that there is a larger area fraction of the surface covered with silver nanoparticles. Figure 3.8 presents data normalized to the area fraction of silver. The plot shows that the fluorescence enhancement is very similar for inter-particle spacings from 270-390nm. At these large inter-particle spacings each nanoparticle evidently interacts with excitation light and excited molecules individually. Beyond two times the size of the particles, our results indicate weak or no coupling between particles. In this limit, one may determine the optimal conditions for fluorescence enhancement by tuning the size of the nanoparticle (particle plasmon spectrum) to match the spectral properties of the fluorophore.

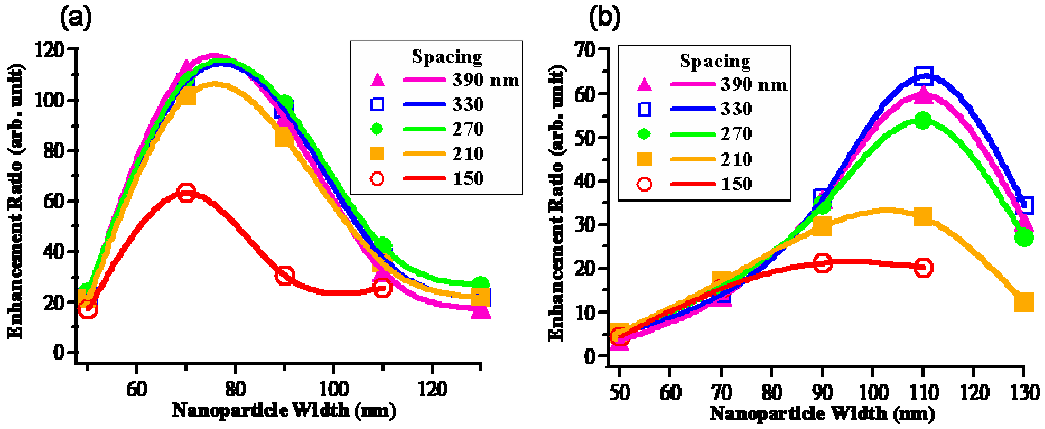

Figure 3.8: Fluorescence enhancement ratio for intensities normalized to the area fraction of silver for square-shaped nanoparticles with (a) excitation at 514 nm and (b) excitation at 633 nm.

A quantitative comparison of the observed optimal shapes with those producing a plasmon-polariton resonance coinciding with the excitation and/or fluorescence frequency is complicated by the difficulty of modeling resonances for the particle shapes studied here, including interaction with the substrate. It is known that multiple modes will be excited [51, 52], that retardation effects will be important, [53] as will interaction with the substrate [54]. Such a discussion will be carried out later in this thesis.

To explore the shape effect on enhancement, we also vary the shape of the particles as shown in figure 3.9. Panel (b) is a SEM image of a cell containing triangle silver nanoparticles whose sides are 130nm long and center-to-center spacings are 390nm. Although we do not observe large enhancements due to hot spots between particles for edge-to-edge spacings down to approximately 20 nm, we do in fact see larger enhancements for particle shapes producing greater local electric fields. Figure 3.10 shows the effect of a change in the particle shape on the fluorescence enhancement; in this case the enhancement ratio is shown for particles of triangular shape. The largest enhancement for excitation at 488/514 nm and for triangular particles is similar to square particles, but after normalizing to the actual area of silver the relative enhancement is greater for the triangles than for the squares, as seen in Fig. 10(a). The results are similar for excitation at 633 nm. When compared to results for the square-shaped nanopaticles, the lateral size of the particle that gives rise to the optimal area-normalized enhancement increases from ~75 to ~90 nm, consistent with reports by Jensen *et al.* [18] of a red-shift in the optical extinction wavelength of triangular shaped particles compared to elliptical particles. It is also

consistent with theoretical modeling by Kottman *et al*. [52] who find the Plasmon-polariton resonance for triangular shaped nanoparticles is red-shifted from other shapes, including squares. These latter calculations also predict that the peak values of the enhancement of the electromagnetic fields associated with triangles is larger than for squares and other shapes studied [52] and that the field is strongest at specific positions around and close to the nanoparticle. These should act as hot spots, resulting in a local fluorescence enhancement, in agreement with the modest increase we observe for triangular particles.

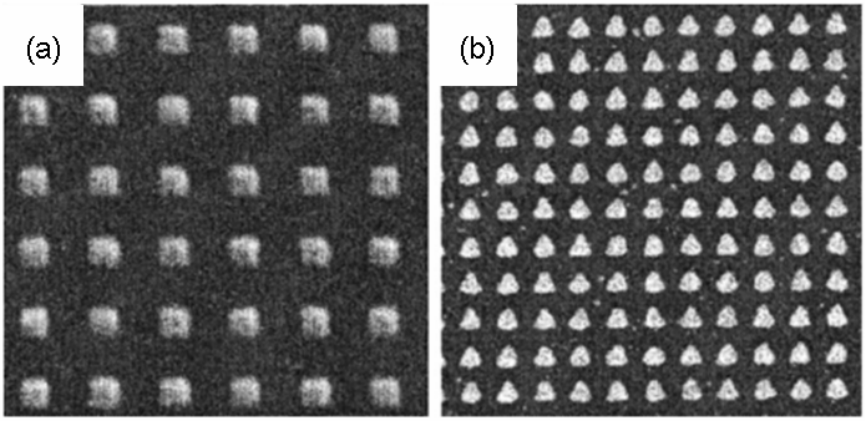

Figure 3.9: SEM images of (a) 130 nm lateral size square shaped silver nanoparticles in a field of view of 2.4 μm and (b) 130 nm lateral size triangular particles at a field of view of 4.3μm.

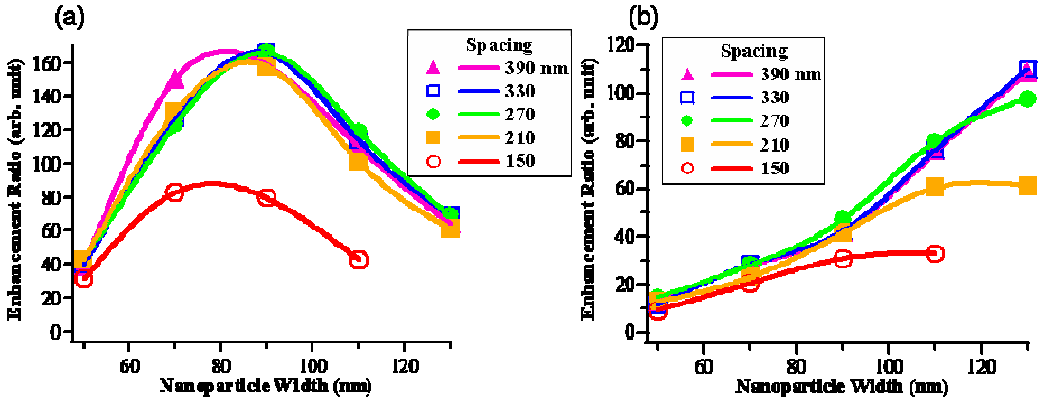

Figure 3.10: Fluorescence enhancement ratio for intensities normalized to the area fraction of silver for triangular-shaped nanoparticles with (a) excitation at 488/514 nm and (b) excitation at 633 nm.

3.4 Enhancement from anisotropic silver nanoparticles

To explore the role of particle shape in enhanced fluorescence [15] we fabricated arrays of silver pillars with rod-shaped cross sections, on an ITO-coated glass substrate; we held the edge to edge spacing fixed at 150 nm. SEM images of these structures are shown in Fig. 3.11. We again measured fluorescence for two fluorophores, Cy3 and Cy5, deposited on the sample as described above. Figure 3.12 shows fluorescence images and summary plots of the enhancement for two fluorophores and for polarization of incident light both parallel and perpendicular to the long axes. The results show a strong polarization and shape dependence of the enhanced fluorescence. For light polarization parallel to the long axis as shown in Figure 3.12(a) and 3.12(b), the optimum enhancement shifts slightly to larger particle size for longer wavelength, which qualitatively agrees with the predicted red shift of the plasmon resonance for larger particle length/width ratio [1]. For the polarization perpendicular to the long axis, however as shown in Figure 3.12(c) and 3.12(d), the peak still shifts to larger particle size for longer wavelength, which is opposite to the predicted blue shift in the transverse plasmon resonance [1]. To test this prediction, we carried out the extinction measurements in collaboration with J. Simpson and H. D. Drew. Figure 3.13 shows the wavelengths of the measured extinction peak versus aspect ratios for incident light parallel (orange) and perpendicular (blue) to the long axis. The extinction peaks (open circle) indeed shift toward red and blue with increasing aspect ratio for polarization of incident light parallel and perpendicular to the long axes, respectively; thus the extinction measurements are consistent with the theory of plasmon resonance [1]. Comparison with maxima in the fluorescence,

however, shows that only half of the four reside within the bands formed by the peaks in absorption and reemission (Cy3 in short axis and Cy5 in long axis). The detailed dependence of the fluorescence enhancement we observe on anisotropic silver nanoparticles can thus not be fully explained by the simplest model of resonant plasmon coupling. As described in the next section, to simplify the comparison, we fabricated two-dimensional structures on which it is feasible to carry out calculations of the local electric field using the finite difference time domain method.

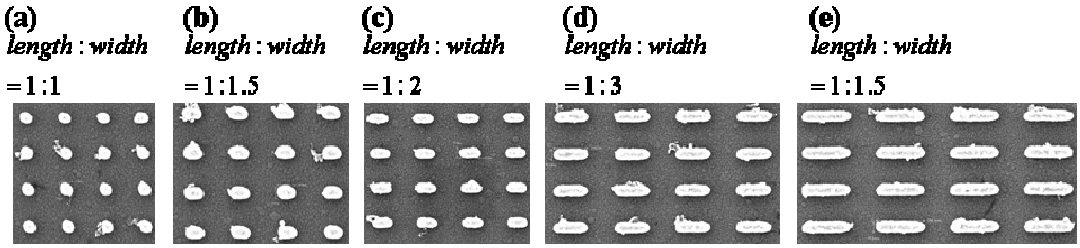

Figure 3.11: SEM images of nanorod silver nanoparticle arrays on an ITO-coated glass substrate fabricated by e-beam lithography. The height of particles are ~ 75 nm and lateral size is 75 nm x 75 nm for aspect ratio (length/width ratio) 1 particle. (a) to (e) are aspect ratios 1 to 4. The edge to edge spacing is 150 nm for all cases.

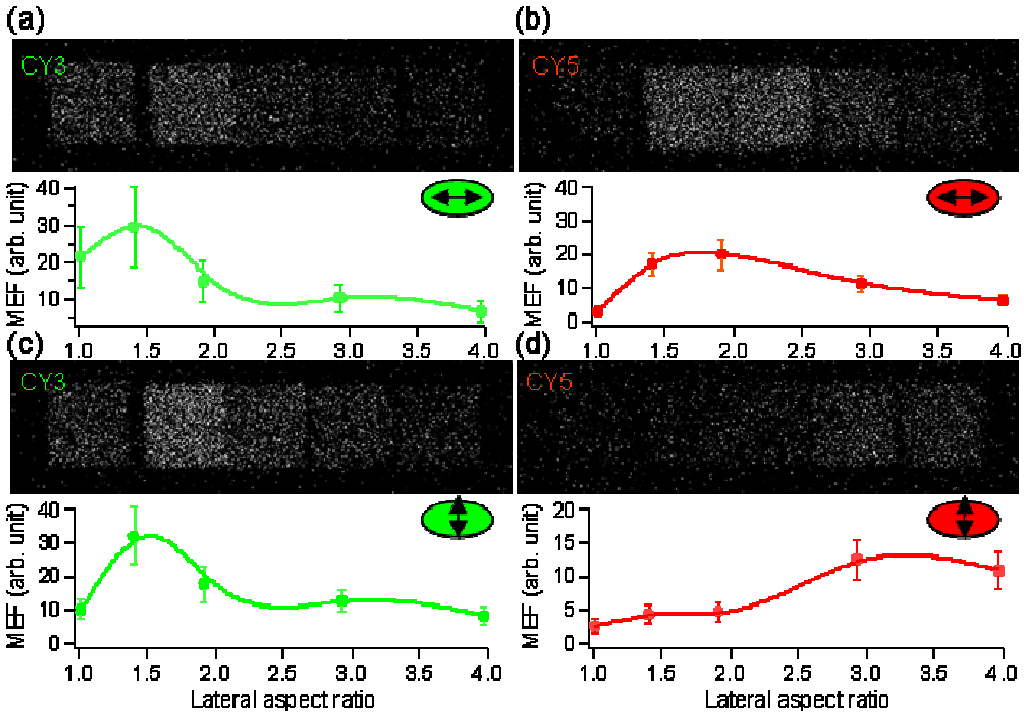

Figure 3.12: Plots of enhanced fluorescence for Cy3 (green) and Cy5 (red) and two polarizations of laser: (a) and (b) parallel to long axis; (c) and (d) perpendicular to short axis.

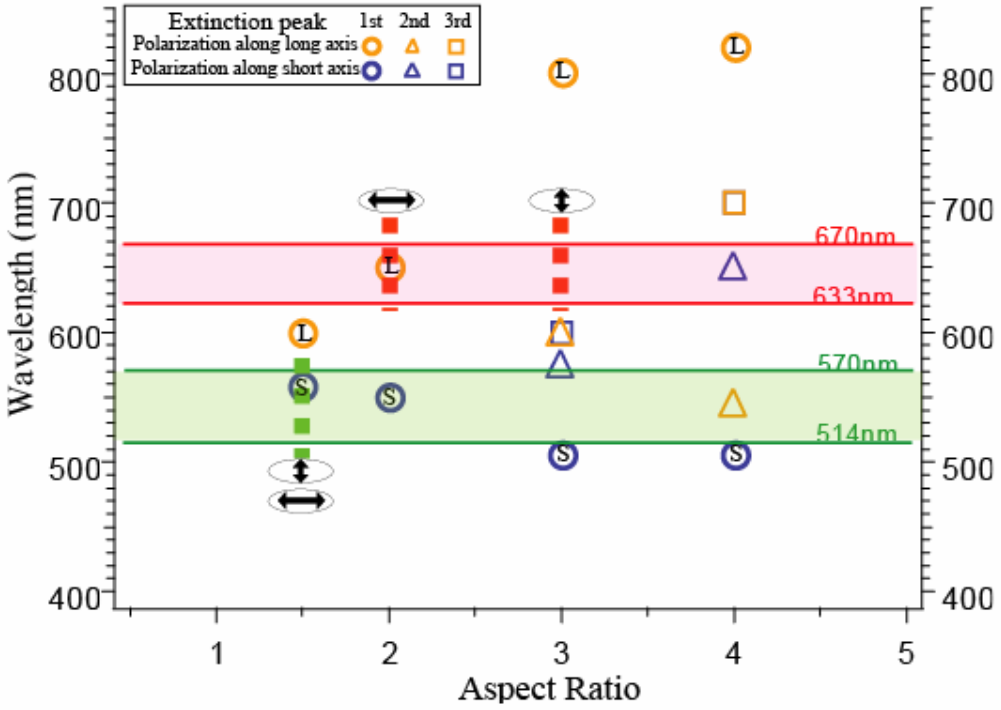

Figure 3.13: Comparison of measured peaks of extinction (orange and blue) and aspect ratios producing maximum fluorescence (green and red) plotted as function of length/width ratio.

3.5 Two-Dimensional Nanowire Structures

The main motivation for the work described in this section is to simplify the geometry to allow for quantitative comparison between calculations of the local electric field and fluorescence enhancement from anisotropic structures. A secondary motivation is to explore how the fluorescence enhancement be affected by 2D surface Plasmon waveguides and make contact with detailed studies of guided modes in a nanoscale metallic rectangular waveguide which have been reported recently [78-81].

In these studies we fabricated periodic silver nanowires onto an aluminum oxide-coated silicon substrate, varying the spatial period, and exploring the polarization dependence of fluorescence enhancement. SEM images of our structures are shown in Fig. 3.14. The polarization of the incident light in our scanning laser microscope is fixed by passing the light through a linear polarizer (the polarization is horizontal in images presented throughout this thesis); rather than rotate the plane of polarization, we effectively do measurements at two different polarizations simultaneously by fabricating nanowires with orthogonal orientations on the same substrate. Figure 3.14(c) shows scanning fluorescence microscopy images; the bottom two panels in the figure summarize the enhancement and reflectance intensity for excitation at 514nm (CY3 fluorophore) and for polarization of incident light both parallel and perpendicular to the long axis. The lateral periods for the nanowire arrays are indicated as fractions the excitation light wavelength, and vary between $\lambda/4$ and 2.5 λ.

The results show a strong polarization dependence of the enhancement, with the highest value occurring for the electric field vector perpendicular to the long axis of

the nanowire arrays. The optimum enhancement occurs for a spatial period of approximately half of the excitation light wavelength. On the same sample, we prepared arrays of silver nanopillars with square cross section, and with a similar range of spatial periods; as shown in Fig. 3.15. The optimum period is smaller, approximately quarter of the incident wavelength, and the enhancement ratio is around 4 times higher than that from line structures.

It is known that interaction of light with metallic nanoparticles result in extinction spectra that wavelength position and amplitude depend on the size of particles [32, 57]. It is common to provide the extinction or reflectance spectra for characteristics of particle-light interactions. Since the sample areas were very small, $(6um)^2$, and silver particle deposited on silicon wafer (non transparent), we were not able to measure directly extinction spectra. Reflectance images at extinction wavelengths were acquired and reflectance ratios relative to the substrate were calculated for each patterned array. Fig. 3.14(b) shows the reflectance images of silver periodic nanowires at wavelength 514 nm. As expected, the amount of reflected light from the array is dependent on both the period and polarization mode. Reflectance values greater than 1 indicate the amount of reflected light from silver patterns is actually more than that from substrate. In other words, those patterns with high reflectance act film-like property to the incident light. Darker areas indicate that

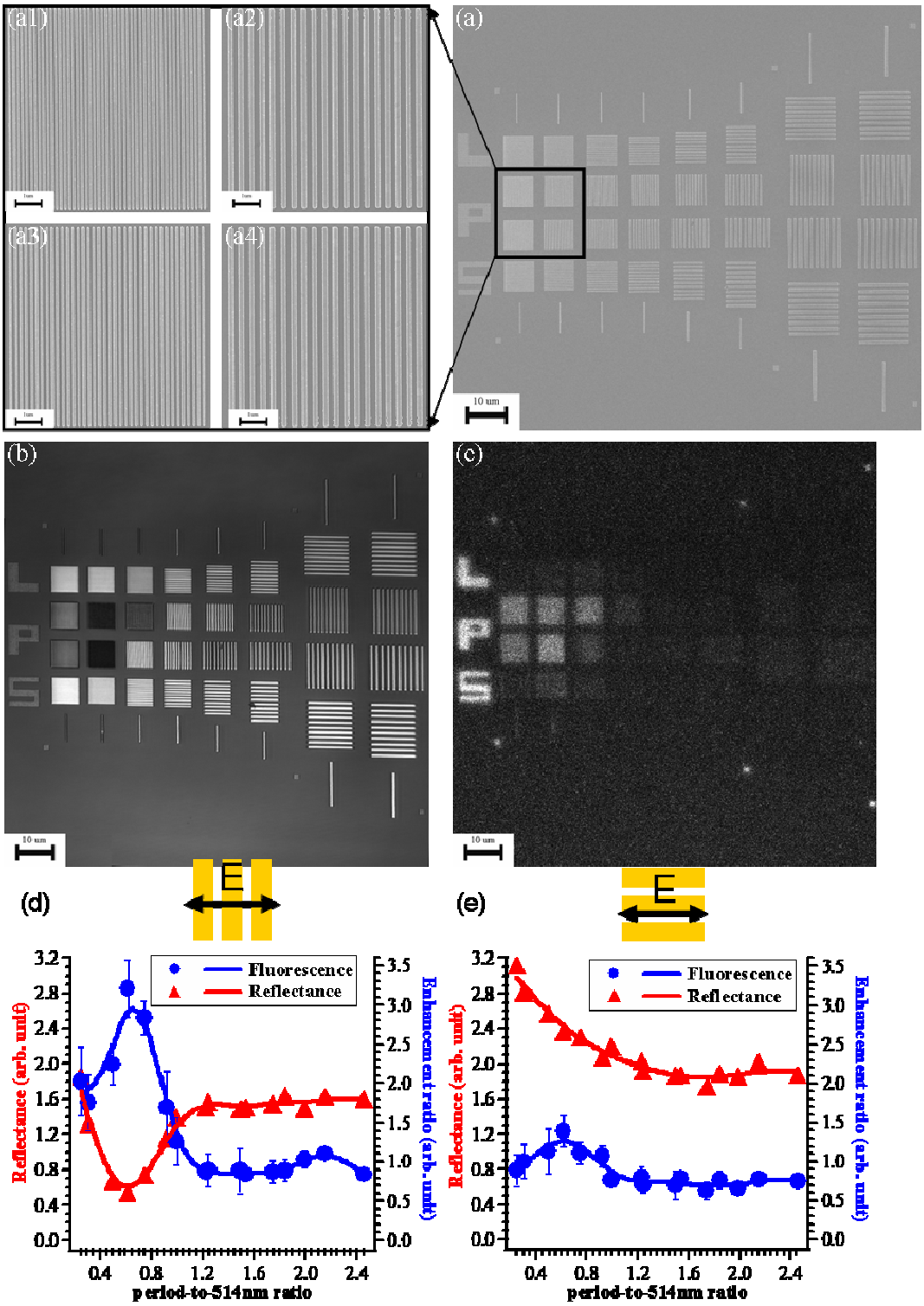

Figure 3.14: (a) Scanning electron microscope images of Ag nanowire structures; images

at the left are zoomed-in images to allow individual silver lines to be seen; (b) optical reflectance image for incident light wavelength equal to 514 nm; (c) Fluorescence map, for incident light wavelength equal to 514 nm; (bottom panels) quantitative analysis of fluorescence enhancement (blue) and reflectance intensity (red) for long axis of nanowire perpendicular (left) and parallel (right)to the electric field vector of the incident light. The period is defined as line width plus edge-edge spacing, and line width is equal to edge-edge spacing in this case. The change of line width from pattern to pattern in (a) is $\frac{1}{8}\lambda|_{514nm} \sim 64nm$ ***for top half and*** $\frac{1}{8}\lambda|_{633nm} \sim 79nm$ ***for bottom half pattern, and each half consists of longitudinal and transverse orientations plus single vertical line. The "LPS" navigation marks consist of arrays of silver nanopillars of square cross section, each 120 nm in width, and spaced at 220 nm center-to-center.***

silver nanowires absorb more light at 514 nm and the minimum reflectance corresponds to the maximum fluorescence enhancement at period approximately half of the incident wavelength along transverse polarization. All longitudinal patterns have reflectance higher than 1, and no significant fluorescence enhancement from this orientation. Similarly, in periodic square particles, patterns with periods located at local minimum in reflectance show local maximum in enhancement. However, the optimum enhancement is not at the period with the major minimum in reflectance. The following shows a comparison of field calculation and experimental result using FDTD method (Fig. 3.16).

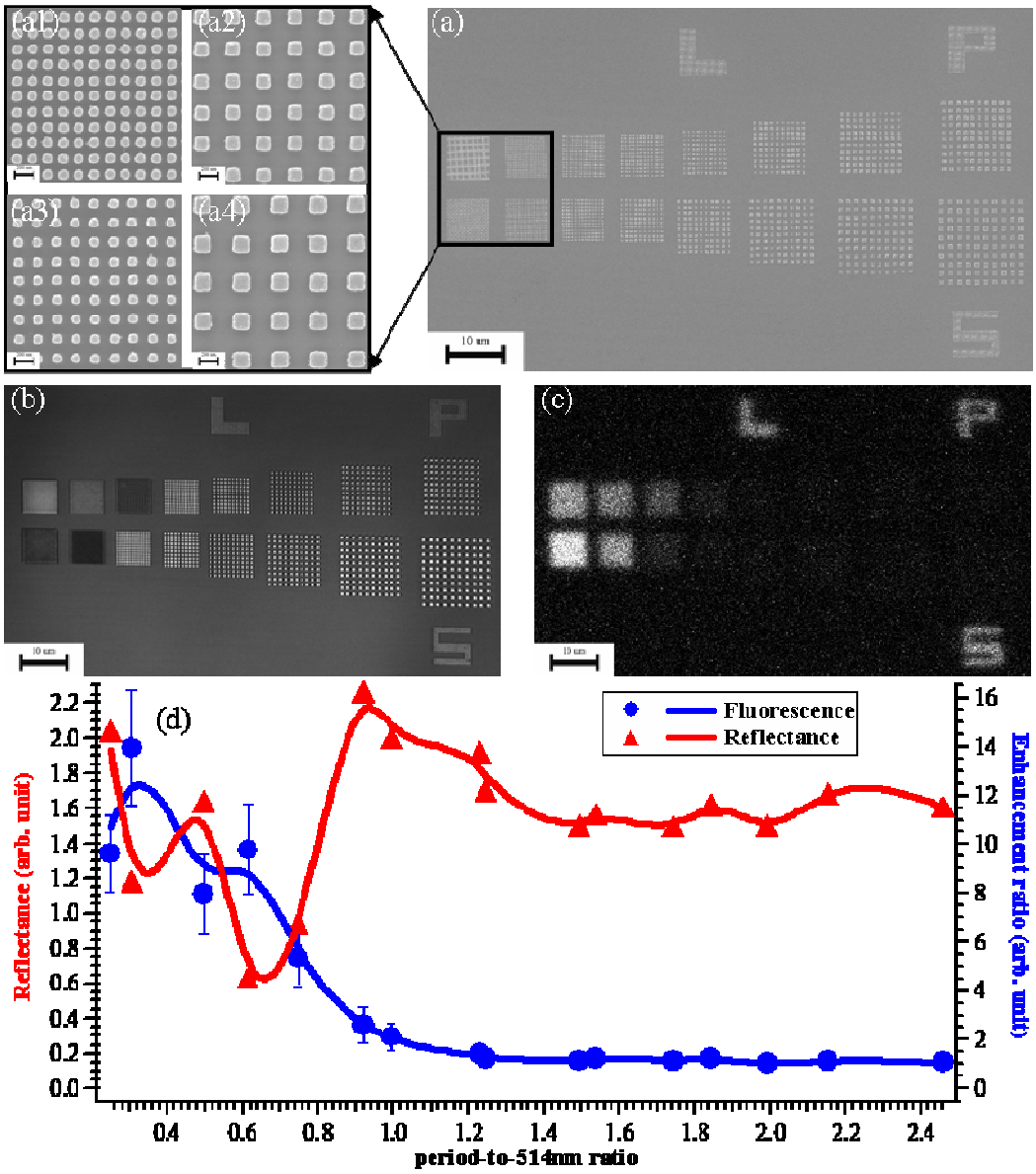

Figure 3.15: Scanning electron microscope images (a) with enlarged images to the left from patterns in the square mark on various periodic square silver nanoparticles, (b) Reflectance image with incident light 514 nm, (c) CY3 fluorescence map, and quantitative analysis of fluorescence enhancement (blue) and reflectance intensity (red) along two different orientations to the bottom two panel. The period is defined as particle width plus edge-edge spacing, and particle

width is equal to edge-edge spacing in this case. The variation of particle width is $\frac{1}{8}\lambda|_{514nm} \sim 64nm$ ***for top half and*** $\frac{1}{8}\lambda|_{633nm} \sim 79nm$ ***for bottom half pattern. The "LPS" navigation marks consist of array of silver nanopillars of 120 nm width and center-center spacing equal to 220 nm.***

The field distribution changes with the nanowire period. The summary plot shows the average intensity 8 nm above the sample surface, at the approximate position of the fluorescent tags, as indicated schematically by the purple dashed lines in figure 3.16(a). A comparison of the measured fluorescence and calculated field intensity by FDTD shows qualitative consistency: both are larger for the polarization perpendicular to the nanowires. The major peak in both plots occurs at a period approximately half of the wavelength. Therefore, we may conclude that the near field, local electric field near the particles, has a strong influence on enhanced fluorescence. We also summarize analysis on CY5 fluorophore, and properties are qualitatively consistent with what we observe in CY3 except smaller and red-shifted of the optimum enhancement to larger period. Enhancement dependence is also captured by the field calculation (Fig. 3.17).

It is well-known that the local field will be enhanced at the sharp tip or edge, so called the lightning rod effect. Recent measurements of extremely large enhancements of Raman scattering have been interpreted as pointing to the importance of "hot spots", i.e., regions of very high field [22, 56]. We also see this effect along transverse orientation on the large wire period on which details can be easily resolved by the instrument. Taking a wire period of 1.9 μm, with the wires

perpendicular to the light polarization ("transverse" orientation) as a specific example, we can line up line profiles taken from reflectance and fluorescence image (Fig. 3.18) with higher magnification and lower attenuation, and easily find out the bright region which is actually on the edge of the bars. However, we don't observe a similar effect along the other polarization. Since the silver wires here are wide as 1 μm, they may act as a bunch of silver film, and edge effect dominates the field distribution at those film edges, which we don't see in the field calculation (Fig. 3.18(d)). Therefore, fluorescence enhancement is polarization dependent and the lightning rod effect may alter local field distribution at the edge of the structures.

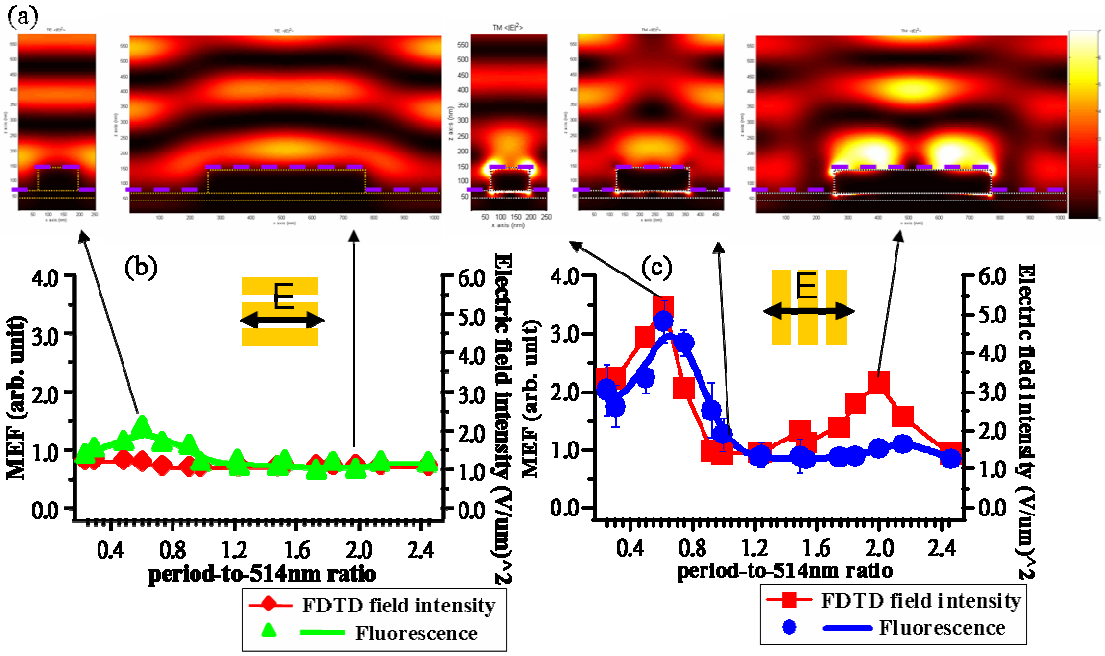

Figure 3.16: Field intensity calculation by 2-dimentional FDTD method and examples are as shown in (a). Summary plots (b), (c) of average field intensity 8nm above the surface as pointed out by the purple dash lines where the fluorophores locate compared with fluorescence enhancement along two different polarizations.

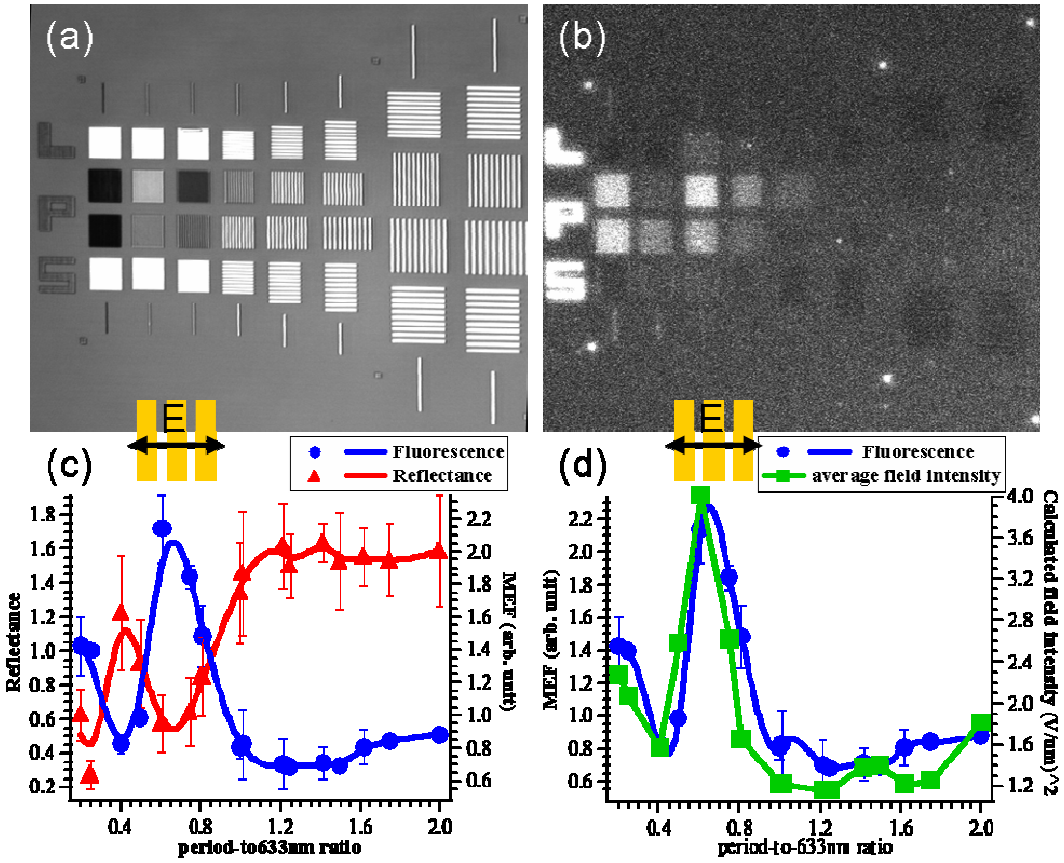

Figure 3.17: Summary of variation of (a) reflectance and (b) fluorescence for Ag nanowire arrays with an excitation wavelength of 633 nm (Cy5). Summary analysis along transverse mode between fluorescence and reflectance (c), and calculated (FDTD) average field intensity 8nm above sample surface (d).

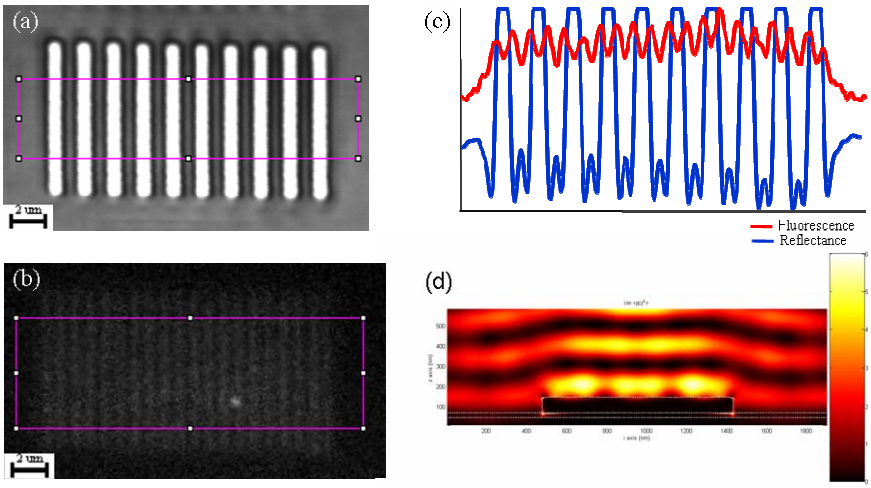

Figure 3.18: ***(a) Reflectance and (b) fluorescence images for incident light wavelength of 514 nm, and a Ag wire period of 1.9 μm (line width: 950 nm); (c) intensity line profiles from the marked purple rectangle regions on previous two images; (d) calculated (FDTD) field intensity for a 1.9 μm period silver wire array on a Si substrate.***

3.6 Enhancement from periodic nanowires with fixed line widths

As described in previous section, our results show a strong polarization dependence of the enhancement. We can easily pick out the optimum condition is for the polarization perpendicular to the long axis: the optimum period is approximately half of the incident wavelength. It is also of interest to explore the dependence of the enhancement on various lateral spacing periods with a fixed silver line width. By fabricating silver nanowires with different gap distances, one might expect that above a certain spacing there will be weak field overlap between proximal stripes, and the

main effect of the array will be to provide a reciprocal lattice vectors, G, at the surface; in this limit the metal nanowires would act as elementary dipole oscillators [59] each having a local particle Plasmon resonance transverse to the wire [58]. A schematic view of such a silver photonic crystal slab, with line width of 192 nm is depicted in Fig. 3.19(a), and several scanning electron microscope images to show top view of the pattern. We take measurements at two different polarizations simultaneously by fabricating the nanowires with two different orientations on the same sample. Fig. 3.20 shows the reflectance image (a) of the excitation wavelength (514 nm for CY3) and fluorescence map (b). As we expected, the optimum condition is for the polarization perpendicular to the long axis, and the optimum period is still approximately half of the incident wavelength, and it manifests itself as a minimum in the reflectance of the excitation wavelength. We also carried out field calculations by the FDTD method and extracted the average field intensity 8 nm above the surface where the fluorophores were located. Comparing the results with the average field calculation as shown in Fig. 3.21, the first maximum average field intensity coincides with the optimum enhancement, but there are other average field intensity peaks at period 704 nm, and 1088 nm, exactly twice the line width (384 nm) in step apart from the first peak, with no significant enhancement shown in the measurement. The second maximum local field intensity should be corresponding to higher resonance mode in particle Plasmon resonance; therefore, the supplied reciprocal lattice G vector may be able to couple with the fundamental resonance frequency at the first peak with smaller period and couple with the secondary at the next peak after two discrete steps of line widths, so on so forth. From section 3.1, we've known that there

is not only red-shift in particle Plasmon resonance for larger particle size, but also the field distribution is no longer dipole-like , but a mixture with higher order modes, such as quadruple. Modes other than the dipole are expected to be essentially non-radiative and not to contribute to fluorescence enhancement.

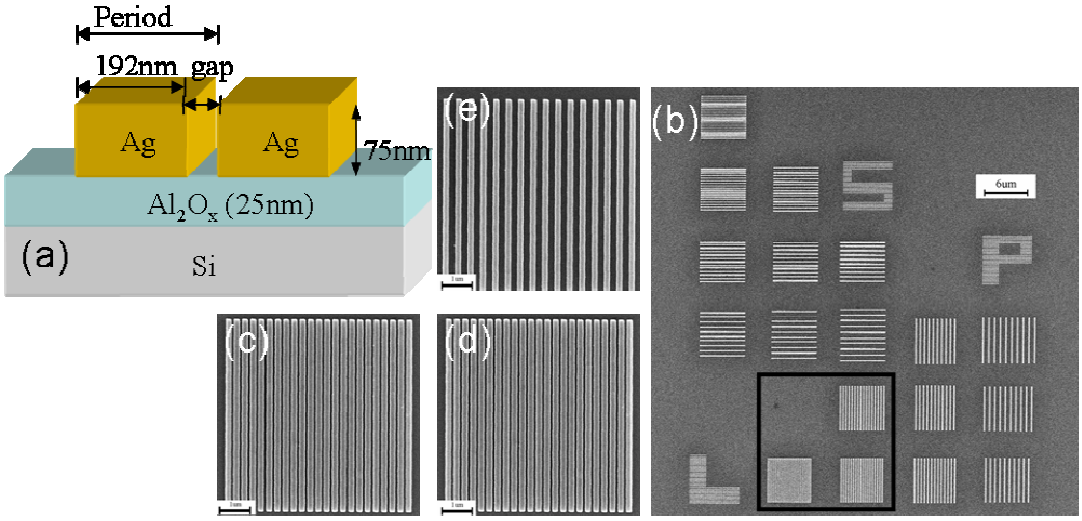

Figure 3.19: (a) Schematic cross-section view of Ag nanowires sample; (b) Scanning electron microscope image of Ag nanowire sample (c)-(e) magnified SEM images (with scale bar 1 um) of 192 nm width nanostripes with various periods: (c) 256 nm , (d) 320 nm , (e)384 nm. All the stripes in the lower right corner of (b) have a vertical orientation, coupling a transverse mode plasmon to the horizontally polarized incident light, and those in the upper left of (b) have a horizontal orientation, coupling a longitudinal plasmon mode to the incident light. The "LPS" navigational marks are made up of arrays of square silver nanopillars 120 nm in width, spaced at 220 nm center-to-center.

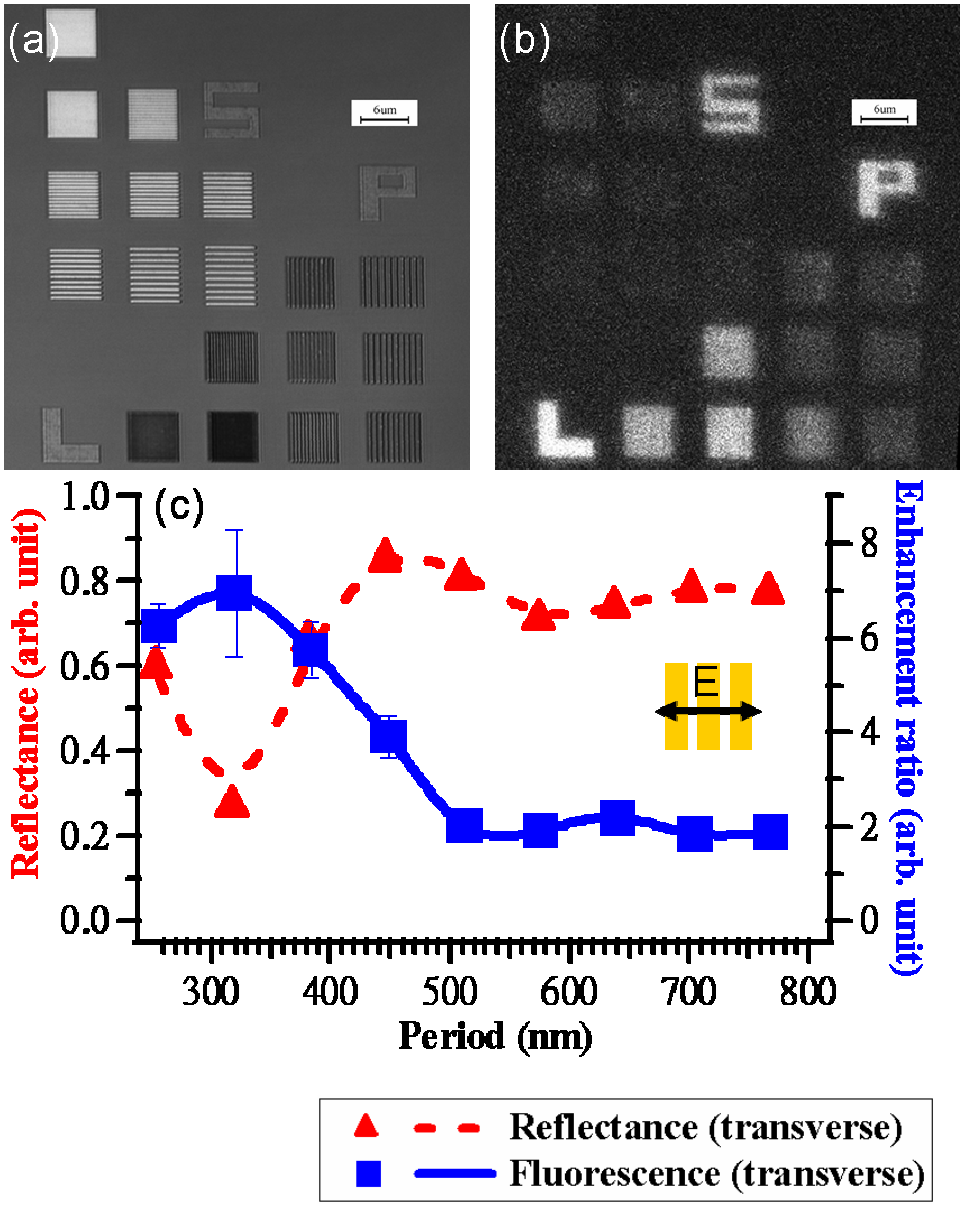

Figure 3.20: (a) Reflectance and (b) fluorescence images for 514 nm wavelength incident light (Cy3) at the pattern as shown in Fig. 3.19(b) design. (c) Summary plot of reflectance and fluorescence enhancement on the pattern with the light polarization orthogonal to the wires (transverse mode).

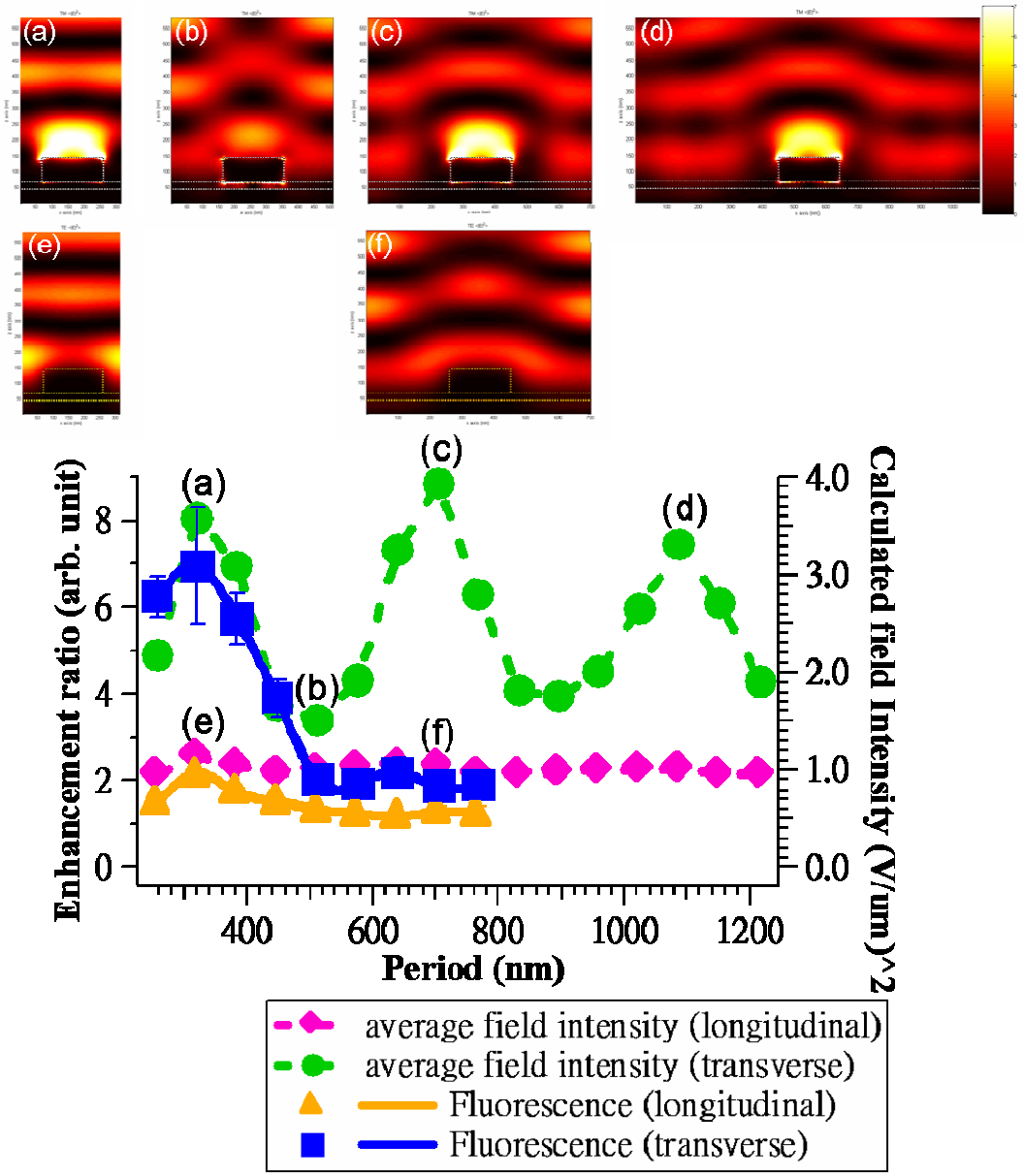

Figure 3.21: ***(Top) Field intensity, as calculated by a 2-dimentional FDTD method; examples are as shown along transverse/longitudinal polarization. Periods are as labeled. (Bottom) Summary plots of average field intensity (magenta, green curves) 8nm above the surface (fluorophore position) compared with fluorescence enhancement along longitudinal and transverse polarizations (yellow, blue curves).***

3.7 Effect of spacer layer between nanowires and Ag film

There have been reports in the literatures [14] [16], suggesting it is possible to have the local plasmon resonance couple to a traveling plasmon by introducing a metallic plane beneath the nanostructures [60, 61], and indeed it is well-known that the interaction between electromagnetic radiation and electric dipole resonances can be strongly altered in the presence of a nearby reflecting metal surface [62]. The strength of the coupling can be modified by introducing a spacer layer of a chosen thickness.

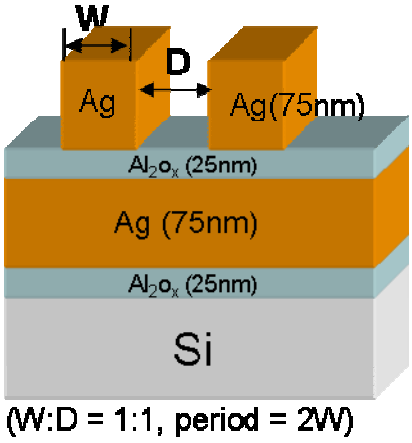

Figure 3.22: Schematic cross-section view of the sample with periodic nanowires spaced from silver ground plane by a 25 nm thick oxide spacer layer.

To test the effect of varying this coupling on fluorescence enhancement, we fabricated silver nanowires on an aluminum oxide spacer layer deposited over a silver film. The geometry is shown schematically in figure 3.22. In these investigations we varied both the lateral spatial period of an Ag nanowires array and thickness of the oxide layer which spaces it above the underlying film systematically; the goal was to explore both the role of plasmon coupling to the underlying Ag film as well as the

polarization dependence of the fluorescence. Following the procedure described earlier, we effectively recorded fluorescence measurements at two different polarizations simultaneously by fabricating arrays with nanowires arranged at various spatial periods along two orthogonal directions.

We find that the measured fluorescence enhancement ratios from nanowires arrays spaced 25 nm above an underlying Ag film is indeed much higher than in the absence of the Ag plane; this is especially so for the incident light polarization perpendicular to the nanowires (figure 3.24). The optimum period is still approximately half of the wavelength of the incident light, but the enhancement ratio is increased to approximately 50 fold (Fig. 3.24(c)). An even larger enhancement, approximately 90 fold (Fig. 3.23), is found for square nanoparticles at an excitation wavelength of 514 nm (CY3) at the same period. We have found qualitatively consistent results for excitation at 633 nm (Cy5), however with a slightly larger optimum period and lower overall enhancement ratio, as described in section 3.5.

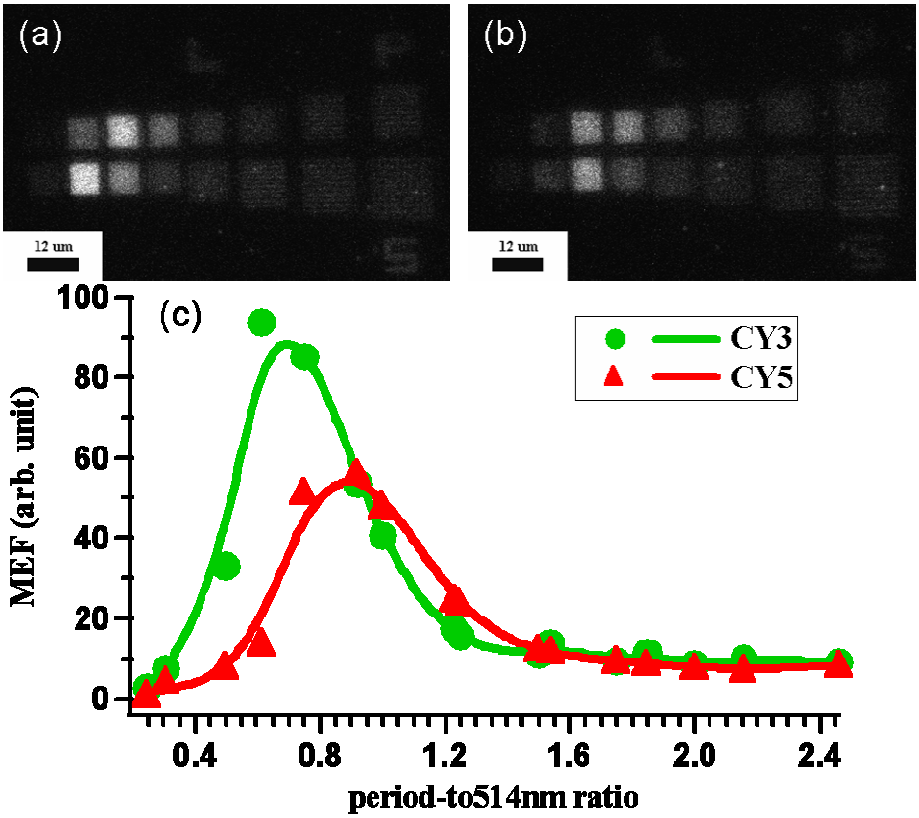

***Figure 3.23:** Fluorescence maps for arrays of square nanoparticles over ground plane with spacer layer 25 nm on CY3 (a) and CY5 (b). A summary plot (c) of enhancement ratio as a function of lateral periods, ranging from 0.25 to 2.4 times of incident wavelength.*

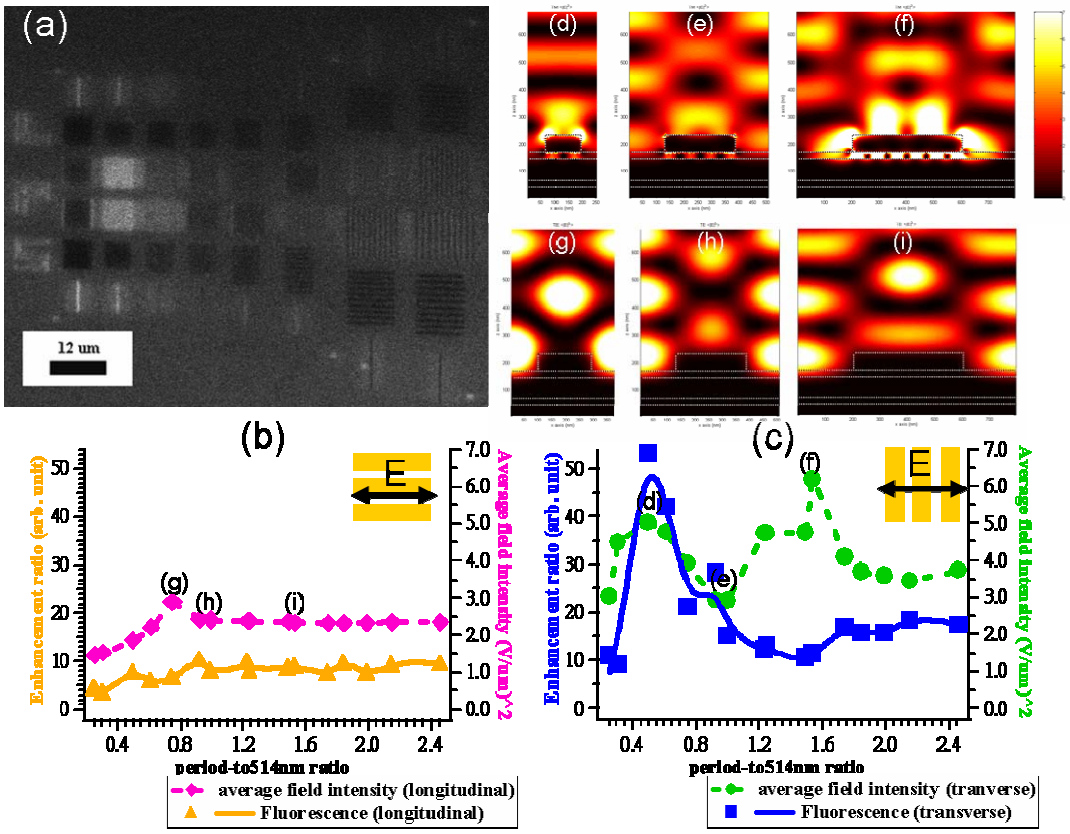

Figure 3.24: ***Enhanced fluorescence from arrays of silver nanowires spaced above a Ag film by 25 nm of aluminum oxide. (a) Fluorescence map for 514 nm wavelength excitation (CY3); summary plots of enhancement ratio and calculated (FDTD) average field intensity along longitudinal (b), transverse (c) polarizations. Field intensity maps at labeled periods along (g) - (i) longitudinal polarizations, (d) - (f) transverse polarizations.***

Figs. 3.24(d) ~ (i) show the results of calculations of the local electric field intensity for Ag nanowires spaced above a Ag slab, carried out using a 2-dimensional FDTD code. As shown in Figs. 3.24(d) ~ (f), the field intensity distribution varies

with spatial period, and leads to oscillations in the average intensities determined at the position of the fluorescent tags, 8nm above the surface. As mentioned above, we are interested in the possibility of resonant coupling between the local plasmon and the traveling plasmon to the underlying ground plane, and indeed there is direct evidence of this in Figs. 3.24(d) ~ (f), with strong field intensity localized in the region between the silver line and the underlying ground plane. These regions of strong field intensity occur for transverse polarization; they are absent for longitudinal (Fig. 3.24(g) ~ (i)) polarization, resulting a weaker coupling, and a polarization-selective enhancement in fluorescence, as seen in Fig. 3.24(b), (c). The calculated field intensity reproduces the peak in the fluorescence enhancement for a spatial period near on half the wavelength of the incident light, but also predicts a second peak near three halves the wavelength, which is not seen experimentally. While the agreement is only semi-quantitative, our results indicate that it is essential to include the spatial distribution of the field near nanostructures into the consideration for optimizing fluorescence employing noble metallic nanostructures.

Additional evidence of the importance of coupling between Ag nanowires and an underlying Ag film in enhanced fluorescence comes from measurements from isolated wires. In the images shown earlier, in Fig. 3.14, (section 3.5) for isolated lines in the absence of the Ag film there is no obvious enhancement. In contrast, as shown in Fig. 3.25, a significant enhancement occurs from isolated nanowires when spaced above silver film; this figure shows a series of intensity profiles across wires of increasing width, ranging from 64 nm to 633 nm*. Ag nanowires with small line

widths produce high fluorescent intensity above the wire, while those with large line widths produce dips in the intensity above the bar instead. We find a similar effect, local dips in intensity above periodically spaced nanowires in some cases, as shown in Fig. 3.26. Although the maps are dark for wires oriented parallel and perpendicular to the direction of polarization, they are brighter between the wires for transverse polarization, i.e. the optimum polarization for a 25 nm thick aluminum oxide spacer layer.

* All isolated stripes are more than 2 um apart.

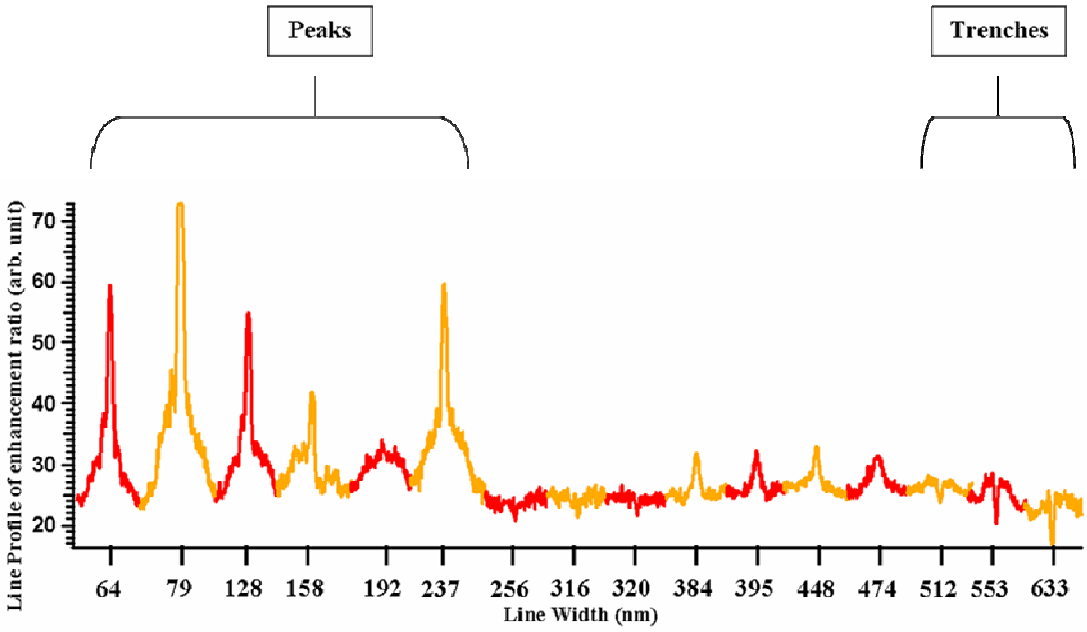

Figure 3.25: Intensity line profiles across isolated silver nanowires as a function of line widths. Differentiation from one line profile to the next based on colors, red and orange.

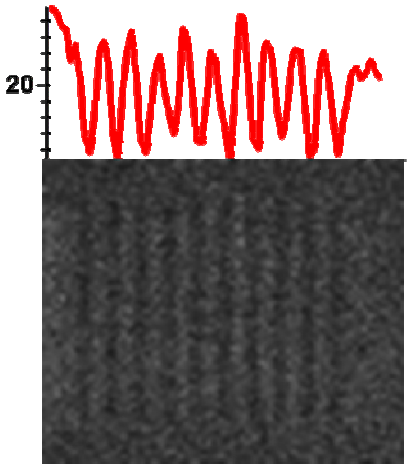

Figure 3.26: (top) Fluorescent intensity profile and (bottom) fluorescence image for excitation at 514 nm for Ag nanowires 633 nm in width, oriented transverse to the direction of polarization.

The results presented in this section indicate that coupling between nanowires and an underlying Ag film is indeed important, and can result in a significant increase in the fluorescence enhancement. In the next two sections we examine the result of varying the thickness of the spacer layer between Ag nanowires and an underlying Ag film. We finish this section with one final set of observations for related structures, arrays of square nanopillars.

Figure 3.27 shows what is seemingly an example of the lightning-rod effect mentioned above; the fluorescence images are for an array of square Ag nanopillars with a lateral period of 1.266 μm. These maps show higher intensity between pillars. Interestingly, in Fig. 3.27(b), which is the fluorescence maps for 633 nm excitation, pronounced bright edges along the direction of the polarization are evident. Such features are absent in Fig. 3.27 (a), which is for excitation at 514 nm. We will show additional examples of this effect in section 3.9.

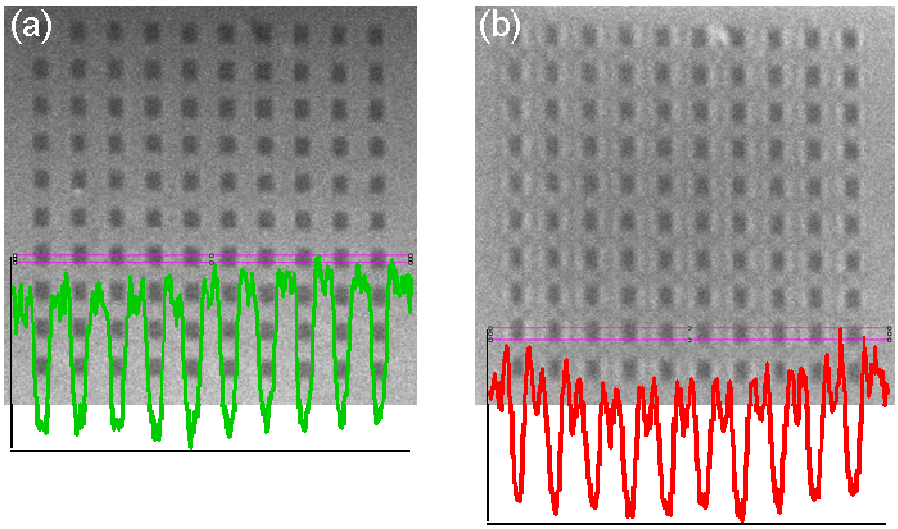

Figure 3.27: Fluorescence images acquired for optical excitation at (a) 514 nm, and (b) 633 nm, for an array of square silver nanopillars spaced at a period of 1.266 μm, i.e. twice the incident wavelength in (b). The green and red curves are intensity profiles, taken from the rectangular regions marked in purple.

3.8 Zero Spacer Limit: Enhancement from corrugated Ag Film

If the spacer layer thickness is reduced to zero, the result is effectively a corrugated Ag film. Systems which are composed of a dipole-active layer placed in front of a metal mirror have been extensively investigated [60, 61], especially in SERS [64, 65]. In this section, we explore the fluorescence enhancement from the corrugated silver surface [63] consisting of small periodic grating produced by electron-beam lithography. As in previous sections, fluorescence measurements at two different effective polarizations by orienting the log axis of the corrugations parallel and

perpendicular to the electric field vector of the incident light. For the corrugated film we find that the measured fluorescence enhancement ratio is higher than that for nanowires without the ground plane, but less than those with oxide layer of 25 nm between the structures and the ground plane; this is especially so for the excitation polarization perpendicular to the nanowires (figure 3.28). The optimum period is again approximately half of the wavelength of the incident light; the maximum enhancement is approximately 20 fold, as seen in Fig. 3.28(b). Much larger the maximum enhancement ratios, up to approximately 140 fold are obtained for a corrugated Ag surface consisting of square Ag nanopillars on a Ag film at the same period as seen in Fig. 3.29(c) for excitation at 514 nm, and roughly the same spatial period.

Figs. 3.28(d) ~ (i) show the results of calculations of the electric field intensity for linearly corrugated Ag films, using a 2-dimensional FDTD method and incident light along two polarizations. As shown in figure 3.28(d) ~ (f), the field distribution varies with spatial period, which leads to a variation in the average intensity determined at the height of the fluorescent tags, 8nm above the surface. These calculations reproduce the polarization dependence but not the optimum period.

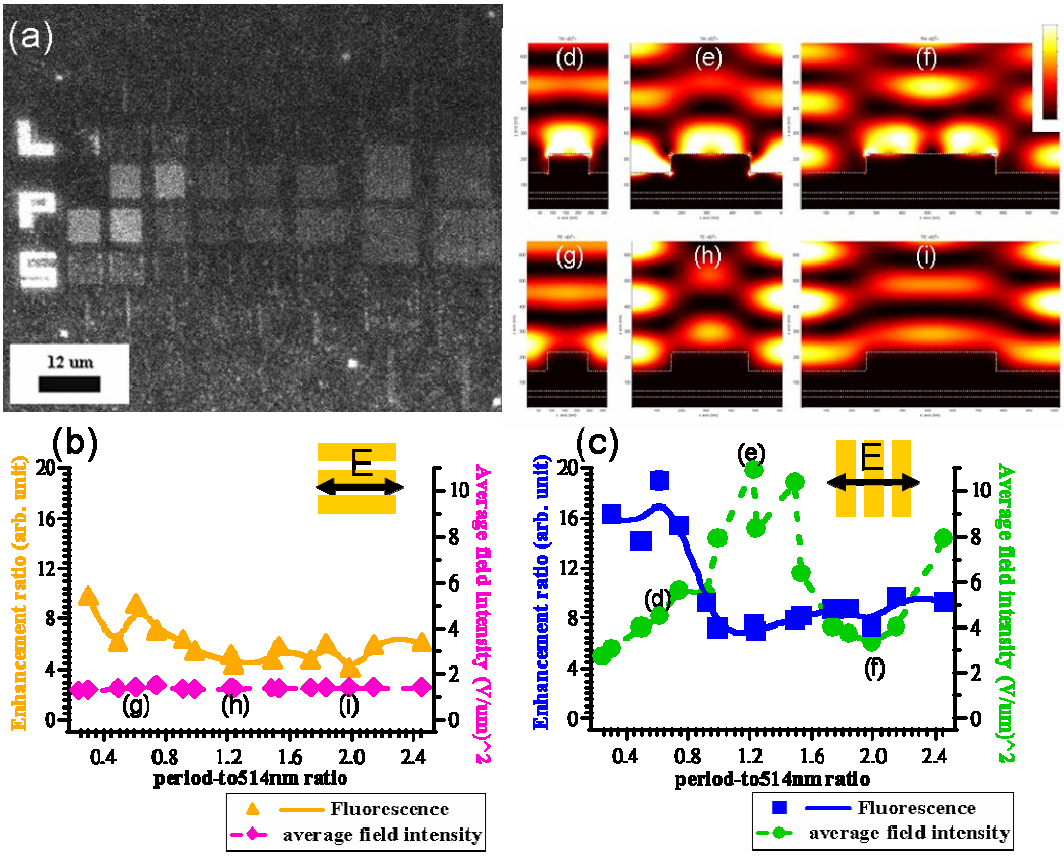

Figure 3.28: Enhanced fluorescence from corrugated surfaces consisting of arrays of silver nanowires deposited on a Ag film. (a) Fluorescence map of overall sample, measured with an excitation wavelength of 514 nm (Cy3); (b), (c) summary plots of enhancement ratio and calculated (FDTD) average field intensity with (b) longitudinal, (c) transverse polarizations; (d)-(i) field intensity maps at indicated periods for (g) - (i) longitudinal, and (d) - (f) transverse polarizations.

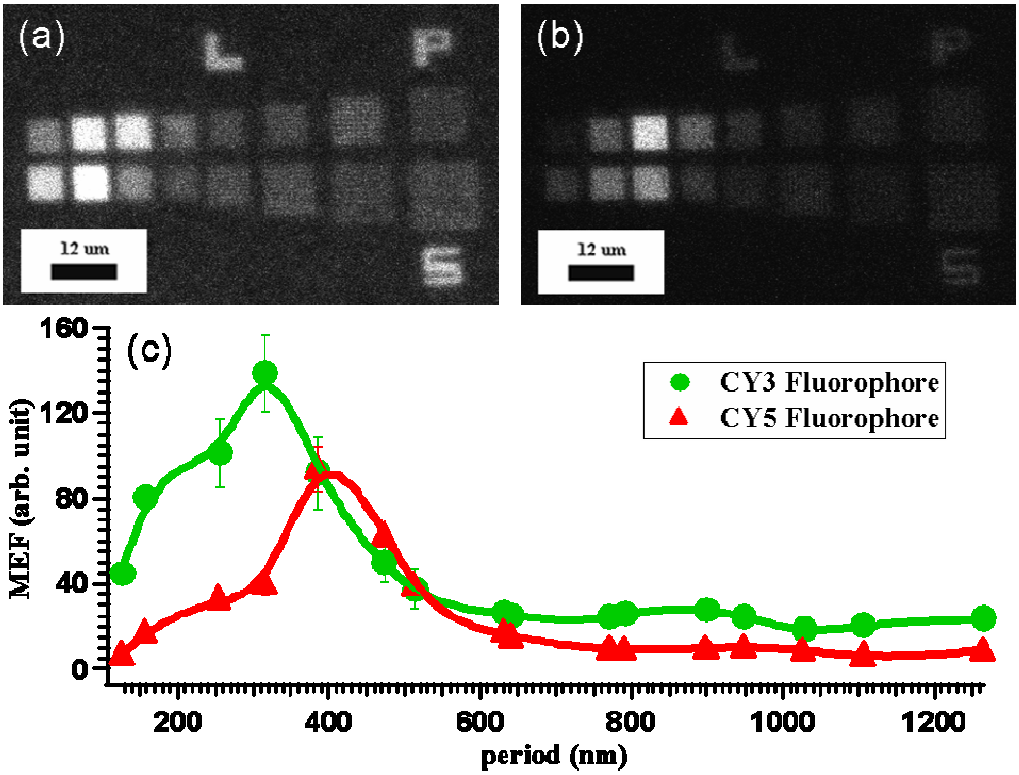

***Figure 3.29:** Fluorescence maps for array of square nanoparticles on ground plane without spacer layer for optical excitation at (a) 514 nm and (b) 633 nm; (c) summary plot of enhancement ratio as a function of lateral periods, ranging from 128 nm to 1.26 μm.*

3.9 Thick spacer layer

In the previous 2 sections, we demonstrated that an additional enhanced of fluorescence from Ag nanostructures is possible in the presence an underlying Ag film. In this section we investigate the tunability of this effect by increasing the spacer layer thickness. We fabricated silver nanowires on an aluminum oxide spacer 80 nm in thickness pre-deposited on a silver layer. The measured fluorescence

enhancement ratio in this case is again much higher than for Ag nanowires without the underlying Ag film. However, in this case the maximum enhancement, of approximately 100 fold occurs for the incident light polarization *parallel* to the nanowires as seen in figure 3.30. Significantly the sense of the optimum polarization has *switched*, in increasing the oxide thickness from 25 nm to 80 nm. The optimum period again shifts as the excitation wavelength of the incident light is changed from 514 to 633 nm. Finally, the maximum enhancement ratio for excitation at 514 nm and square nanopillars over an increase to approximately 120 fold for this spacer thickness, again at a period approximately half of the wavelength of the incident light (fig. 3.32).

Field calculations for this geometry based on the 2-dimensional FDTD method are presented in Figs. 3.30(d) ~ (i). As shown in Figs. 3.30(g) ~ (i), the field distribution varies with spatial period, which again leads to different average intensities at the height where the fluorescent tags reside. We no longer see the same regions of intense electric field between the wires and film for transverse polarization at this larger spacer layer thickness. Instead the fluorophores are *lifted up into the strong field region* between the wires for the longitudinal polarization, the optimum polarization for this particular spacer layer thickness. Furthermore, the optimum polarization can also be tunable by period of the nanowires, not merely by spacer layer thickness (Fig. 3.31). Although we don't yet have detailed explanations on the optimum period discrepancy, our results indicate that it is essential to include the spatial variation of the spacer layer over the ground plane in the calculation for tuning the optimum polarization.

What we observed before about the bright edge in previous sections (spacer layer 25 nm) with a large square period, the edge effects are only observed with the transverse orientation and for CY5. Take the same square period 1.266 um as an example; we now have the bright edges along the opposite orientation from CY3 instead from CY5 fluorescence map, and it is the same optimum polarization as we discussed on nanowire structures (fig. 3.33).

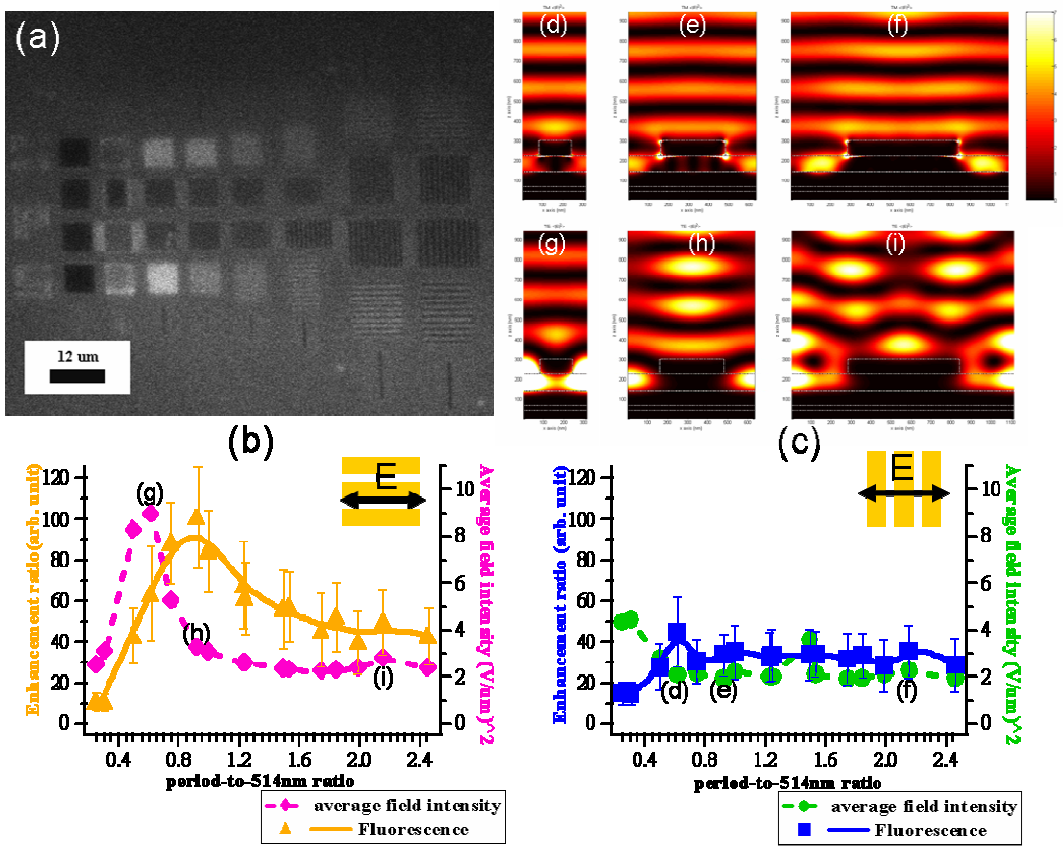

Figure 3.30: Fluorescence (CY3) enhancement from arrays of silver nanowires separated from an underlying Ag film by an aluminum oxide layer 80 nm in thickness. (a) Fluorescence map of entire sample; (b), (c) summary plots of

enhancement ratio and calculated (FDTD) average field intensity for (b) longitudinal and (c) transverse polarizations; (d) – (i) field intensity maps at indicated spatial periods along (g) - (i) longitudinal, (d) - (f) transverse polarizations.

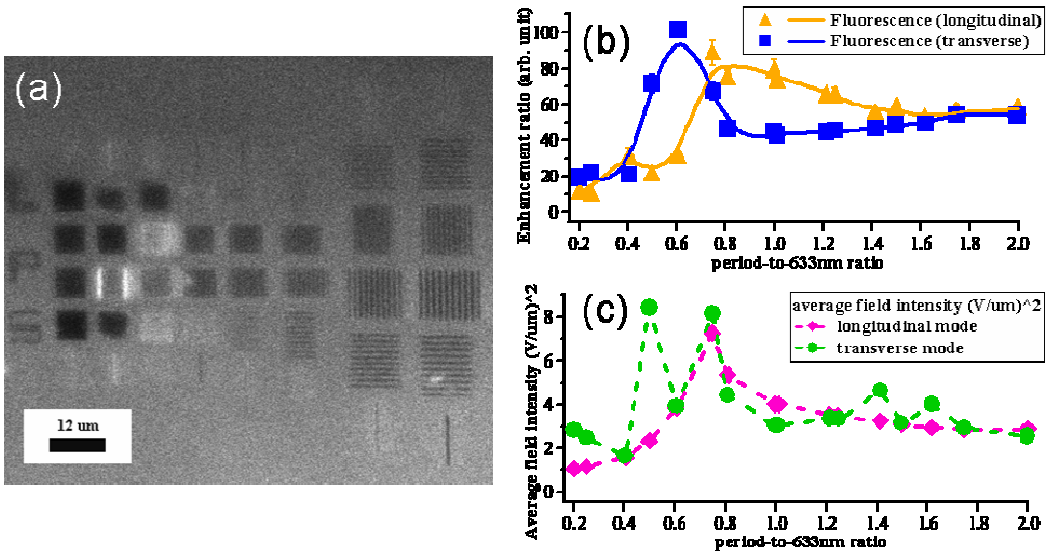

Figure 3.31: Fluorescence (CY5) enhancement from arrays of silver nanowires separated from an underlying Ag film by an aluminum oxide layer 80 nm in thickness. (a) Fluorescence map of entire sample; (b) summary plots of enhancement ratio and (c) calculated (FDTD) average field intensity for longitudinal and transverse polarizations as a function of lateral period, ranging from 0.2 to 2 times 633 nm.

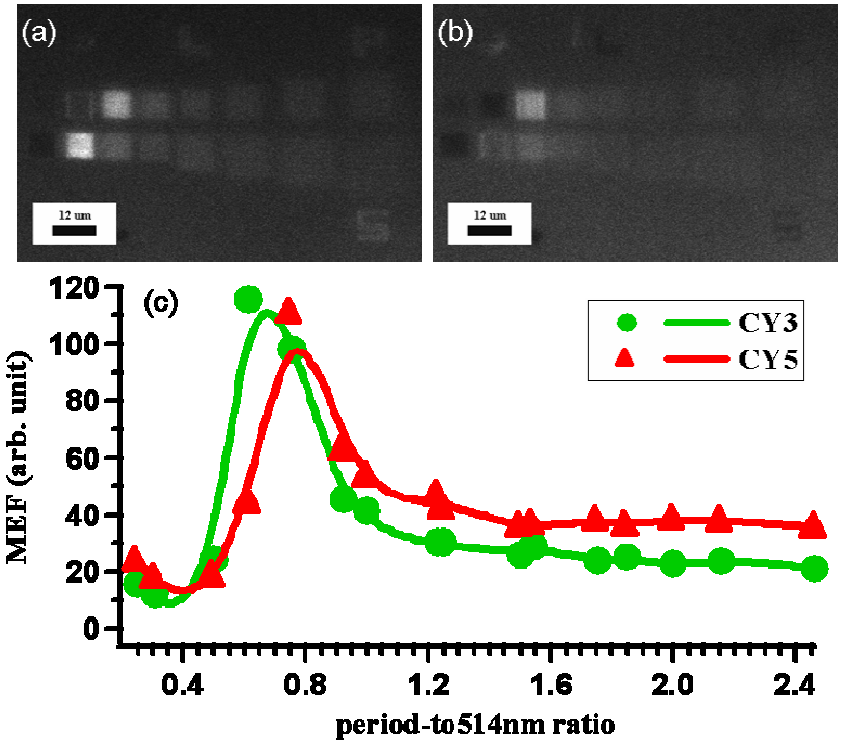

***Figure 3.32:** Fluorescence maps for array of square nanoparticles separated from an underlying Ag film by an aluminum oxide layer 80 nm in thickness for excitation at an optical wavelength of (a)514 nm (Cy3) and (b)633 nm (Cy5); (c) summary plot of enhancement ratio as a function of lateral period, ranging from 0.25 to 2.4 times 514 nm.*

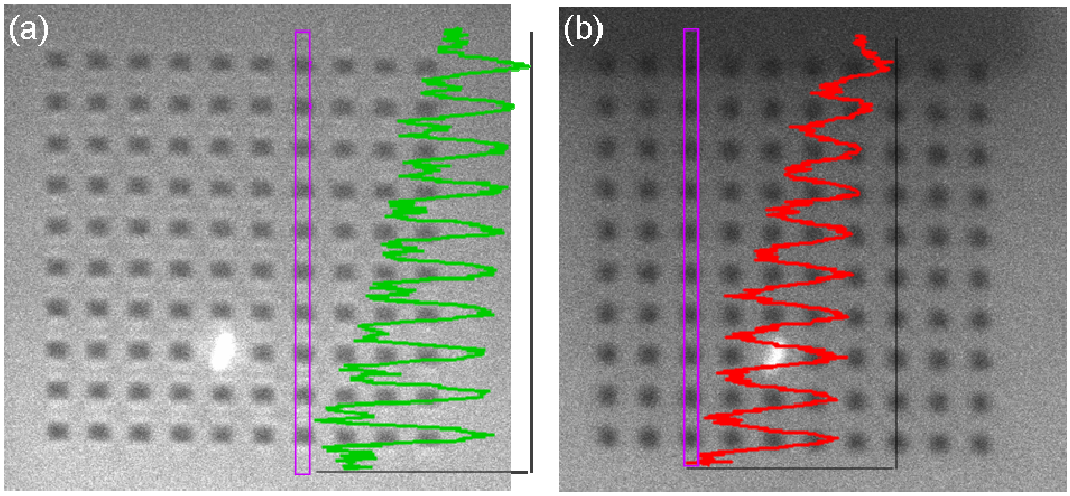

Figure 3.33: Fluorescence images from square silver nanoparticles spaced with lateral period 1.266 μm and separated from an underlying Ag film by an aluminum oxide layer 80 nm in thickness; incident light excitation wavelength (a) 514 nm (Cy3), and (b)633 nm (Cy5), which is One line profile for each image is taken from the purple rectangle region. Colored curves show fluorescence intensity profiles.

3.10 Oscillatory behavior in optimum polarization

In this final results section we discuss the overall spacer layer thickness dependence of the fluorescence enhancement from Ag nanowires above an Ag film. Our results show that as we continue increasing the spacer layer thickness, the optimum polarization direction switches between parallel and perpendicular to the silver nanowires twice in the region we explored, as shown in figure 3.34. We also find that the enhancement ratio falls off quickly after oxide thickness 100nm. As discussed above, the optimum polarization is perpendicular to the lines for a thin

spacer layer of 25nm, then switches to parallel as the spacer layer was increased to 80nm. As seen in Fig. 3.34, the optimum polarization switches back to perpendicular for a spacer layer thicker than 140nm. We interpolate the experimental data points (as shown in solid dots in Fig. 3.34) by smoothing spline with smoothing factor 1 along longitudinal and 5 along transverse polarization.

Our field calculations by FDTD capture part of this behavior, as described in previous two sections, and as summarized in Fig 3.35. The field distribution is qualitatively different for two different polarizations. There is more intense region above the lines than in between the lines for the perpendicular polarization, and that is opposite for the parallel polarization. Although the fluors are only 8nm above the surface, we don't have particularly strong enhancement for the parallel polarization. More importantly, we have the strong coupling at the region in between the line and the ground plane for the perpendicular polarization as shown in figure 3.35(b). As the spacer layer is increased to 80nm, the coupling is much less for the perpendicular polarization, and the fluorophores would be lifted up into the strong field in between the lines for the parallel polarization. This explains the interchange of which polarization shows the highest fluorescence intensity.

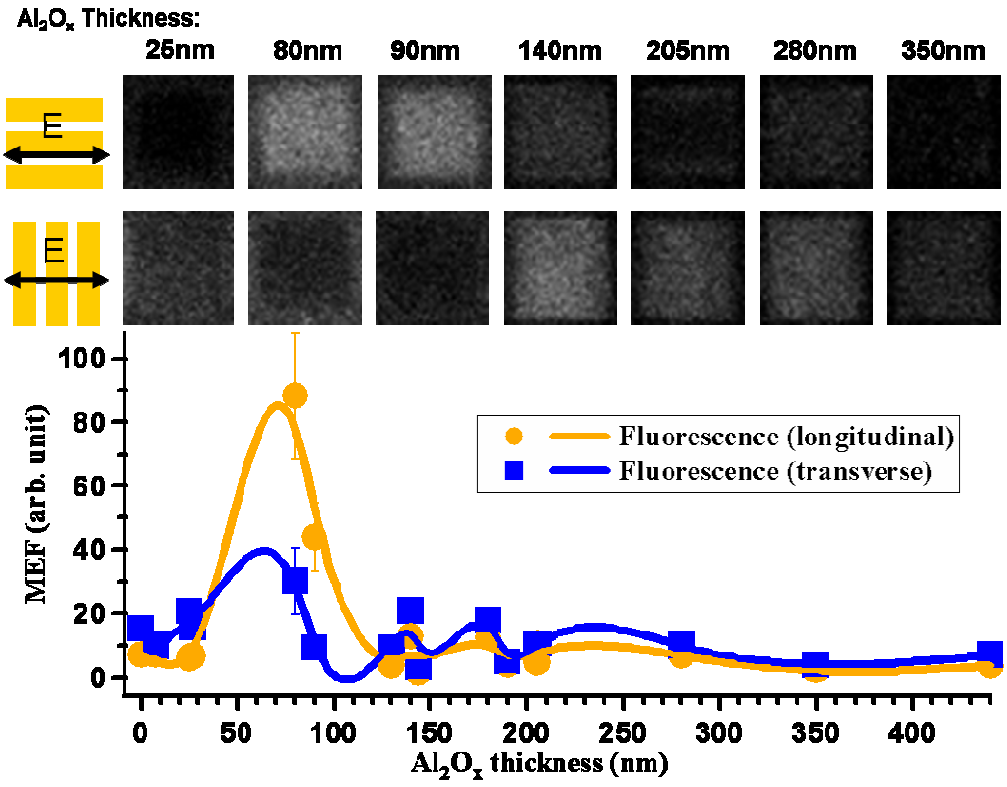

Figure 3.34: (Top) measured fluorescence (CY3) images for Ag nanowires spaced above an underlying Ag film for excitation at 514 nm (field of view approximately 7um); (bottom) summary plots of enhancement ratio for longitudinal and transverse polarizations as a function of spacer layer thickness, ranging from 25nm to 400nm. Nanowire period is 0.75 times the excitation wavelength.

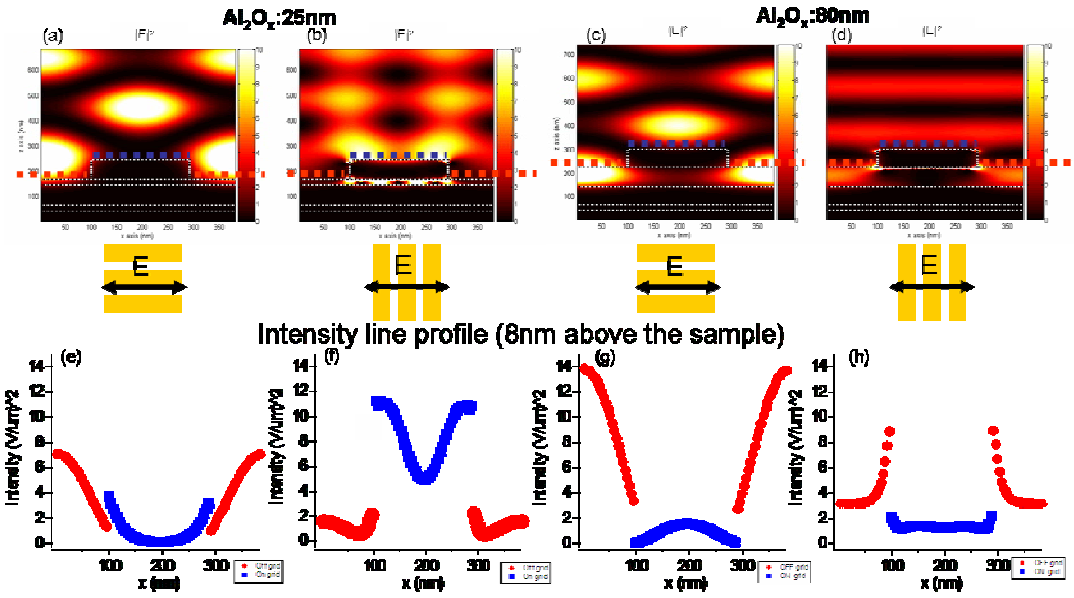

Figure 3.35: Field calculations Ag nanowires spaced above an underlying Ag film for excitation at 514 nm by using a 2-dimensional FDTD method; (a),(b) field intensity distribution for longitudinal and transverse polarization, oxide spacer layer thickness 25nm; (c),(d) field intensity distribution for longitudinal and transverse polarization, oxide spacer layer thickness 80nm; (e),(f) field intensity 8nm above the surface (dashed lines in (a),(b)) with respective color indicating where the fluorophores are located; spacer layer thickness is 25 nm; (g),(h) field intensity 8nm above the surface (dashed lines in (c),(d)) with respective color indicating where the fluorophores are located; spacer layer thickness is 80 nm.

In figure 3.36, we present a summary plot of the calculated field intensity by FDTD for comparison to the measurements of fluorescence maxima in figure 3.34. The field intensity is shown for heights 8nm above the surface with nanowires for two different polarizations as a function of spacer layer thickness, ranging from 0nm to

650nm. The field intensity reproduces the two crossings we observe, but in addition shows additional crossings, and no obvious damping of the enhancement with increasing spacer layer thickness. As the spacer layer thickness increases, the high field along transverse polarization appears periodically between the silver nanowire and the ground plane, resulting in the peaks, at oxide layer thicknesses of: 48, 248, 352 nm. In contrast, the peaks along longitudinal polarization are due to the intermediate region being pushed up into high field periodically as the spacer layer thickness increases.

Clearly the local field intensity and its variation with spacer thickness explain only a part of the complicated switching behavior we observe in the dominant polarization.

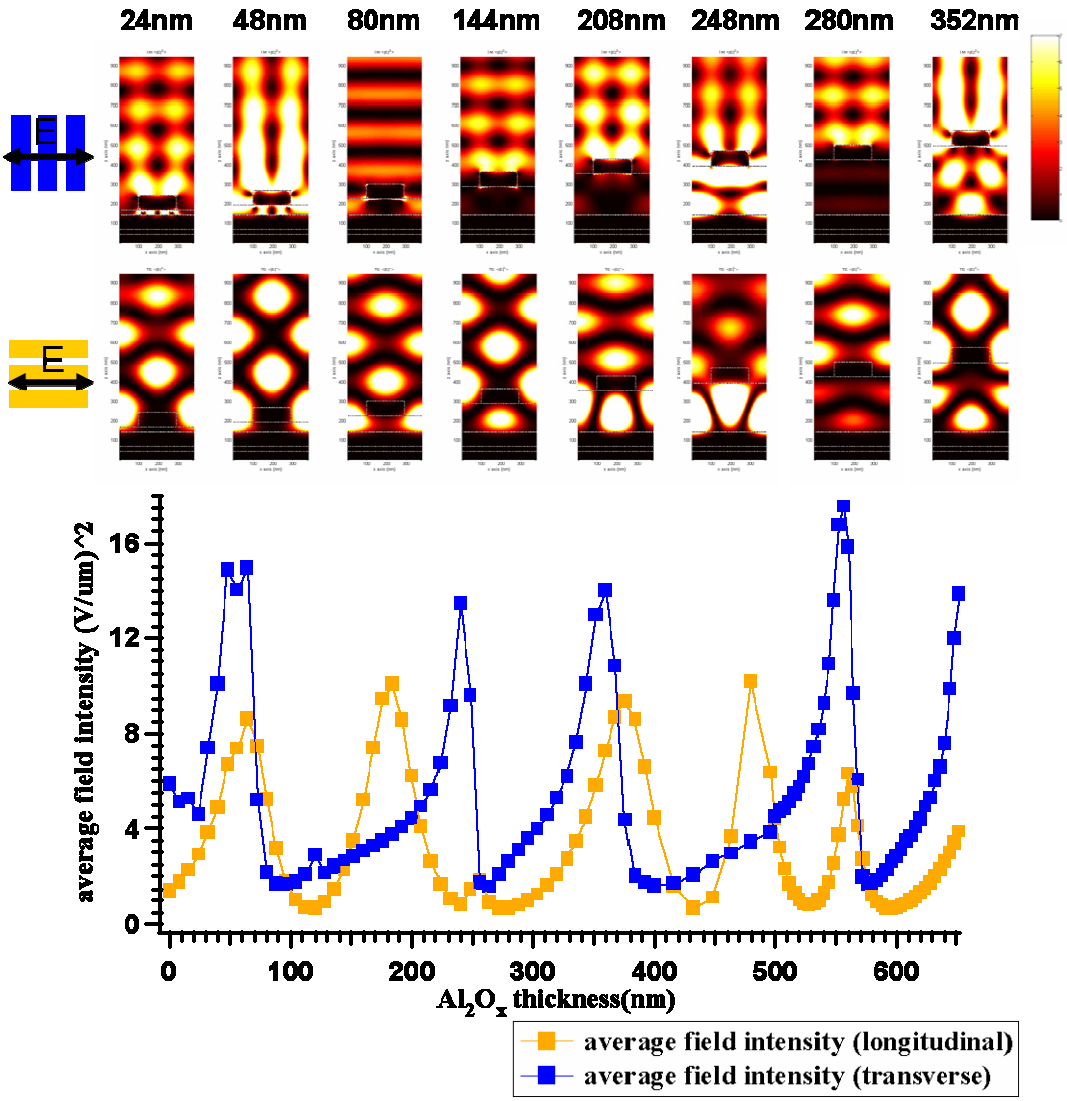

Figure 3.36: Field calculations by using FDTD method: Field intensity maps (top) at different oxide layer thicknesses as labeled along longitudinal (orange) and transverse (blue) polarizations. A summary plot (bottom) shows the average field intensity 8nm above the surface where the fluorophores locate as a function of oxide layer thickness ranging from 0 nm to 650 nm along two polarizations.

Chapter 4: Conclusions

The unique contribution of this work is to employ electron beam lithography in the systematic study of fluorescence enhancement from noble metallic nanostructures. Fluorescence enhancement from silver nanoparticles is highly size- and shape-dependent. The wavelength dependence of the observed optimum size is qualitatively consistent with a red-shift in the transverse Plasmon-polariton oscillation modes for oblate spheroid particles of decreasing height/width ratio, although our shapes are more complex, resulting in additional modes.

Our results also show that the effect of decreasing the spacing is to decrease the normalized enhancement ratio, which is consistent with a shift in the plasmon-polariton frequency away from that of the fluorescence at relatively small particle spacings, i.e. less than 1.5 times the lateral size of the nanoparticles. Indeed such an effect has been reported in optical absorption measurements from silver dot arrays at comparable spacings by Gotschy et al. [66] On the contrary, for center-to-center spacings of more than ~2-3 times the lateral size of the nanoparticles, the optimum size for fluorescence no longer depends on spacing, thus indicating weak interparticle coupling beyond this. However, by comparing the optimum height/width ratio of the spheroid nanoparticles with the polarization dependence of the incident light, particle Plasmon resonance can no longer fully explain the mechanism in the fluorescence enhancement.

Calculations, both for isolated nanoparticles and for periodic nanowires, demonstrate that active substrates, i.e. those with large dielectric functions, have a strong effect on the size- or period-dependence of fluorescence enhancement in the

presence of a substrate, and the region of high field shift position as the particle size varies, thus maximum fluorescence enhancement occurs when a large fraction of those fluorophores which are not shadowed by either the particles or substrate are immersed in region of high field; low or no enhancement otherwise.

We generally find that the maximum fluorescence enhancement from compact periodic nanoparticles is much higher than that from periodic nanowires; nonetheless it is interesting to consider the polarization dependence of fluorescence enhancement in attempting to understand the contribution of local fields. The local field intensity distribution changes across nanowires structures as we vary the polarization of incident light, and that gives rise to an optimum polarization direction. We find that the enhancement can be greatly magnified in the presence of an underlying Ag film. Most intriguingly, we find an switching behavior of the optimum polarization as we increase the spacer layer between the nanowires and the ground plane, which appears only partly explained by variation in the local field intensity.

Since both absorption and reemission of fluorescence are wide spectrums, the possible future work is to replace band pass filter and detector with spectrometer to collect spectral response of fluorescence. We can even replace the excitation by lamp with finite and compatible spectrum for absorption in fluorescence.

We expect this new insights provided by this work to lead to advances in the development of highly sensitive biochips. We further note that the work presented here represents only a limited optimization, and anticipate larger enhancements via a systematic variation of the multiple parameters we find are important in noble metal nanoparticle enhanced fluorescence.

Appendix A - **Finite-Difference Time-Domain (FDTD)**

In 1966 Yee [24] proposed a technique to solve Maxwell's curl equations using the finite-difference time-domain method [67]. It has been used to solve numerous scattering problems on microwave circuits, dielectrics and electromagnetic wave interaction with a number of materials at different frequencies [68-70].

Maxwell's equations for an isotropic medium are:

$$\nabla \times \vec{E} + \frac{\partial \vec{B}}{\partial t} = 0 \tag{A1a}$$

$$-\nabla \times \vec{H} + \frac{\partial \vec{D}}{\partial t} = \vec{J} \tag{A1b}$$

$$\vec{B} = \mu \vec{H} \tag{A1c}$$

$$\vec{D} = \varepsilon \vec{E} \tag{A1d}$$

Where $\vec{J}, \mu, \varepsilon$ are assume to be given functions of space and time. In a Cartesian coordinate system, (A1a), (A1b) are equivalent to the following:

$$\frac{\partial H_x}{\partial t} = \frac{1}{\mu}\left(\frac{\partial E_y}{\partial z} - \frac{\partial E_z}{\partial y}\right) \tag{A2a}$$

$$\frac{\partial H_y}{\partial t} = \frac{1}{\mu}\left(\frac{\partial E_z}{\partial x} - \frac{\partial E_x}{\partial z}\right) \tag{A2b}$$

$$\frac{\partial H_z}{\partial t} = \frac{1}{\mu}\left(\frac{\partial E_x}{\partial y} - \frac{\partial E_y}{\partial x}\right) \tag{A2c}$$

$$\frac{\partial E_x}{\partial t} = \frac{1}{\varepsilon}\left(\frac{\partial H_z}{\partial y} - \frac{\partial E_y}{\partial z} - \sigma E_x\right) \tag{A2d}$$

$$\frac{\partial E_y}{\partial t} = \frac{1}{\varepsilon}\left(\frac{\partial H_x}{\partial z} - \frac{\partial E_z}{\partial x} - \sigma E_y\right) \tag{A2e}$$

$$\frac{\partial E_z}{\partial t} = \frac{1}{\varepsilon}\left(\frac{\partial H_y}{\partial x} - \frac{\partial E_x}{\partial y} - \sigma E_z\right) \qquad \text{(A2f)}$$

Yee defines the grid coordinates (i,j,k) as

$$(i, j, k) = (i\Delta x, j\Delta y, k\Delta z) \qquad \text{(A3a)}$$

where $\Delta x, \Delta y, \Delta z$ are the actual grid separations. Any function of space and time is written as

$$F^n(i, j, k) = F(i\Delta x, j\Delta y, k\Delta z, n\Delta t) \qquad \text{(A3b)}$$

where Δt is the time increment, n is the time index and $\delta = \Delta x = \Delta y = \Delta z$. The spatial and temporal derivatives of written using central finite difference approximations as

$$\frac{\partial F^n(i, j, k)}{\partial x} = \frac{F^n(i + \frac{1}{2}, j, k) - F^n(i - \frac{1}{2}, j, k)}{\delta} + O(\delta^2) \qquad \text{(A4a)}$$

$$\frac{\partial F^n(i, j, k)}{\partial t} = \frac{F^{n+\frac{1}{2}}(i, j, k) - F^{n-\frac{1}{2}}(i, j, k)}{\delta t} + O(\delta t^2) \qquad \text{(A4b)}$$

Equations (A4a), (A4b) are applied to the six scalar equations (A2a) ~ (A2f) resulting in six coupled explicit finite difference equations, and then the electric field and the magnetic field are solved alternatively in time. In all of the finite difference equations the components of $\vec{E}, \vec{H}$ are located within a single unit cell in the three-dimentional lattice depicted in Figure A.1.

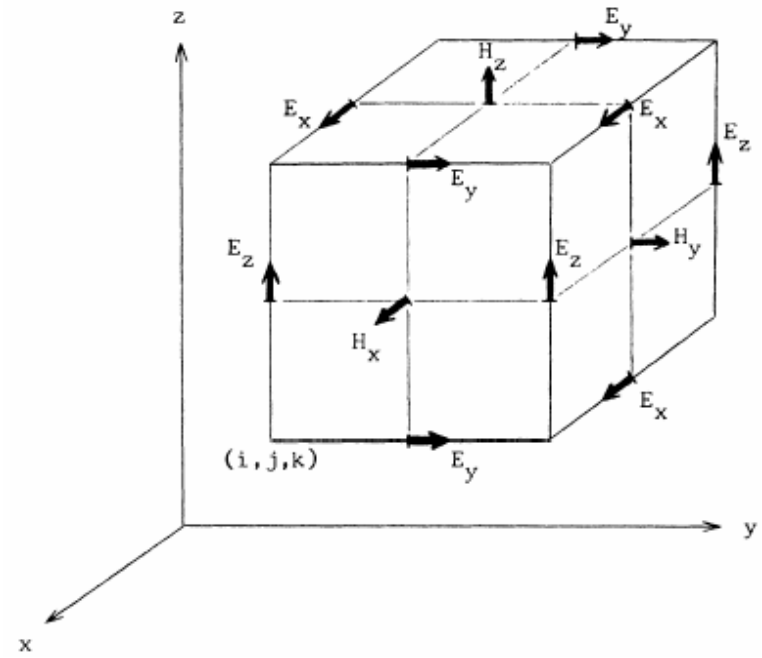

Figure A.1: Yee cell demonstrates the arrangement of field components within a cubical grid.

To yield accurate results, the grid spacing δ in the finite difference simulation must be much less than the wavelength, usually less than $\frac{\lambda}{10}$. The stability condition relating the spatial and temporal step size is [71]

$$v_{\max}\Delta t = [\frac{1}{\Delta x^2} + \frac{1}{\Delta y^2} + \frac{1}{\Delta z^2}]^{-\frac{1}{2}} \qquad \text{(A5a)}$$

where $v_{\max}$ is the maximum velocity of the wave. When the step size δ is the same in all directions, the stability condition is

$$\frac{v_{\max}\Delta t}{\delta} = \frac{1}{\sqrt{N}} \qquad \text{(A5b)}$$

where N is the number of spatial dimensions in the problem.

Appendix B - **Discrete Dipole Approximation (DDA)**

The whole system, including nanoparticles and a substrate are modeled by collection of N dipoles with dipole moment $\vec{p}$. We calculate the response of these dipoles to fields associated with the incident light and those induced by the other dipoles [23]. For a dipole at site *i*, the dipole moment is $\vec{p}_i$ with amplitude α proportional to the electric field on the *i* site (eq. (B1) and (B2))

$$p_i = \alpha \; E_i \tag{B1}$$

$$E_i = E_0 \hat{y} \exp(ikx_i) + \sum_{j \neq i} \frac{\exp(ikr_{ij})}{r_{ij}^{\;3}} \times [k^2 (r_{ij} \times p_j) \times r_{ij} + \frac{(1 - ikr_{ij})}{r_{ij}^{\;2}} (3p_j \cdot r_{ij} r_{ij} - r_{ij}^{\;2} p_j)] \tag{B2}$$

$$p_i^{(l+1)} = \eta \alpha E_i^{(l+1)} + (1 - \eta) p_i^{(l)} \tag{B3}$$

Here E_i is the electric field on the *i* site resulting from the incident light and induced field from other dipoles. By an iterative method with initial condition $p_i^{(0)} = 0, \;\; E_i^{(1)} = E_0 \hat{y} \exp(-ikx_i)$, we can calculate the dipole moments, using

$$E_i^{(l+1)} = E_0 1_z \exp(ikx_i) + \sum_{j \neq i} \frac{\exp(ikr_{ij})}{r_{ij}^{\;3}} \times [k^2 (r_{ij} \times p_j^{\;l}) \times r_{ij} + \frac{(1 - ikr_{ij})}{r_{ij}^{\;2}} (3p_j^{\;l} \cdot r_{ij} r_{ij} - r_{ij}^{\;2} p_j^{\;l})] \tag{B4}$$

where η is introduced for improving convergence, set 0.5. Then we extract the dipole moments for each site to calculate the spatial variation of electric field. [72]

Appendix C – **Metrology of spherical nanoparticles**

The statistics of the size and the number density of the particles were obtained by analyzing SEM images scanned from the sample with image processing software developed in Java [36]. Originating from the ImageJ module (NIH), it defined particle regions on images by convolution with a series of image processing matrixes, and analyzes particle spacing based on Voronoi's theorem [40]. This yielded statistics of particle distribution; more details are described below.

We have created an algorithm to extract statistics on particle average height, area, volume, center-to-center distance, and peak-to-peak distance based upon real AFM and SEM images [36]. We have used this analysis to correlate metal enhanced fluorescence with these geometrical parameters in a meaningful way, and to derive conditions for which the MEF is optimized. In the pre-processing step, the source image passes through a series of convolutions with different image processing matrixes and results in several intermediate images prepared for particle definition. In addition, it also allows users to subtract background for AFM images to accommodate piezo effect in tip scanning. In the particle definition step, we find the correlation in between those intermediate images from previous process, followed by morphological pruning and erosion plus dilation to eliminate sharp noises and close up the particle edges. After we determine the particle edges, we label every particle region and define territories by implementing the Vorinoi theorem [40, 77]. Finally, the program extracts particle statistic information and exports data after merging or deleting those non-particle territories selected by user.

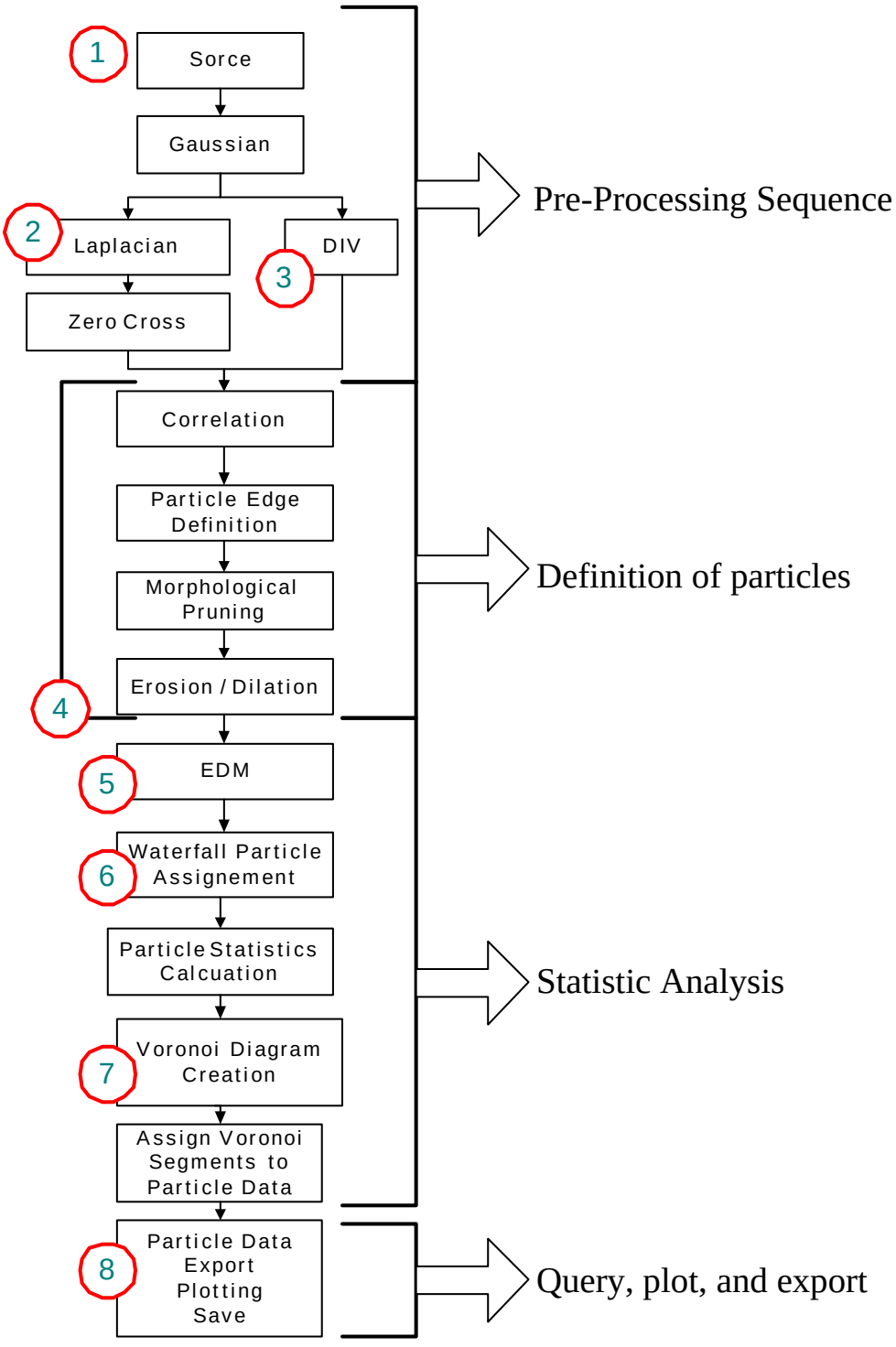

Figure C.1: Algorithm flow chart for Java software.

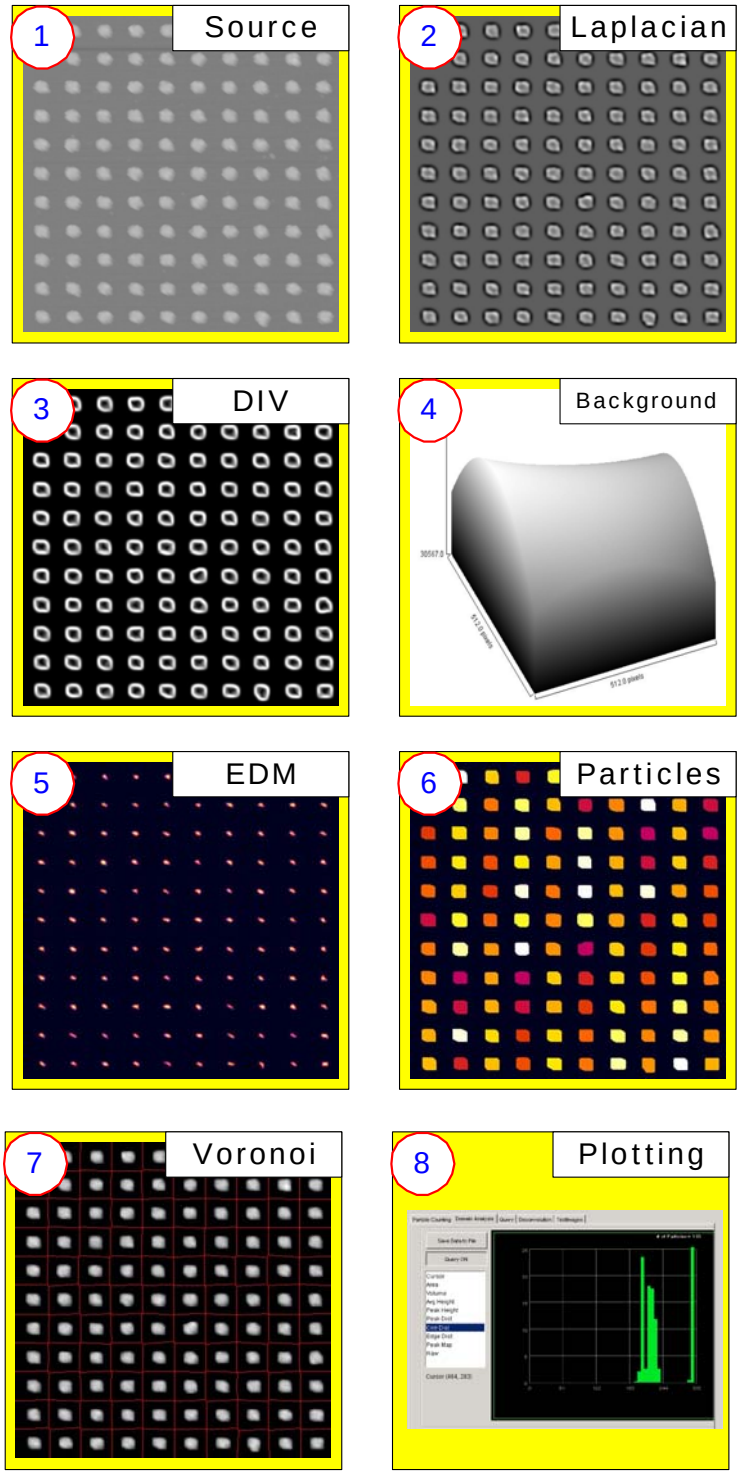

Figure C.2: Intermediate images or plots for steps labeled in Fig. C.1.

Appendix D - **Photobleaching in fluorophores CY3 and CY5**

Photobleaching is the photochemical destruction of a fluorescent molecule. It involves two processes, absorption and reemission. The total number of photons one fluorescent molecule can emit is proportional to the number of cycles of absorption-emission it has completed, and each cycle has an equal probability of causing photobleaching [41]. Loss of activity caused by photobleaching can be controlled by reducing the intensity or time-span of light exposure, by increasing the concentration of fluorophores, or by employing more robust fluorophores that are less prone to bleaching. To a reasonable approximation, any given molecule will be destroyed after a long-term exposure. We have conducted experiments to explore the photobleaching effect on CY5 and CY3. Since we have kept the concentration of fluorophores and laser beam power the same, the only variable is exposure time. After scanning a series of CY5 fluorescence images on a groove pattern described in section 3.6, the fluorescence ratios depending on various groove widths along two different polarizations remain similar for the first several scan frames (Fig D.1). On the other hand, the CY3 fluorescence dependence on polarization lasts much longer than for CY5 in the same scan time. (Examples are shown in figure D.2 for large square patterns.)

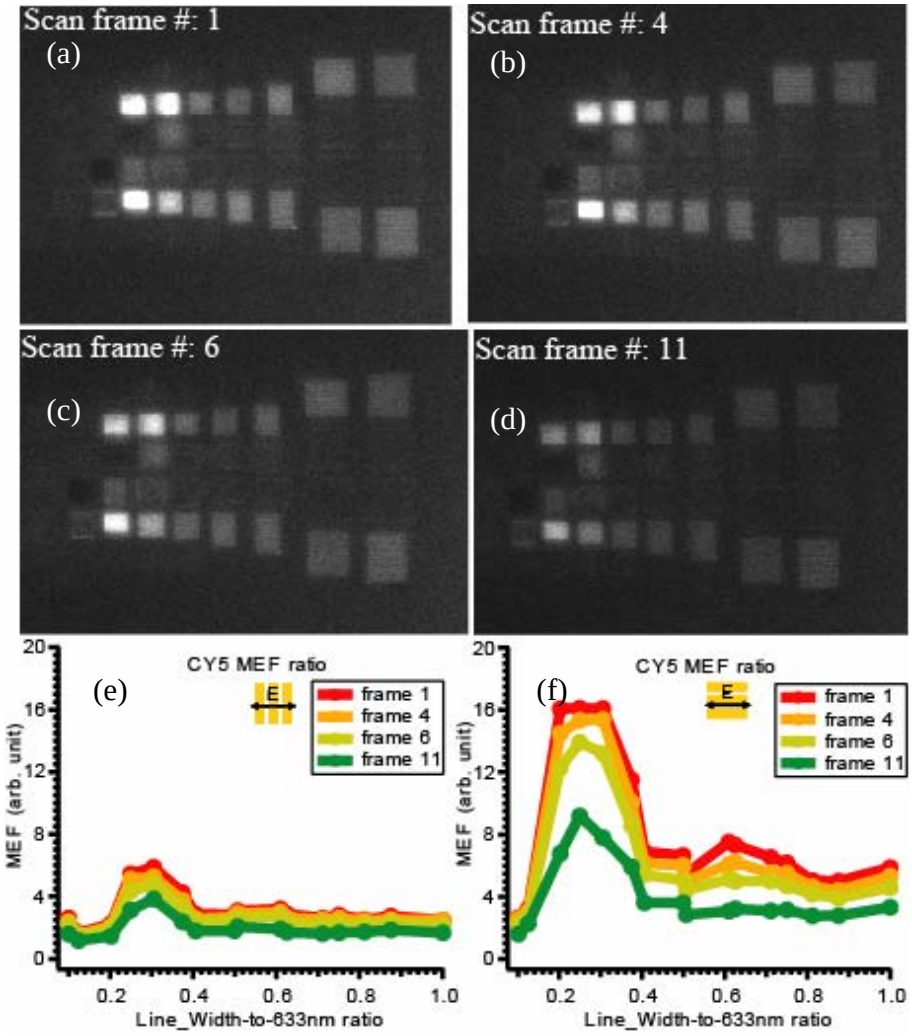

Figure D.1: A series of CY5 fluorescence images labeled with scan number ((a) ~ (d)), and fluorescence ratio as function of line width to 633nm ratio along two different polarization. ((e): transverse polarization, (f): longitudinal polarization)

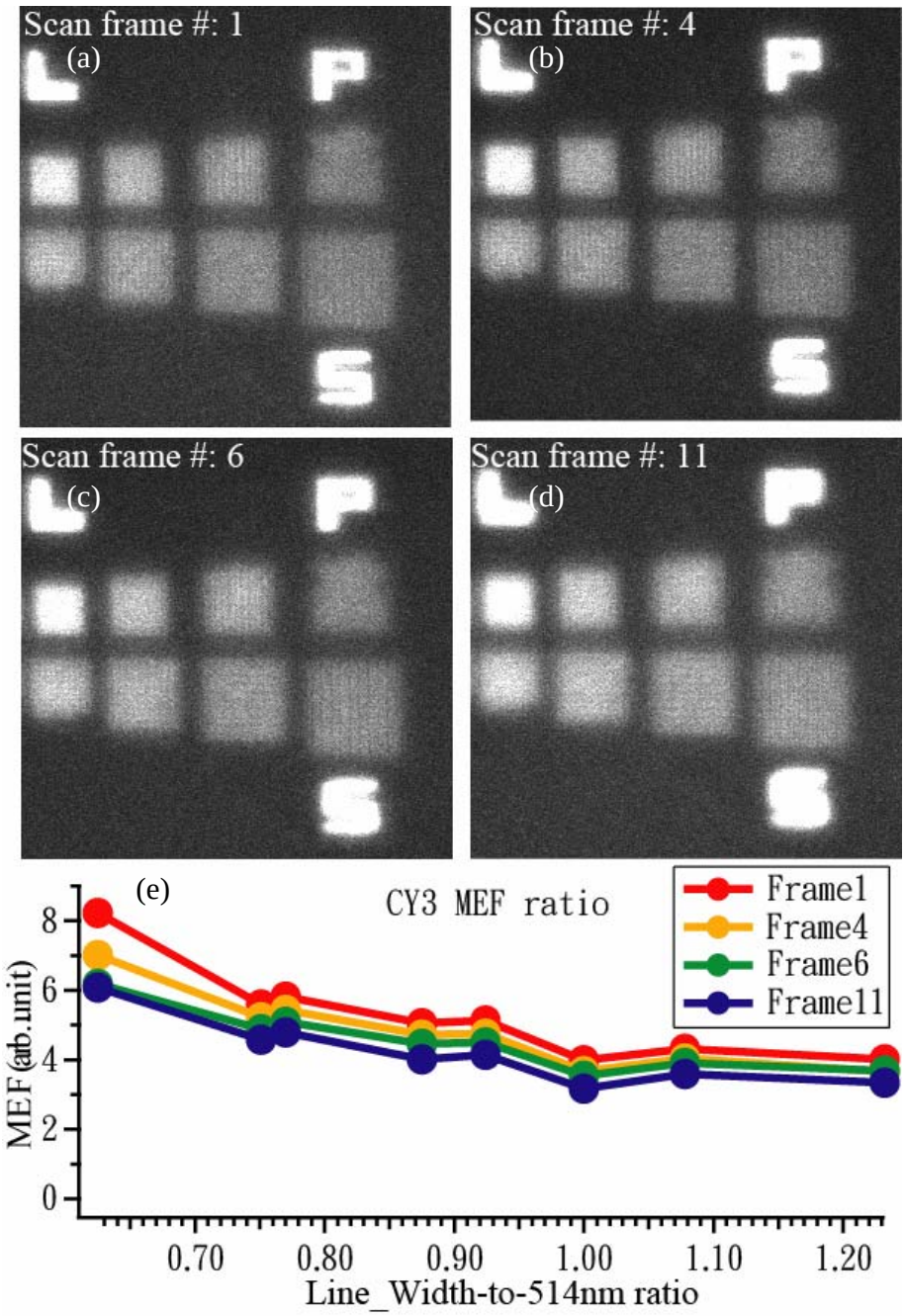

Figure D.2: A series of CY3 fluorescence images labeled with scan number ((a) ~ (d)), and fluorescence ratio as function of square width to 514nm ratio (e).

Appendix E - Attenuation in fluorescence measurement

As described in section 2.4, an intensity ratio allows us to correlate the fluorescence intensities from different samples by taking optical densities into account. We demonstrate how the results would look in the saturation region. Shown in Fig. E.1, are three CY5 fluorescence images under different attenuation filters, index 3, 10, and 30. Quantitative analyses of enhancement ratio for various line periods along two different groove orientations are plotted as well. It is easy to pick out that the enhancement ratio curves would be truncated for working in the saturation region, at attenuation indexes of 3 and 10. The case of attenuation index 30 gives the most detailed information among all three. Therefore, we should pick the fluorescence image with attenuation index 30 as the source for our fluorescence measurements.

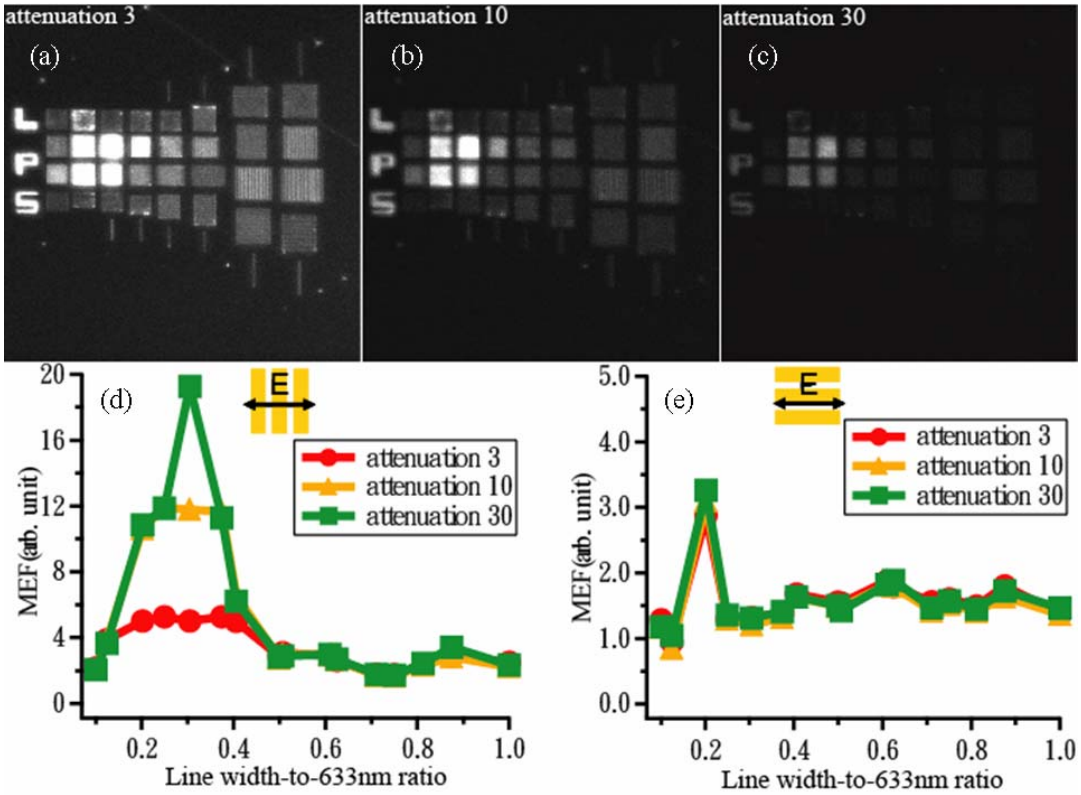

Figure E.1: CY5 fluorescence images with different attenuation filter as labeled ((a) ~ (c)), and plots for fluorescence enhancement as function of the ratio of line width to 633nm at: (d) transverse polarization, and (e) longitudinal polarization.

Appendix F - Fluorescence lifetime measurement

The strong interaction of excited fluorophores with metallic nanoparticles causes enhanced intensity and decreased fluorescence lifetime as reported by theoretical and experimental data [28, 50, 73]. Measurements described in this section conclude that the enhanced fluorescence intensities are actually due to the interaction of the excited local field with the fluorophore rather than local fluorophore distribution [74 -76]. Here we use another fluorescence tag, fluorescein, which exhibits sharper absorption and reemission spectrums with peaks both higher than those for CY3 (Fig. F.1). Fluorescein conjugated to biotin was immobilized using an additional layer of avidin that, as a tetrameric protein, would act as a link between the surface-bound and dye-bound biotins. The distance between fluorescein and the Ag surface is estimated in this case to be about 9 nm (combined thickness of BSA and Avidin).

Lifetime data were obtained for Fluorescein-biotin system by acquiring a set of phase-sensitive fluorescence images at a modulation frequency of 40 MHz. This was accomplished using Fluorescence Lifetime Imaging Microscope [75, 76], where sinusoidal modulated amplitude of a light emitting diode (LED) was used [74]. From the difference of phase angle between fluorescence and excitation signal a phase lifetime was calculated for each array as $\tau = \frac{1}{2\pi f}\arctan\varphi$, where f is the modulation frequency, and φ the measured phase shift. The average phase lifetime was calculated for each array. Figure F.2 shows the fluorescence enhancement and corresponding decrease in lifetime. The strong relationship between intensity enhancement and

decrease in lifetime can be used as direct confirmation of effects of interaction of excited fluorophore with plasmon resonant nanoparticles. Large decrease of fluorescence lifetime is observed only for near-field effects, at distances where the excited molecule dipole interacts most strongly with the nanoparticle [28, 73].

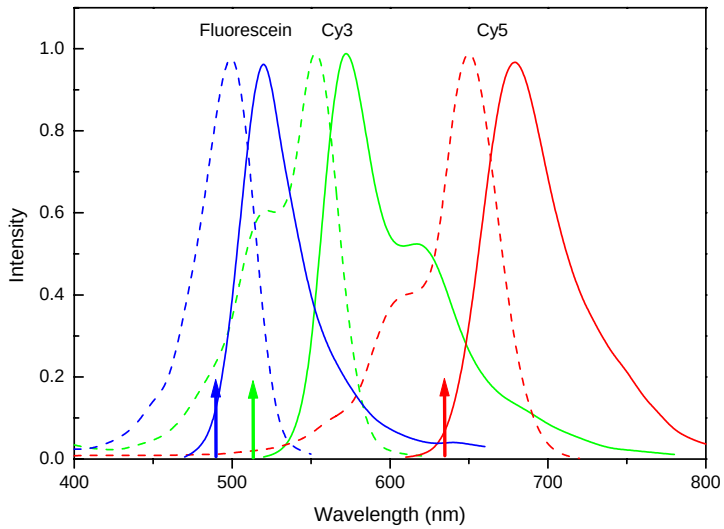

Figure F.1: Absorption and emission spectra of Fluorescein, Cy 3 and Cy 5. Laser lines used for excitation are shown with arrows: 488 nm, 514 nm and 633 nm.

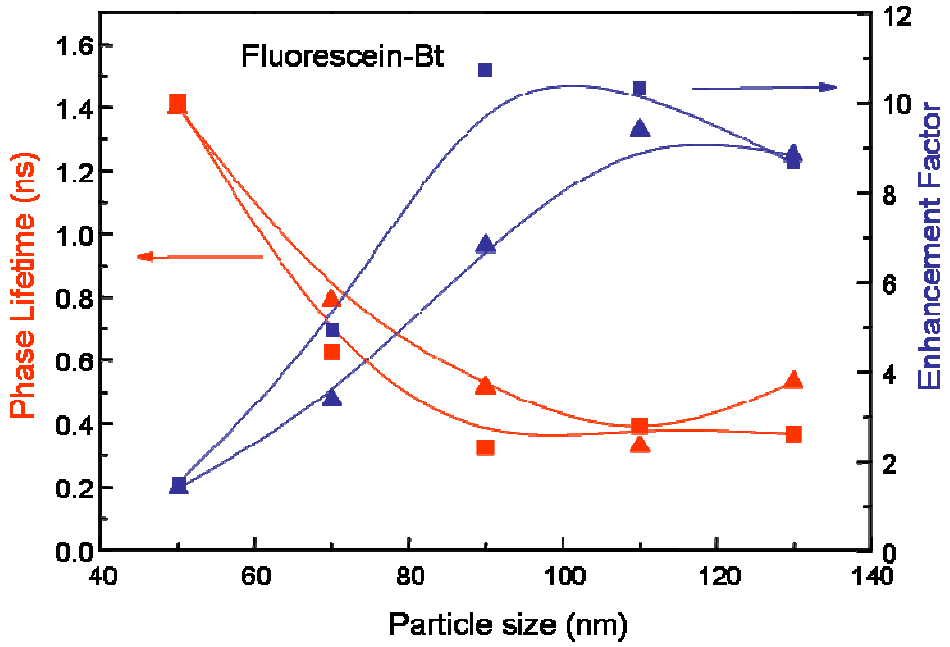

***Figure F.2:** Decrease in fluorescence lifetime (red) with simultaneous fluorescence enhancement (blue) is a unique fingerprint of interaction of excited molecules with particle plasmon resonance. Data are for Fluorescein-biotin on a Ag array with square and triangle shapes of particles and spacing of 210 nm. Excitation of 470 nm (Blue LED) and modulation frequency of 40 MHz were used.*

Appendix G - Enhancement dependence on particle height

Other than controlling the shape and the size of the nanoparticles, we also conduct experiments to explore the dependence on the particle height as well. As described in section 3.4, the optimum square nanoparticle is 90 nm for CY3, so we decided to fabricate array of square nanoparticles with fixed lateral size 90 nm and center-center spacing 210 nm on an aluminum oxide covered Si substrate, and vary the particle height with the upper limit set by the thickness of the PMMA resist. As shown in Fig. G.1, the optimum enhancement for CY3 occurs at ~ 75 nm particle height.

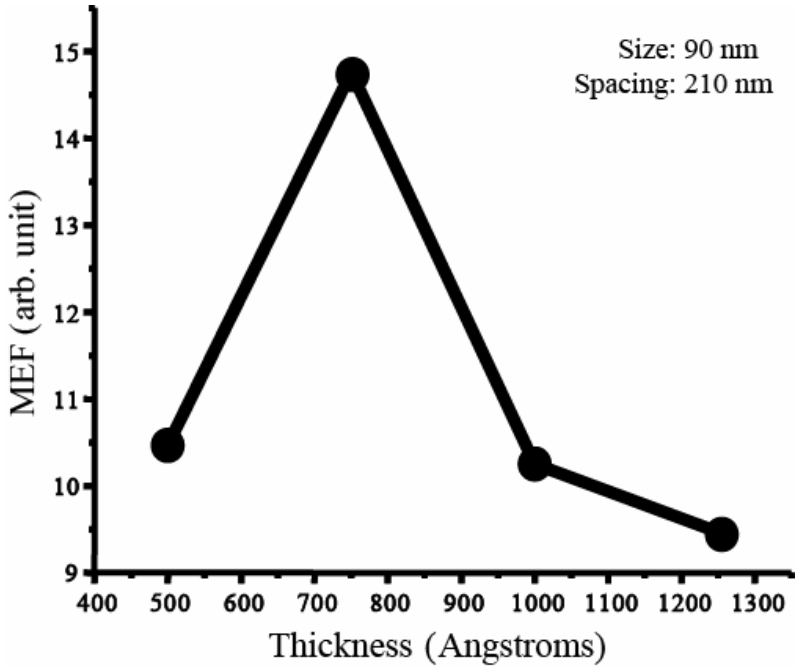

Figure G.1: Fluorescence enhancement dependence on square particle height with controlled particle size 90 nm and center-center spacing 210 nm.

Appendix H - **Transmission on Al_2O_x covered glass**

To investigate the role of the oxide layer in fluorescence enhancement, we have done transmission measurements on the glass slides covered with different thicknesses of oxide, and as summarized in figure H.1(b), the transmission does not drop significantly as the thickness of oxide layer increases. Thus the effective intensity for ground plane coupling may still be effective as we increase the thickness of the oxide layer, and which can not explain the decreasing phenomenon for the enhancement from nanostructures spaced by thick oxide layer above the ground plane.

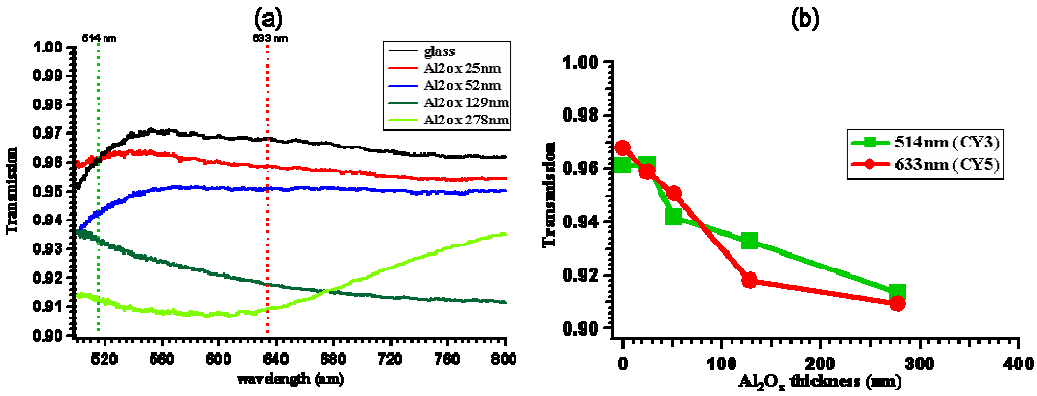

Figure H.1: Summary plots show the transmission spectrum (a) and the transmission at two incident wavelengths for CY3 and CY5 (b), from glasses covered with various thickness of oxide.

Appendix I – **Height-height correlation function**

The surface roughness can not only be characterized by the RMS roughness, but also the correlation length, which can be estimated by height-height correlation function as shown below:

$$G(x) = W[1 - e^{-(\frac{x}{\xi})^{2\alpha}}] \qquad \text{(I1)}$$

ξ is the correlation length and can be calculated by fitting the equation above on the 2-dimentional auto-correlation map of the original AFM image.

Appendix J – **Enhancement from nominally flat metallic and non-metallic films**

Due to the difference in dispersion relationships between light and surface plasmons, a flat metallic film should not enhance fluorescence. However, as pointed out by Moskovits [43] roughness on a metal surface can lead to coupling of light to plasmons. In this section we discuss observations of fluorescence on nominally flat, but in reality rough surfaces, [19] including observations of fluorescent intensity from fluorophores spaced above both metallic and non-metallic substrates. All samples were masked off so that regions of contiguous films of silver 75 nm thick were bordered by regions with no such films; aluminum oxide films of various thicknesses were deposited onto the entire samples using a commercial electron-beam evaporator (CHA Mark-40). We then used AFM to characterize surface roughness and correlation length based on analysis of the height-height correlation function (detailed in Appendix I). Over the range of oxide layer thickness we have explored (Fig. J.1), the surface roughness on 75 nm silver covered Si (001) substrate increases initially up to peak value around 3.2 nm, and decreases after oxide layer thickness exceed 60 nm. The correlation length has a similar behavior on this type of surface, and shows a peak at approximately 80 nm oxide layer thickness with maximum correlation length around 60 nm. On the other Si (001) surface, the surface roughness and correlation length monotonically increase over the same range of oxide layer thickness, and merge with those from silver covered surface at surface roughness ~ 1.4 nm and correlation length ~ 25 nm.

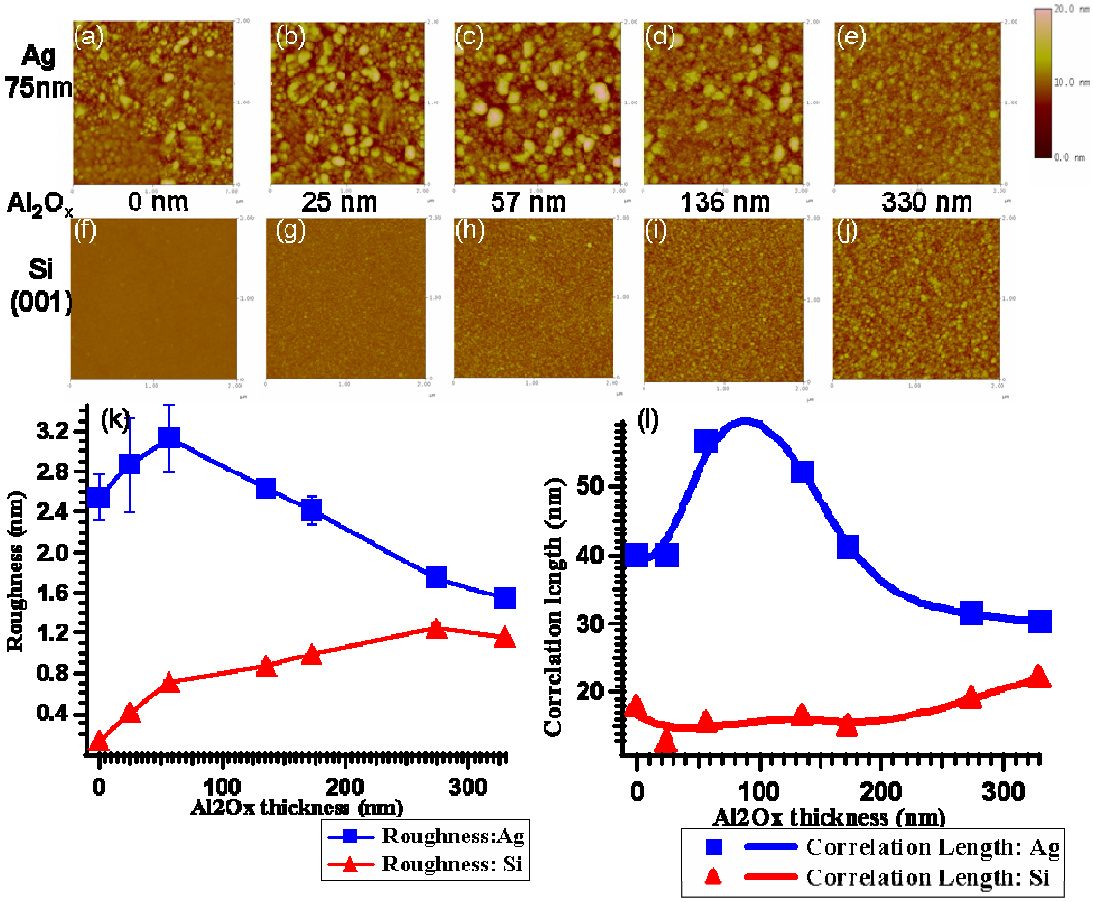

Figure J.1: AFM images (field of view: 2 um) with different oxide (Al_2O_x) layer thickness as labeled on silver-covered (75 nm) Si (001) surface (a) ~ (e) and Si (001) surface (f) ~ (j). Summary plots for roughness (k) and calculated correlation length (l) on these two different surfaces with oxide (Al_2O_x) layer thickness ranging from 0 nm to 330 nm.

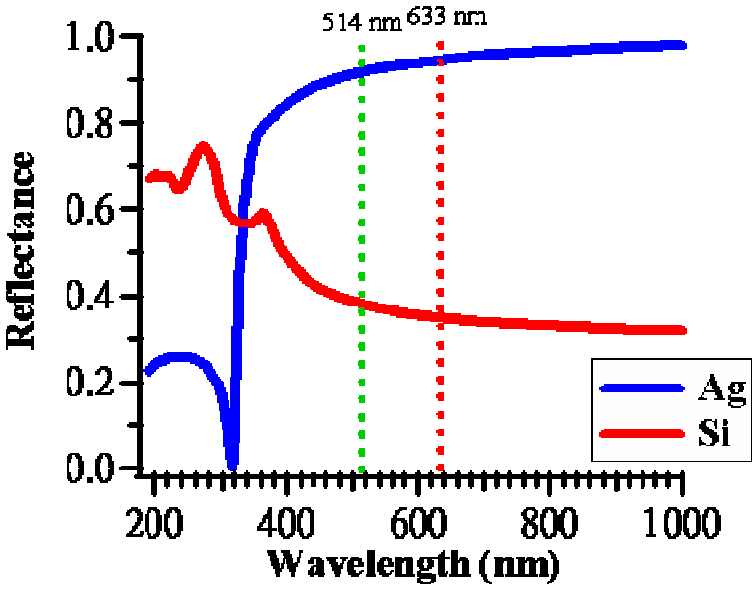

Reflectance	514nm	633nm
Ag	0.916	0.944
Si	0.381	0.348

Figure J.2: Reflectance from silver covered and non-covered Si (001) surfaces are measured by reflectometer (N&K analyzer 1500) over the range of wavelength from 200 nm to 1 um.

We also measure fluorescence for two different fluorophores simultaneously, CY3 (green) and CY5 (red). The reflectance and fluorescence images are shown in figure J.3 and J.4 respectively for CY3 and CY5. By capturing images at the boundary between silver covered and non-covered substrates, we can compare the intensities from the two different surfaces either on reflectance of incident wavelength or on fluorescence of CY3/CY5. The reflectance (as measured independently by a commercial reflectometer, N&K analyzer 1500) from silver-covered surfaces is higher than that from Si surface at incident wavelengths of both 514 and 633 nm, the reflectance intensities from silver-covered portions are always brighter than non-silvered portion (Fig. J.2). If high reflectance serves as the main

source of high fluorescence, we should observe the fluorescence intensities from silver-covered portions to be consistently brighter than non-silvered portions. However, there are several exceptions in the range of oxide layer thicknesses we explored, e.g. oxide layer thicknesses 120 nm, 135 nm for CY3 (Fig. J.3) and 135 nm, 170 nm for CY5 (Fig. J.4). On those fluorescence images, the intensities from the half only covered by oxide are actually brighter than those from the other half covered by silver and oxide.

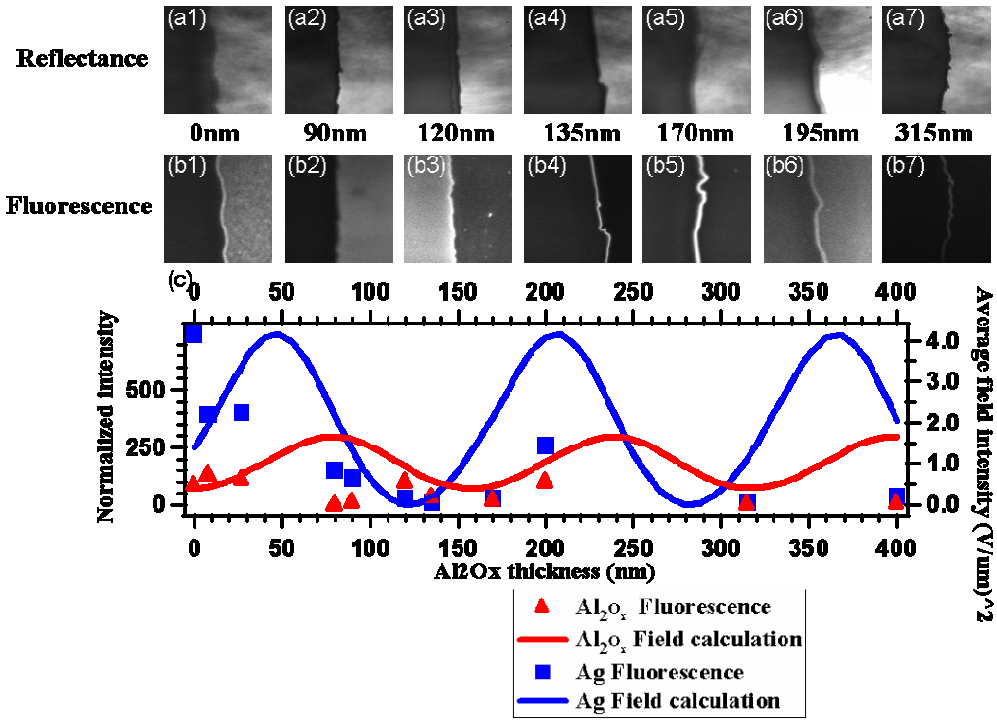

Figure J.3: Reflectance (a1) ~ (a7) and CY3 fluorescence (b1) ~ (b7) images (field of view ~ 110 um) at the edge between silver covered (right part of each image) and non-covered (left part of each image) part of the Si (001) substrate, and the summary plot (c) of normalized intensity (points) and calculated (FDTD) average

field intensity 8 nm above the surface (lines) on silver covered substrate (blue) and non-covered Si substrate (red) as a function of oxide (Al_2O_x) layer thickness ranging from 0 nm to 400 nm.

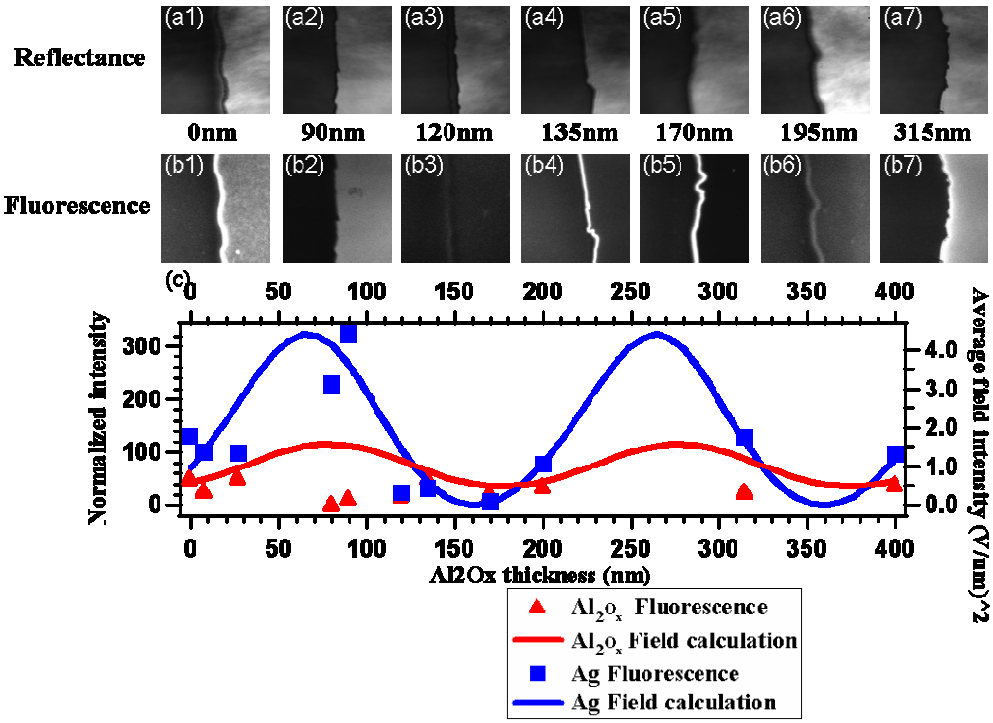

Figure J.4: Reflectance (a1) ~ (a7) and CY5 fluorescence (b1) ~ (b7) images (field of view ~ 110 um) at the edge between silver covered (right part of each image) and non-covered (left part of each image) part of the Si (001) substrate, and the summary plot (c) of normalized intensity (points) and calculated (FDTD) average field intensity 8 nm above the surface (lines) on silver covered substrate (blue) and non-covered Si substrate (red) as a function of oxide (Al_2O_x) layer thickness ranging from 0 nm to 400 nm.

We calculate the field intensity distributions by 2-dimentional FDTD methods (appendix A) for various Al_2O_x layer thicknesses deposited on both silver-covered and non-covered Si substrate (Fig. J.5), and summarize the average field intensities (Fig. J.3(c)) 8 nm above the surface as pointed out by the purple dash lines where the fluorophores locate. Since we are working on the substrate only, the plane source wave propagates from the top and bounces back until it reaches steady state. The field intensity map at the steady state would still be a plane wave but with half of the wavelength of the field. Therefore, the incident wavelength (514 nm in vacuum) of CY3 is 320 nm in Al_2O_x, and we have a peak-to-peak distance in the calculation equal to 160 nm (Fig. J.3(c)). On the other hand, the incident wavelength (633 nm in vacuum) of CY5 is 400 nm in Al_2O_x, and the peak-to-peak distance in calculation equal to 200 nm (Fig. J.4(c)). The maximum field intensity with oxide on the silver plane is higher than that with oxide on Si substrate. The optimum field intensities 8 nm above would oscillate in between the two surfaces due to the phase difference, and that explains the switching phenomenon of which side shows higher intensity in the fluorescence images. The normalized intensities are the intensities normalized by the attenuation ratio (Section 2.4), and the peak shifts from 0 nm on silver surface for CY3 to 90 nm for CY5. Furthermore, the fluorescence intensities for both fluorophores decay as the oxide layer thickness increases. More calculations are needed in order to have a complete explanation of this phenomenon.

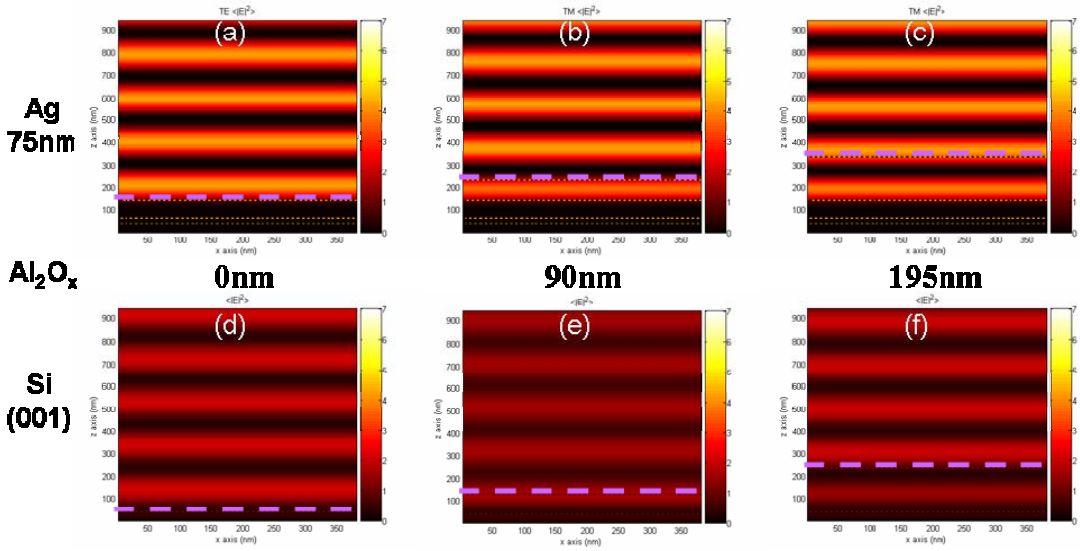

Figure J.5: Field intensity distributions calculated for various aluminum oxide layer thicknesses as labeled on silver-covered (a) - (c) or non-covered (d) - (f) Si substrate with incident wavelength 514 nm (for CY3). The average field intensities in the summary plot (Fig. J.3(c)) are 8nm above the surface as pointed out by the purple dash lines where the fluorophores are located.

Appendix K – **Calculated dipole moment contribution**

Clearly the local field intensity and its variation with spacer thickness explain only a part of the complicated switching behavior we observe in the dominant polarization (section 3.10). We must also consider possible mechanisms of damping in fluorescence enhancement as the spacer layer thickness increases, which we will now discuss.

Based on Mie theory [1], electric fields generated by very small particles are purely dipolar, but the fields may gain additional higher-order components (quadupole, octapole, etc.) as the particle size increases. It's generally believed that only the dipole moment can radiate its field outward, and others do not significantly to radiation from the particle. We have observed damping of fluorescence enhancement as a function of oxide layer thickness which is not predicted by the FDTD calculations. Here, we calculate the dipole moment as a function of spacer layer thickness in order to test the simple idea that it is the dipole moment contribution to the overall field is important to fluorescence enhancement. As we learn from classical electrodynamics [82], the electric field can be decomposed into various modes, and the dipole component can be calculated from the charge density distribution relative to the center of mass. We employ Gauss's law to calculate the divergence of electric fields, and divide by the dielectric function to attain the local charge distribution $\rho(\vec{r})$ (fig. K.1(b)),

$$\varepsilon(\nabla \cdot \vec{E}) = \rho(\vec{r}) \tag{3}$$

which is then used to calculate the dipole moment (P) associated with the charges at the position of fluorescence molecules near the nanowire structures, (fig. K.1(c))

$$P = \int \rho(\vec{r})(\vec{r} - \vec{r}_0)dr = P_0 \cos(\omega t + \phi) \quad (4)$$

where $\vec{r}_0$ is defined as center of mass based on the charge distribution.

$$\vec{r}_0 = \frac{\int \rho(\vec{r}) \cdot \vec{r} dr}{\int \rho(\vec{r}) dr} \quad (5)$$

Due to the limitations of 2-dimensional FDTD calculations, we can only calculate the magnitude of the dipole moment, P_0, as a function of spacer layer thickness with transverse excitation polarization (fig. K.1(c)). Unlike the oscillatory behavior of the calculated average field intensity 8 nm above the surface with transverse polarization (fig. 3.36), the dipole moment contribution to the local field along this polarization damps out as we increase the spacer layer thickness. This is qualitatively consistent with what we observe in the experimentally (fig. 3.34).

The damping of fluorescence enhancement is observed as we expand the structure not only vertically, but also laterally. As discussed for periodic nanowires with fixed line width in section 3.6, the enhancement ratio damps out at large period, while the calculated E-field squared oscillates. We carry out similar calculations of dipole contribution to the overall field for this lateral expansion along transverse polarization, and the magnitude of the dipole moment damps out as the period of the nanowires increases (fig K.2). This is qualitatively consistent with the measured fluorescence enhancement ratios which have been corrected with silver coverage area (blue curve in fig. K.2).

This trend provides a strong indication for what the underlying cause of the energy damping is likely to be, and provides additional evidence that the dipolar contribution to the local field is the most important factor in explaining far-field radiation associated with fluorescence.

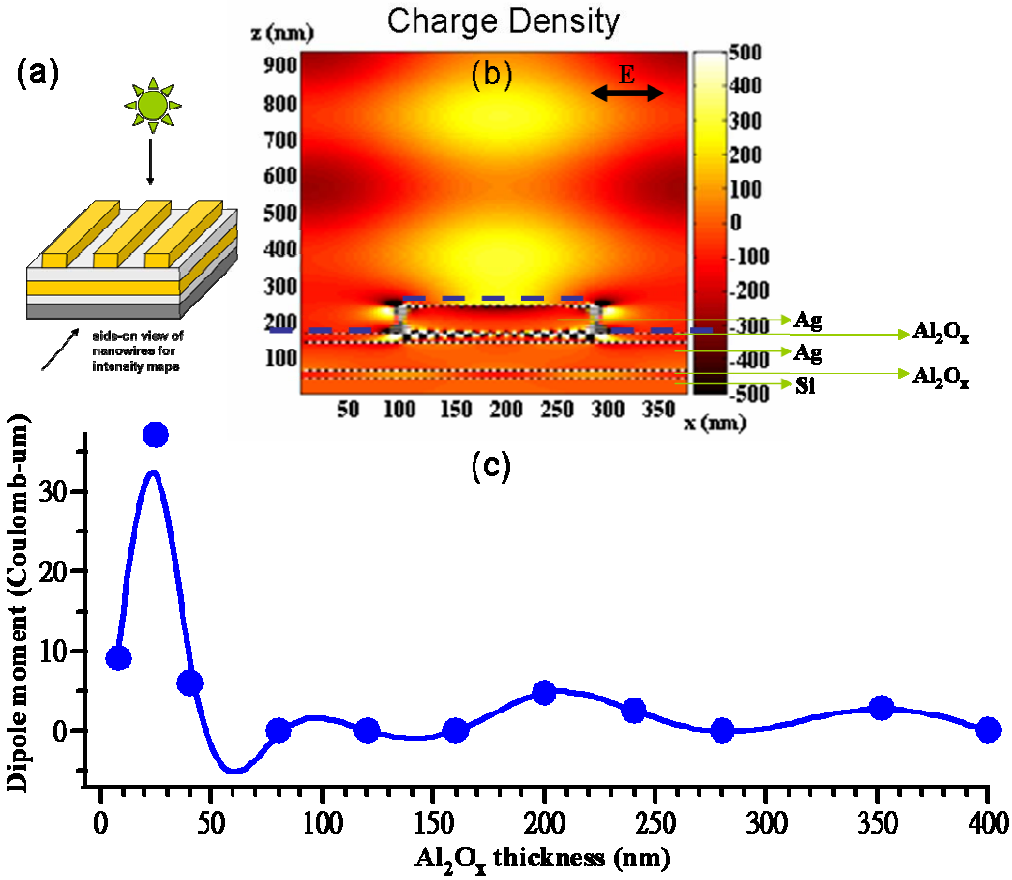

Figure K.1: (a) Schematic of nanowires on the multilayered substrate. (b) Example of charge density distribution with transversely polarized excitation, a spacer layer thickness of 25 nm, and a nanowire period of 0.75 times the excitation wavelength, or 384 nm. (c) Graph of average calculated dipole moment magnitudes along a line 8 nm above the surface (as labeled in (a)), as a function of spacer layer thickness from 8 nm to 400 nm. Solid line is spline fitting by smooth order 1.

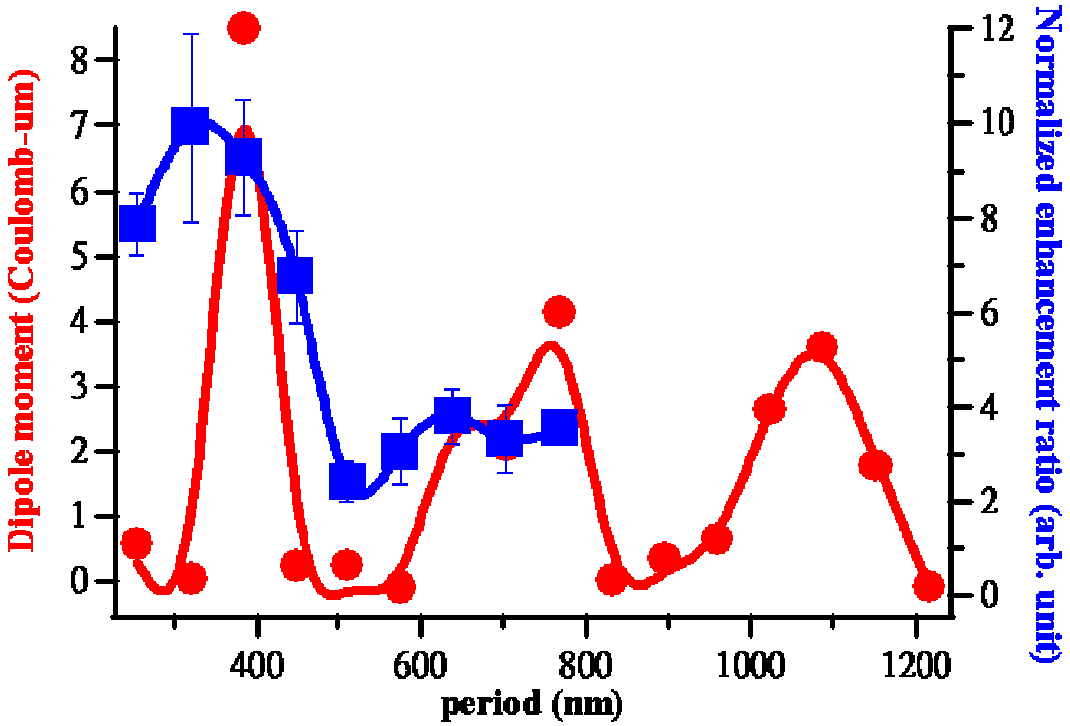

Figure K.2: Graph of Ag coverage area corrected enhancement ratio (blue) and average calculated dipole moment magnitudes (red dots; solid line is a smoothed spline fit, to guide the eye) along a line 8 nm above the surface, as a function of period from 256 nm to 1216 nm, with fixed line width of 192 nm.

Bibliography

1. K. Lance Kelly, et al., *The Optical Properties of Metal Nanoparticles: The Influence of Size, Shape, and Dielectric Environment.* J. Phys. Chem. B, 2003. **107**: p. 668-677.
2. Andres;, R.P., et al., *Self-Assembly of a Two-Dimensional Superlattice of Molecularly Linked Metal Clusters,* Science, 1996. **273**: p. 1690-1693.
3. Gider;, J.S.S., K. Babcock;, and D.D. Awschalom, *Magnetic Clusters in Molecular Beams, Metals, and Semiconductors,* Science, 1996. **271** (No. 5251).
4. Weitz, D.A., et al., *The enhancement of Raman scattering, resonance Raman scattering and fluorescence from molecules adsorbed on a rough silver surface.* J. Chem. Phys., 1983. **78(9)**: p. 5324.
5. Markel, V.A., et al., *Near-field optical spectroscopy of individual surface-plasmon modes in colloid clusters.* Phys. Rev. B, 1999, **59** (No.16).
6. Haynes, C.L., A.D. McFarland, and R.P.V. Duyne, *SURFACE-ENHANCED RAMAN SPECTROSCOPY.* Anal. Chem.., 2005: p. 339A.
7. Zhang, Y., et al., *Metal-enhanced fluorescence: Surface plasmons can radiate a fluorophore's structured emission.* Appl. Phys. Lett., 2007. **90** (053107).
8. Cole, J.R. and N.J. Halas, *Optimized plasmonic nanoparticle distributions for solar spectrum harvesting.* Appl. Phys. Lett., 2006. **89** (153120).
9. Gersten, J.I. and A. Nitzan, *Photophysics and photochemistry near surfaces and small particles.* Surface Science, 1985, **158**(1-3): p. 165.
10. Aslan, K., et al., *Metal-enhanced fluorescence: an emerging tool in biotechnology.* Current Opinion in Biotechnology, 2005. **16**: p. 55.

11. Sun, B., E. Marx, and N.C. Greenham, *Photovoltaic Devices Using Blends of Branched CdSe Nanoparticles and Conjugated Polymers.* Nano Letters, 2003. **3**(7): p. 961.
12. Schmidt, M., et al., *Electro-optically tunable photonic crystals.* Appl. Phys. Let., 2005. **87** (121110).
13. Schro¨ter, U. and D. Heitmann, *Surface-plasmon-enhanced transmission through metallic gratings.* Phys. Rev. B, 1998. **58**(23).
14. Le, F., et al., *Plasmons in the Metallic Nanoparticle-Film System as a Tunable Impurity Problem.* Nano Letters, 2005. **5**(10): p. 2009.
15. T. Corrigan, GUO, S.H., et al., *Enhanced fluorescence from Ag nanoRods: Is Particle Plasmon Resonance Alone Responsible?* In press, 2008
16. Okamoto, T. and I. Yamaguchi, *Optical Absorption Study of the Surface Plasmon Resonance in Gold Nanoparticles Immobilized onto a Gold Substrate by Self-Assembly Technique.* J. Phys. Chem. B, 2003. **107** (38).
17. Corrigan, T.D., et al., *Systematic study of the size and spacing dependence of Ag nanoparticle enhanced fluorescence using electron-beam lithography.* Appl. Phys. Let., 2006. 88(101112).
18. Jensen, T.R., et al., *Nanosphere Lithography: Tunable Localized Surface Plasmon Resonance Spectra of Silver Nanoparticles*. J. Phys. Chem. B, 2000. 104: p. 10549.
19. Kadir Aslan, Z.L., Joseph R. Lakowicz and Chris D. Geddes, *Annealed Silver-Island Films for Applications in Metal-Enhanced Fluorescence: Interpretation*

in Terms of Radiating Plasmons. Journal of Fluorescence, 2005. **15**(5): p. 643-654.

20. Joseph R. Lakowicz, Y.S., Sabato D'Auriaa, Joanna Malicka, Jiyu Fangb, Zygmunt Gryczynskia and Ignacy Gryczynskia, *Radiative Decay Engineering 2. Effects of Silver Island Films on Fluorescence Intensity, Lifetimes, and Resonance Energy Transfer*. Anal. Biochem., 2002. **301**(2): p. 261-277.
21. Sebastian Gerber, F.R., Ulrich Hohenester, Thomas Schlagenhaufen, Joachim R. Krenn, and Alfred Leitner, *Tailoring light emission properties of fluorophores by coupling to resonance-tuned metallic nanostructures*. Phys. Rev. B, 2007. **75**: p. 073404.
22. Shuming Nie, and S. R. Emory, *Probing Single Molecules and Single Nanoparticles by Surface-Enhanced Raman Scattering*, Science, 1997. **275**: p. 1102.
23. Bruce T. Draine, P.J.F., *User Guide for the Discrete Dipole Approximation Code DDSCAT (version6.1)*, 2004.
24. Yee, K.S., *Numerical solutions of initial boundary value problems involving Maxwell's equations in isotropic media*, IEEE Transactions on Antennas and Propagation, 1966. **AP-14**: p. 302-307.
25. Allen Taflove, M.E.B., *Numerical Solution of Steady-state Electromagnetic. Scattering Problems Using the Time-Dependent Maxwell's. Equations,* Microwave Theory and Techniques, IEEE Transactions on, 1975. **23**(8): p. 623-630.

26. Neureuther, A., *TEMPEST FDTD software developed by Univ. of California at Berkeley*.

27. Franck, J. *Elementary processes of photochemical reactions,* Transactions of the Faraday Society, 1926, 21: 536-542

28. Lakowicz, J.R., *Radiative Decay Engineering: Biophysical and Biomedical Applications,* Analytical Biochemistry, 2001. **298**(1-24).

29. Malicka, J., I. Gryczynski, and J.R. Lakowicz, *Enhanced Emission of Highly Labeled DNA Oligomers near Silver Metallic Surfaces,* Analytical chemistry, 2003. **75**: p. 4408.

30. Lakowicz, J.R., et al., *Radiative decay engineering: the role of photonic mode density in biotechnology,* J. of Physics D: Applied Physics, 2003. **36**: p. R240-R249.

31. Gotschy, W., et al., *Thin films by regular patterns of metal nanoparticles: tailoring the optical properties by nanodesign,* Appl. Phys. B, 1996. **63**: p. 381.

32. N. Fe´ lidj, et al., *Optimized surface-enhanced Raman scattering on gold nanoparticle arrays.* Appl. Phys. Let., 2003. **82** (18) p.3095

33. D.-H. Tsai, S. H. Kim, T. D. Corrigan, R. J. Phaneuf, and M. R. Zachariah, *Electrostatic-directed deposition of nanoparticles on a field generating substrate, Nanotechnology* **2005**, *16*, 1856.

34. H. J. Fissan, C. Helsper, and H. J. Thielen, *Determination of particle size distributions by means of an electrostatic classifier,* Journal of Aerosol Science **14** (3), 354 (1983).

35. D.-R. Chen and D. Y. H. Pui, *A High Efficiency, High Throughput Unipolar Aerosol Charger for Nanoparticles, J. Nanoparticle Res.* **1999**, *1*, 115.
36. E. Rencs and S.-H. Guo, unpublished.
37. Radmacher, M. et al, (1994) *Imaging adhesion forces and elasticity of lysozyme adsorbed on mica with the atomic force microscope,* Langmuir. 10: 3809-3814
38. J. I. Goldstein, et al, (1992) *Scanning Electron Microscopy and X-Ray Microanalysis. 2nd Ed.*, Plenum
39. Kan, H.-C., *We developed our own Fortran program to calculate the E-field distribution based on the dipole moments calculated by the discrete dipole approximation method.*
40. Gill Barequet, M. T. Dickerson, and M.T. Goodrich, *Voronoi diagrams for polygon-offset distance functions,* Springer/Heidelberg, Vol. 1272/1997
41. Lakowicz, et al., (2006) *Principles of Fluorescence Spectroscopy. 3rd Ed.,* Springer
42. S.-H. Guo, et al., *the Effect of an Active Substrate on Nanoparticle-Enhanced Fluorescence,* Advanced Materials, 2008.
43. M. Moskovits, *Surface-enhanced spectroscopy,* Rev. Mod. Phys. 57 (3):783 (1985)
44. E. Hao and G. Schatz, *Electromagnetic fields around silver nanoparticles and dimmers,* J. of Chem. Phys. 2004, 120, 357.
45. B. T. Draine and P. J. Flatau, ***Discrete-dipole approximation for scattering calculations****,* J. Opt. Soc. Am. A, **2004,** 11, 1491.

46. P. B. Johnson and R. W. Christy, *Optical Constants of the Noble Metals,* Phys. Rev. B 1972, *6*, 4370.

47. G. M. Hale and M. R. Querry, ***Optical constants of water in the 200-nm to 200-micrometer wavelength region,*** Appl. Opt., 1973, *12*, 555.

48. M. D. Malinsky, K. L. Kelly, G. C. Schatz, and R. P. V. Duyne, *Nanosphere Lithography: Effect of Substrate on the Localized Surface Plasmon Resonance Spectrum of Silver Nanoparticles,* J. Phys. Chem. B **2001**, *105*, 2343.

49. G. E. Jellison, Jr., *Optical functions of silicon determined by two-channel polarization modulation ellipsometry,* Opt. Mater. **1**, 41 (1992).

50. T. D. Corrigan, et al., *Enhanced Fluorescence from Periodic Arrays of Silver Nanoparticles*. J. of Fluorescence 15 (5), 2005.

51. R. Fuchs, *Theory of the optical properties of ionic crystal cubes,* Phys. Rev. B 11, p. 1732, 1975.

52. J. P. Kottmann, O. J. F. Martin, D. R. Smith, and Sheldon Schultz, *Plasmon resonances of silver nanowires with a nonregular cross section,* Phys. Rev. B **64**, 235402 (2001).

53. U. Kreibig, P. Zacharias, *Surface plasma resonances in small spherical silver and gold particles,* Zeitschrift für Physik A Hadrons and Nuclei 231, 128 (1970)

54. A. Pinchuk, et al., *Substrate effect on the optical response of silver nanoparticles,* Nanotechnology 15, 1890 (2004)

55. T. C. Pluym, Q. H. Powell, A. S. Gurav, T. L. Ward, T. T. Kodas, L. M. Wang, and H. D. Glicksman, *Solid silver particle production by spray pyrolysis, J. Aerosol Sci. 24*, 383 (1993)

56. K. Kneipp, et al., *Single Molecule Detection Using Surface-Enhanced Raman Scattering (SERS),* Phys. Rev. Lett. 78, 1667 (1997)

57. R. Jin, et al., *Photoinduced Conversion of Silver Nanospheres to Nanoprisms,* Science **294**, p. 1901-1903 (2001).

58. A. Christ, et al., *Interaction between localized and delocalized surface plasmon polariton modes in a metallic photonic crystal,* Phys. Stat. Sol. (b) 243, 10, p. 2344-2348 (2006)

59. J. Cesario, et al., *Electromagnetic coupling between a metal nanoparticle grating and a metallic surface,* Opt. Lett. 30, 3404 (2005)

60. W. R. Holland, and D. G. Hall, *Frequency Shifts of an Electric-Dipole Resonance near a Conducting Surface,* Phys. Rev. Lett. 52, 12, p. 1041-1044 (1984)

61. W. R. Holland, and D. G. Hall, *Surface-plasmon dispersion relation: Shifts induced by the interaction with localized plasma resonances,* Phys. Rev. B, 27, 12, p. 7765-7768 (1983)

62. W. L. Barnes, *Fluorescence near interfaces: The role of photonic mode density,* J. Mod. Opt. 45(4), p. 661-699 (1998)

63. R. W. Gruhlke, W. R. Holland, and D. G. Hall, *Surface plasmon cross coupling in molecular fluorescence near a corrugated thin metal film,* Phys. Rev. Lett. 56, p. 2838, (1986)

64. I. Baltog, et al., *Surface enhanced Raman scattering on silver grating: Optimized antennalike gain of the stokes signal of 10^4*, Appl. Phys. Lett. 66 (10), p. 1187-1189 (1995)

65. J. Kalkman, et al., *Surface plasmon polariton modified emission of erbium in a metallodielectric grating,* Appl. Phys. Lett. 83 (1), p. 30-32 (2003)

66. W. Gotschy, et al., *Optical dichroism of lithographically designed silver nanoparticle films***,** Opt. Lett. 21 (15), 1099 (1996)

67. Taflove, A. and S.C.Hagness, *Computational Electrodynamics: The Finite-Difference Time-Domain Method.* Artech House, Boston-London, (2000)

68. Adhidjaja, J. and G. Horhmann, *A Finite-Difference Algorithm for the Transient Electromagnetic Response of a Three-Dimensional Body.* Geophysics J. Int., **98**: p. 233-242 (1989)

69. Piket-May, M. and A. Taflove, *Electrodynamics of Visible-Light Interactions with the Vertebrate Retinal Rod.* Optics Letters, **18**(8): p. 568-570 (1993)

70. Crozier, K.B., et al., *Optical antennas: Resonators for local field enhancement.* Journal of Applied Physics, **94**(7), p. 4632-4642 (2003)

71. Sadiku, M., *Numerical Techniques in Electromagnetics.* CRC Press, 1992.

72. D Chirvase, J.P., J C Hummelen and V Dyakonov, *Influence of nanomorphology on the photovoltaic action of polymer–fullerene composites.* Nanotechnology, **15**: p. 1317-1323 (2004)

73. A. Wokaun, *Surface enhancement of optical fields**:** Mechanism and applications,* Mol. Phys. 56 (1), 1-33 (1985).

74. H. Szmacinski, J.R. Lakowicz, and M.L. Johnson, *Fluorescence lifetime imaging microscopy: Homodyne technique using high-speed gated image intensifier,* Methods in Enzymology, **240**, p. 723-748 (1994)

75. J. R. Lakowicz, et al., *Lifetime-selective fluorescence imaging using an rf phase-sensitive camera,* Rev. Sci. Instrum, 62 (7), 1727 (1991)

76. J. R. Lakowicz, et al., *Fluorescence lifetime imaging,* Analy. Biochem., 202 (2), p. 316-330 (1992)

77. D. Lavender, et al., *Voronoi Diagrams of Set-Theoretic solid Models,* IEEE Computer Graphics and Applications, 12(5), p. 69-77 (1992)

78. F. Kong, et al., *Surface plasmon mode analysis of nanoscale metallic rectangular waveguide***,** Optics Express, 15 (19):12331 (2007)

79. R. Buckley, and P. Berini, *Figures of merit for 2D surface plasmon waveguides and application to metal stripes***,** Optics Express, 15 (19):12174 (2007)

80. G. Schider, et al., *Optical properties of Ag and Au nanowire gratings,* J. Appl. Phys. 90 (8):3825 (2001)

81. B. Lamprecht, et al., *Metal Nanoparticle Gratings: Influence of Dipolar Particle Interaction on the Plasmon Resonance,* Phys. Rev. Lett. 84 (20):4721 (2000)

82. J. D. Jackson, *Classical Electrodynamics,* 3rd Ed., John Wiley & Sons, Inc. (1999)